TAMPERE UNIVERSITY OF TECHNOLOGY

MANU NURMINEN

IMAGING AND ANALYSIS OF P(L/D)LA 96/4 JOINT SCAFFOLD USING COMPUTED TOMOGRAPHY

Master of Science Thesis

Thesis examiners:
Professor Minna Kellomäki
Professor Jari Hyttinen

Examiners and topic approved in the
Faculty of Automation, Mechanical and
Materials Engineering council meeting
on February 9th, 2011

ABSTRACT

TAMPERE UNIVERSITY OF TECHNOLOGY
Master's Degree Programme in Materials Science
NURMINEN, MANU: Imaging and analysis of P(L/D)LA 96/4 joint scaffold using computed tomography
Master of Science Thesis, 88 pages, 4 Appendix pages
May 2011
Major: Biomaterial Engineering
Examiners: Professor Minna Kellomäki, Professor Jari Hyttinen
Keywords: Computed tomography, polymeric scaffold, structural characterization

The architecture of tissue engineering scaffold has a strong effect on its functionality. The micro-computed tomography (μ-CT) is a non-destructive X-ray irradiation based imaging method which has been widely used in scaffold characterization. The technique enables accurate visualization of the internal structures and morphology in two- and three-dimensions. In addition, image data can be used to calculate numerical values for several structural parameters including porosity and pores sizes.

In the present study, the structure of five different types of joint scaffolds was studied using two different CT types. Studied scaffolds are designed for small joint (metacarpophalangeal joint) reconstruction. Imaging was performed using Planmeca ProMax 3Ds cone-beam computed tomography (CBCT) and high resolution SkyScan-1072 desktop fan-beam micro-CT. The main purpose of the study was to assess the suitability of Planmeca CBCT for structural characterization and for quality control of porous scaffolds. Main studied scaffold type was P(L/D)LA 96/4 joint scaffold. Motivation for this study comes from the specific properties of Planmeca CBCT which overcome the general limitations of micro-CT. The device is originally designed for dental imaging allowing fast image acquisition and has also a large measuring field which enables imaging the entire implant structure with a single scan.

First goal in the present study was to find out the highest image quality which can be achieved with Planmeca device. In practice, different CT imaging parameters were tested and some of the samples were modified with different contrast enhancement techniques before imaging. The quality of obtained images was visually evaluated and the best images were selected for structural parameter determination. A SkyScan micro-CT was used in a comparative study in order to estimate the reliability of Planmeca CBCT study and to compare the suitability of these two devices for scaffold characterization. The spatial resolution of the SkyScan micro-CT was beforehand known to be significantly better than in Planmeca CBCT.

Sample modification studies proved that it is very challenging to improve image contrast and use contrast enhancement techniques non-destructively without causing any structural changes to the scaffold. Without using any contrast enhancement, the CBCT image quality was good enough to apply them for image analysis and determine porosity degree and porosity degree distribution of scaffolds. Also glass content of two types of scaffolds was calculated successfully. Pore sizes (pore diameter) could not be calculated due to complex scaffold architecture and lack of sophisticated image analysis program but total pore volume distribution was determined instead. Quality of Planmeca CBCT images was not the best possible due to still poor accuracy and contrast even though the imaging parameters were optimized carefully. Planmeca CBCT characterization cannot be considered reliable because images did not give realistic overview of the scaffold fibrous structure, unlike the micro-CT images did. The use of Planmeca CBCT in the quality control would still be possible but that would require standardization of the CT imaging parameters and image analysis parameters. Parameter standardization would allow comparing the mutual differences in architectures of parallel samples.

TIIVISTELMÄ

TAMPEREEN TEKNILLINEN YLIOPISTO
Materiaalitekniikan koulutusohjelma
NURMINEN, MANU: Imaging and analysis of P(L/D)LA 96/4 joint scaffold using computed tomography
Diplomityö, 88 sivua, 4 liitesivua
Toukokuu 2011
Pääaine: Biomateriaalitekniikka
Tarkastajat: professori Minna Kellomäki, professori Jari Hyttinen
Avainsanat: Tietokonetomografia, polymeeri skaffoldi, rakenteen karakterisointi

Kudosteknologiassa käytettävien tukirakenteiden (skaffoldien) rakenteella on merkittävä vaikutus niiden toimivuuteen implantoituna. Mikrotietokonetomografia (μTT) perustuu röntgensäteilyyn ja on ainetta rikkomaton kuvantamismenetelmä, jota on laajalti käytetty skaffoldien rakenteen karakterisoinnissa ja optimoinnissa. Menetelmä mahdollistaa näytteen rakenteen kaksi- ja kolmiulotteisen visualisoinnin sekä useiden rakenteellisten parametrien määrittämisen sopivaa kuvankäsittelymenetelmää käyttäen.

Tämän diplomityön kokeellisessa osassa tutkittiin kahdella erilaisella tietokonetomografialaitteella viiden erityyppisen nivelskaffoldin rakennetta. Kuvantamislaitteina toimivat Planmeca ProMax 3Ds ja SkyScan-1072. Tutkimuksen ensisijaisena näytetyyppinä toimi P(L/D)LA 96/4 skaffoldi, mutta tutkimukseen sisältyi myös neljän muun erityyppisen skaffoldin karakterisointi. Kaikkien skaffoldien perustana oli neulottu P(L/D)LA 96/4 polymeeri. Kolme skaffoldityyppiä sisälsi lisäksi kitosaania ja/tai bioaktiivista lasia. Työn päätavoitteena oli selvittää alun perin hammaslääketieteen käyttöön suunnitellun Planmeca ProMax 3Ds soveltuvuus huokoisten skaffoldien rakenteen tutkimiseen sekä laadunhallintaan. Laite mahdollistaa kokonaisen implantin kuvantamisen ja analysoinnin nopeasti yhdellä kertaa, mikä on merkittävä etu yleisesti käytettyihin mikrotietokonetomografialaitteisiin verrattuna.

Kuvan laadulla on merkittävä vaikutus rakenteen karakterisoinnin luotettavuuteen. Sen vuoksi tutkimuksen alussa oli tarkoituksena selvittää, kuinka hyvä kuvanlaatu Planmeca ProMax 3Ds laitteella voidaan saavuttaa. Käytännössä tämä tarkoitti kuvantamista eri laiteparametreilla ja modifioimalla skaffoldeja röntgenpositiivisuutta lisäävillä aineilla. Kuvien laatu arvioitiin visuaalisesti ja parhaimmanlaatuiset kuvat valittiin kuva-analyysiin, jossa skaffoldien huokoisuusaste, huokoisuusasteen vaihtelu skaffoldin eri osissa ja huokoskoko oli tavoitteena määrittää. SkyScan-1072 mikrotietokonetomografiaa käytettiin vertailevassa tutkimuksessa, jonka tarkoituksena oli arvioida Planmeca ProMax 3Ds:n luotettavuutta skaffoldien karakterisoinnissa. SkyScan-laitteen tarkkuuden tiedettiin olevan huomattavasti Planmecan laitetta parempi.

Tutkimuksessa selvisi, että skaffoldien modifiointi röntgenpositiivisilla aineilla ei merkittävästi parantanut TT-kuvien kontrastia. Lisäksi näytteiden modifiointi vaurioittamatta tai muuttamatta alkuperäistä skaffoldin rakennetta osoittautui erittäin haasteelliseksi. Kuvien kontrasti oli riittävä kuva-analyysin suorittamiseksi ilman kontrastinparantamisaineiden käyttöä ja tutkimuksessa onnistuttiin määrittämään skaffoldien huokoisuusaste sekä huokoisuusaste skaffoldin eri osissa. Myös kahden skaffoldityypin lasipitoisuus onnistuttiin määrittämään. Skaffoldien huokoskokoa ei onnistuttu laskemaan johtuen skaffoldin vaativasta rakenteesta sekä siitä, että ei ollut määritykseen soveltuvaa kuvankäsittelyohjelmaa käytettävissä. Sen sijaan, huokosten kokonaistilavuus onnistuttiin laskemaan. Planmecan laitteella hankittujen kuvien tarkkuus ja kontrasti pysyivät hieman heikkoina, vaikka kuvantamisparametrit olivat tarkoin optimoituja. Koska skaffoldin rakenne Planmecan CT kuvissa ei vastaa tarkasti todellista rakennetta, ei myöskään laskettuja rakenteellisien parametrien arvoja voida pitää luotettavina. Planmeca ProMax 3Ds käyttö laadunvalvonnassa on kuitenkin mahdollista, mutta se edellyttää vakioitujen parametrien käyttöä kuvantamisessa sekä kuva-analyysissä. Vakioitujen parametrien käyttö mahdollistaisi rinnakkaisten skaffoldien rakenteellisten poikkeamien havaitseminen.

PREFACE

This Master of Science thesis was done at the Department of Biomedical Engineering at Tampere University of Technology. The study was a part of Tekes funded MIKAMA II project.

I would like to thank Professor Minna Kellomäki, Professor Jari Hyttinen and Researcher Kaarlo Paakinaho for giving me this interesting subject and directions during the study. For the instructions for imaging and image analysis I would like to thank Researcher Baran Aydogan and Researcher Markus Hannula. Aydogan performed the pore analysis part of the study using Pore Analyzer software. The software was developed during MIKAMA project.

Thanks to the staff of the Department of Biomedical Engineering, especially to other thesis workers, for creation of comfortable working environment during the summer 2010.

Tampere, 26.4.2011

TABLE OF CONTENTS

MATHEMATICAL SYMBOLS

A	Area of scaffold bottom
A_T	Total amount of pixels in circle area
A_s	Average amount of non-zero pixels in circle area
d	Strut diameter
h	Scaffold height
I_0	Initial radiation intensity
I	Radiation intensity
L	Strut length
l	Scaffold length
m	Scaffold mass
n_1	Number of struts per layer
n_2	Number of layers per scaffold
r	Circle radius
V	Scaffold volume
V_a	Scaffold cube volume
V_f	Scaffold material volume
V_g	Scaffold material volume
w	Scaffold width
x	Object thickness
μ	Attenuation constant of material
ρ	Scaffold density
π	Pi
Ø	Diameter

TERMS AND ABBREVIATIONS

In horizontal direction	From central part of the sample to its fringe areas
In vertical direction	From the top of the sample to its bottom
Porosity degree	Percentage of pore volume in a total volume of the sample
Porosity distribution	Porosity degree in the separate sections of the sample

2D	Two-dimensional
3D	Three-dimensional
AFM	Atomic force microscopy
BaSO4	Barium sulphate
BaG	Bioactive glass
$CaCl_2$	Calcium chloride
CBCT	Cone-beam computed tomography
CLSM	Confocal laser scanning microscopy
CT	Computed tomography
CP	Calcium phosphate
EBCT	Electron beam computerized tomography
ECM	Extracellular matrix
FEM	Finite element modelling
FP	Flow porosimetry
GA	Gas adsorption
GP	Gas pycnometry
HA	Hydroxyapatite
H_2O	Water
HCl	Hydrochloric acid
KCl	Potassium chloride
K_2HPO_4	Dipotassium phosphate
$MgCl_2$	Magnesium chloride
MIP	Mercury intrusion porosimetry
MPM	Multiphoton microscopy
MRI	Magnetic resonance imaging
Na_2SO_4	Sodium sulphate
NaCl	Sodium chloride
$NaHCO_3$	Sodium hydrogen carbonate
NaOH	Sodium hydroxide
OCT	Optical coherence tomography
P(L/D)LA	Poly-L/D-lactide
P scaffold	P(L/D)LA 96/4 scaffold
PC scaffold	P(L/D)LA 96/4 + chitosan scaffold

PCG scaffold	P(L/D)LA 96/4 + chitosan + bioactive glass scaffold
PCL	Polycaprolactone
PG scaffold	P(L/D)LA 96/4 + bioactive glass scaffold
PGA	Polyglycolide
pI_2DTEc	Poly(desaminotyrosyl-tyrosine ethyl ester carbonate)
PLDL	Poly(L-lactide-co-DL-lactide)
PLGA	Poly(lactide-co-glycolide)
SEM	Scanning electron microscopy
SBF	Simulated body fluid
TM	Theoretical methods
Tris	Tris(hydroxymethyl)aminomethane
VOI	Volume of interest
β-TCP	Beta-tricalcium phosphate
μCT	Micro-computed tomography

1. INTRODUCTION

A common tissue engineering application of biodegradable polymers is their use as scaffolds. Scaffold function is to give temporary mechanical support and a template for various cell populations in order to achieve tissue regeneration and repair. Architecture of scaffolds has a significant effect on functionality of the scaffold as they affect both mechanical and biological properties of the constructs. Architecture affects the robustness of the scaffold both *in vivo* and *in vitro*. Structure of pore network affects the cell migration and adhesion into the scaffold, vascular ingrowth and molecular transport (oxygen, nutrient, metabolic wastes and molecular signaling) through construct. [35; 40]

Architecture of tissue engineering scaffold is generally defined using certain structural parameters including porosity degree, pore size and pore interconnectivity [14; 34; 41]. The reliable determination of the structure can be utilized to follow and optimize the relationship of scaffold design and functionality and also to assess the feasibility and repeatability of fabrication process [40]. Proper technique can also be applied as a non-destructive testing method in quality control and verification merged together with implant manufacturing [28; 50].

During the past decade the scaffold architectural characterization using X-ray irradiation based micro-computed tomography (μCT) imaging has increased its popularity. The technique combines non-destructive and accurate characterization giving also a reliable 2D and 3D visualization of the interior structure. These key properties of CT overcome the limitations of many other techniques. [14; 46] The CT has also been used in several other tissue engineering applications such as measurements of forming rate of engineered tissue [75], the vessel ingrowth into biomaterial structure [26], fluid transport through scaffold [11] and designing of new implant structures [29; 43]. However, the reliable image-based characterization of materials and tissues is considered as a challenging task and requires both acquisition of high-quality images and skilled image analysis [61].

The subject of this study combines the fields of biomaterials and biomedical imaging as two main objectives were to find out if the Planmeca ProMax 3Ds cone-beam computed tomography (CBCT) is a suitable method to characterize complex polymeric structures and consider if this technique could be applied in quality control of P(L/D)LA 96/4 joint scaffolds. Differences between low resolution CT and high resolution micro-CT was also intended to be compared and to discuss which device type would be suited better for examining of polymeric scaffolds. The study should also answer a question that could Planmeca CBCT be used in examining of other porous structures than knitted ones. In spite of its low resolution, Planmeca ProMax 3Ds is particularly appealing because it allows non-destructive material testing and it has also a

large measuring field (compared to standard μCT) which enables to determine the entire scaffold with a single scan. Five types of fibrous joint scaffolds designed for small joint (metacarpophalangeal joint) reconstruction was used as samples.

This work started with experimental studies which aim was first to optimize the quality of scaffold Planmeca CBCT images as contrast and accuracy levels were in main focus. In practice, the optimization included sample modification with different contrast enhancement techniques and imaging with different scanning parameters. The lack of X-ray contrast was a known challenge in polymer imaging and therefore several contrast enhancement methods needed to be developed [15]. It was also known that scanning parameters have a strong effect on image quality and therefore the parameters were optimized by trials and errors [5; 33]. Then the quality of achieved images was intended to be visually evaluated and if the quality was sufficient, images would be applied for determination of structural parameters. The porosity degree, porosity distribution and pore size of scaffolds was in main focus. A suitable image analysis program needed to chose and analysis process needed to be developed. The correlation between mass and the porosity was also intended to be examined and therefore each scaffold was weighed.

A starting point for this study was challenging because Planmeca ProMax 3Ds has originally been designed for dental imaging and thus its suitability for polymer imaging was unknown. The spatial resolution of the device was assumed to be too weak to recognize the filaments separately and so it was not supposed that the image-based calculated porosity degree values would be absolutely correct, but however, they would be sufficiently comparable. In order to evaluate the reliability of the Planmeca CBCT characterization, the comparative examination with SkyScan μCT was included in this study. Pore diameter of P(L/D)LA 96/4 joint scaffold have previously been estimated only from 2D microscopic images and porosity degree has been calculated using a theoretical method [47; 70]. In the present study, more precise structural analysis from three-dimensional nature of the scaffold was aimed to be performed using volumetric image data.

The first part of this thesis gives necessary theoretical background information about performed experimental studies describing the architecture of scaffolds and also introducing and comparing commonly applied techniques for structural characterization. Computed tomography and its usability in the field of tissue engineering are described thoroughly. Performed experimental studies are described in detail from sample preparation to image-based structural characterization in experimental part of the text. The last part of the text presents achieved results, assess critically their reliability and suggests improvement proposals for the future studies.

THEORETICAL PART

2. ARCHITECTURE OF POROUS SCAFFOLDS

Architecture among other important features of scaffolds such as biocompatibility, biodegradability and mechanical properties must be considered in order to achieve successful function of the construct. Several different scaffold designs have been developed in order to fulfill the requirements of various biomedical applications. Macroscopic shape of the earlier studied scaffolds varies from fibrous to sponge and from honeycomb to foams and hydrogels. [10; 28] Two examples of the developed scaffold architectures are illustrated in Figure 2.1. Certain structural characteristics have been introduced for more exact describing and assessing of these variable constructs [28]. The definitions of important structural characteristics and their effects on functionality of scaffold are described in this chapter and summarized in Table 2.1. The optimization process of scaffold architecture is clarified in the last part of the chapter.

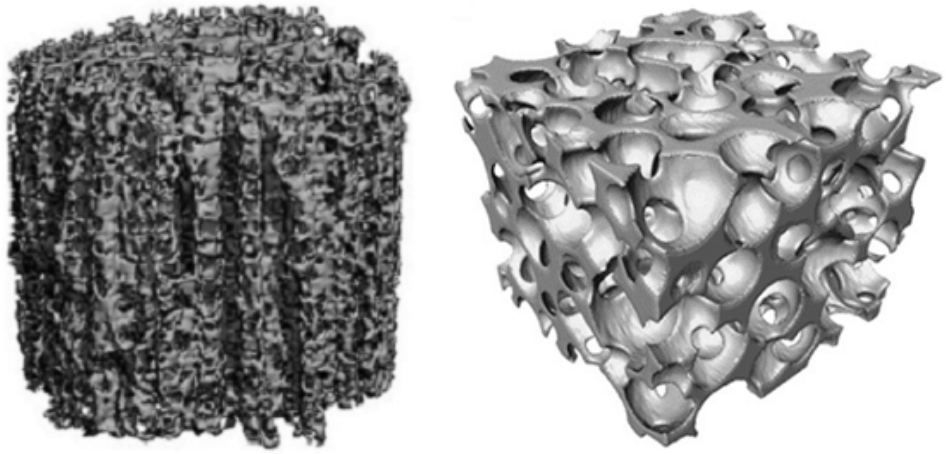

Figure 2.1. *Micro-CT images illustrating two different porous scaffold designs. Oriented poly(L-lactide-co-DL-lactide) (PLDL) scaffold created using a solution coating and porogen decomposition method (left) [40] and a bioactive glass scaffold fabricated using sol-gel foaming (right) [34].*

Widely discussed characteristic in literature is porosity degree which can be defined as the percentage of empty space in a total volume of the scaffold. Porosity affects to mechanical strength, cell seeding efficiency and diffusion. High porosity degree is required for uniform cell delivery, cellular attachment and tissue in-growth. [28.] Disadvantage of highly porous network is that it tends to compromise the mechanical strength of the construct and therefore sets an upper functional limit for porosity and pore sizes. Mechanical properties should be similar to those of tissue repair site and thus the demand for strength depends on the type of growing tissue. [28; 35; 50] Functional

diffusion and vasculature growth are necessary for proper molecular transport in tissue engineering scaffold including the exchange of oxygen, nutrient and metabolic wastes. The functional molecular transport facilitates the migration and proliferation of cells to interior of the scaffold and ensures their survivability. [28.] Typical desirable porosity degree for scaffolds is around 90 %, but the sufficient degree varies significantly according to application requirements and other characteristics [14; 35; 76].

As most cells utilized in tissue engineering are anchorage dependent, high surface porosity and surface area of the scaffold facilitate clearly cell attachment and proliferation. [10; 50] Porous surface also enables mechanical attachment between the implant and surrounding tissue improving mechanical stability [35]. Surface area to volume ratio can be determined as a share of surface area of scaffold and volume of scaffold material [28].

The size and type of the pores affect the function of the scaffold. Pore size can be defined as an average diameter of the pores [35]. Scaffold pore types can be divided into three classes as illustrated in the left picture in Figure 2.2. The closed pores are not accessible. Open (interconnected) pores can be either through pores which extend from one end to the other or blind pores which end inside the material. [28.] Pore sizes, sufficiently large in relation to the cell size, assists cell migration, proliferation, tissue in-growth and capillary formation [35]. Rough estimation for minimum requirement for pore size of bone scaffold is stated to be around 100 µm. This pore size enables fluid transport and migration of osteoblasts but larger pores, approximately in range of 300-350 µm, allow vascularization and promote bone in-growth. [35; 41; 44] However, very large pores can reduce surface area for cells and slow down cell proliferation [41]. Scaffolds with pore sizes between 10 µm and 75 µm may not allow bone in-growth, but instead fibrous tissue is observed to grow in to a scaffold even though pores are small [35].

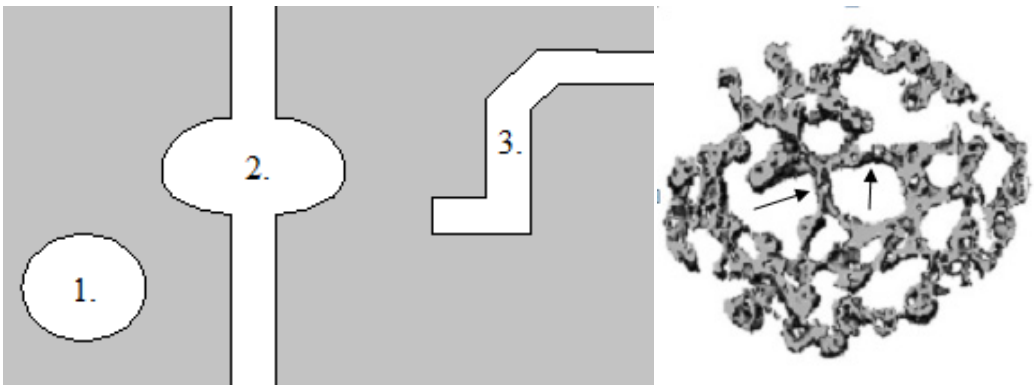

Figure 2.2. *Left picture illustrates the three possible types of pores within the scaffold. Closed pore (1), open through pore (2) and open blind pore (3). [Modified 28] Right image is a representative cross-section µCT image of PLDL scaffold in which the arrows indicate scaffold walls. [Modified 40]*

Interconnectivity is a characteristic which is used to describe the percentage share of interconnected pore volume and interconnected and closed pore volume. Biodegradable

implants with highly interconnected pore networks enable immediate cell migration and tissue in-growth and also facilitates molecular transport and vascularization at implantation site. [14; 44; 46]

Cross section area is a measure of the area in a specified sectional plane of the scaffold [28]. Cross sectional images of a scaffold are commonly used to visualize and measure structural characteristics including wall thickness and pore sizes [40; 47]. Right picture in Figure 2.2. shows a cross-section from the same scaffold as shown in Figure 2.1. (left). Wall thickness is defined as an average diameter of scaffold wall and it is illustrated in right picture in Figure 2.2. [28]. Strut is a used expression instead of wall if the scaffold has a regular honeycomb or fibrous design. The strut thickness is shown to affect cell attachment and cell form. The fiber diameter should be suitable in relation to cell size because too thin fibers have resulted in weaker attachment on the surface of biomaterial. [35.]

Anisotropy is a measure of the non-uniformity in the alignment of the scaffold struts [28]. Permeability describes the ease of at which fluid passes through the pores. Strut thickness, anisotropy and cross sectional area of the scaffold has a strong effect on mechanical strength of construct. [28; 35]

Table 2.1. *Summary of typical structural characteristics and their effects on the functionality of the scaffold. [28; 35; 46; 50]*

Characteristics	**Influences**
Anisotropy	Cell attachment
Cross-section area	Cell migration
Interconnectivity	Cell proliferation
Permeability	Diffusion
Pore size	Mechanical strength
Porosity degree	Molecular transport
Surface area to volume ratio	Tissue ingrowth
Wall thickness	Vascularization

The identification of optimized scaffold structure is an exceptionally challenging goal which forces to consider several matters, especially scaffold-tissue interactions and balance of structure and mechanical integrity [26; 50]. The optimal design of scaffold should mimic the properties of extracellular matrix (ECM) and therefore the optimal values for scaffold characteristics vary according to generating tissue type and amount of physical loading in implant site. Therefore globally functional values for architectural characteristics cannot be defined. [35; 41; 44] In addition, it is often difficult to optimize a specific parameter without sacrificing the performance of another property. Even that the defined characteristics are presented separately, one must notice that the parameters affect each other and so the functionality of the structure is dependent on the balance of several parameters. [28; 50] Architecture of scaffolds can be varied and optimized by choosing suitable biomaterial, fabrication method and using optimized processing parameters [28; 35; 41; 50].

3. COMPUTED TOMOGRAPHY

In this chapter, the development, operational principle and the most typical tissue engineering application of computed tomography are described. Also the principle of image analysis process and the general problems related to CT characterization of biomaterials and tissues are covered.

3.1. Development

Computed tomography (CT) is an X-ray based imaging method which is used to obtain information about the structure of desired target. Allen MacLeod Cormack and Godfrey Hounsfield are considered as pioneers of medical computed tomography. They developed CT during the 1960s and 1970s receiving the Nobel Prize for Medicine in 1979. [12.]

During the last decades the CT devices have been developed continuously and the development has been driven mainly by three objectives: reduction of image acquisition time, reduction of X-ray exposure and reduction of cost. Several changes in device assembly have been required for reaching these objectives. The changes have been related most in the way that X-ray tubes and detectors are constructed and the way that they move around the object. [12.]

First generation CTs had a single needle-like X-ray beam. During the development the shape of beam has changed from needle-like to a narrow fan beam shape, wide fan beam and conical beam form. The majority of CT scanners currently in use are fan-beam systems. [12.] The movements of the object and radiation system, during imaging, vary between different CT types. For example, the X-ray source and detector rotate around the patient in common medical CT systems whereas in industrial CTs, the radiation system does not usually rotate but the object rotates instead. [73.]

High resolution X-ray micro-computed tomography (μCT) was first developed in the early 1980's and since then it has become the most commonly used CT type for material testing and bioengineering research [25]. Micro-CT can be divided into two types in terms of X-ray sources: synchrotron radiation and laboratory based Micro or Nano focus X-ray tube heads. The speed of scanning process is usually faster and the image resolution is higher with less artifacts in synchrotron μCT systems compared to laboratory μCTs. Synchrotron systems are superior to laboratory systems because its monochromatic X-rays prevent beam hardening and its parallel beam prevents geometric artifacts in the resultant images, which make it easier to record measurements and see fine details. [81.]

The constant development has led to several improvements of the performance of CT devices and to overcome the limitations of the technique. For example, the image reconstruction time has reduced significantly as a two-dimensional image took even 9 days using first generation CT whereas more sophisticated EBCT technique is able to acquire an image in 50 ms. Conventional CTs are only able to provide morphological information of object, but PET-CT scanners, which combine the positron emission tomography (PET) and CT techniques, enable to image morphological and functional information from anatomical region at the same time. [12.]

Phase contrast CT is emerging state-of-the-art imaging technique that can be implemented at third generation synchrotron radiation sources or by using a microfocus X-ray tube. Conventional attenuation-based imaging has shown a limitation in low density object imaging where the absorption contrast is low and fascinating phase contrast technique is expected overcome this limitation. Phase contrast CT improves low-contrast details, such as soft tissues and low density polymers, by using the phase information of the object. [9; 15]

3.2. Operational principle

The operating principle of computed tomography is described in Figure 3.1. Main parts of CT system are radiation source and detector which are situated toward each other. An X-ray fan or cone from radiation source penetrates the object which is located between source and detector and the X-rays with reduced intensities are captured by the detector. [33; 73] Rotation of sample or source and detector during scanning enables to irradiate the object from all sides and thus to measure reduced irradiation intensities from different directions producing sequential X-ray projections from the object [12; 73].

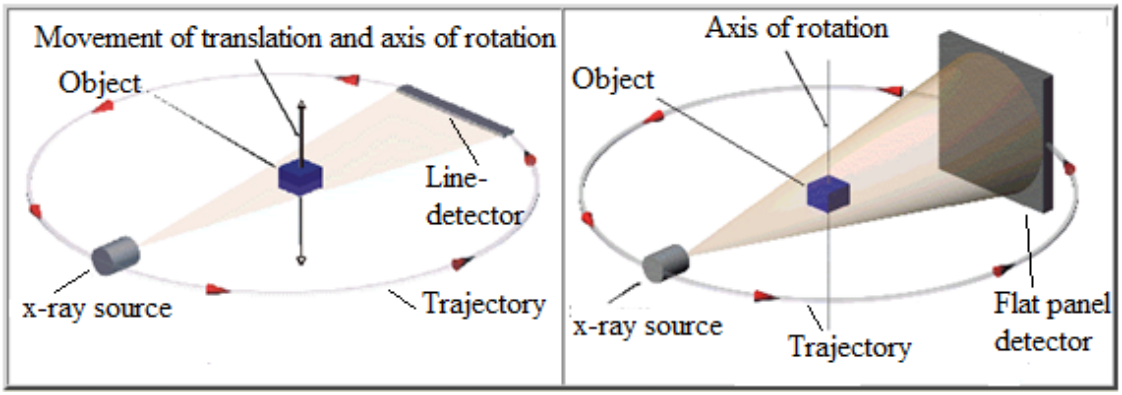

Figure 3.1. *Principle scheme of conventional 2D computed tomography (left) and 3D cone-beam computed tomography (right). [Modified 73]*

Conventional CT measures and reconstructs a set of one dimensional projections during the rotation resulting a two dimensional images. To get a three dimensional image with a conventional tomography is time consuming and it requires that the object has to be moved in the direction of the axis of rotation and several scans have to be taken. Cone-

beam computed tomography instead, allows the reconstruction of three dimensional structures with a single rotation. During rotation, conical beam penetrates the object and attenuation is measured by large area detector. A set of projections is stored and three-dimensional image can be reconstructed based on these two-dimensional images. The arrangement of an axial two-dimensional slice set to build up a three-dimensional volume is called secondary reconstruction [12]. Structure of object can be displayed either as a series of sectional 2D images or a three-dimensional image [23; 73].

In the X-ray devices, the image acquisition is based on that the electromagnetic radiation, which is X-ray irradiation, penetrates object in a different way depending on the energy of the radiation. The energy area of X-ray radiation is in range in which the absorption also depends strongly on the density of sample material. [33.] The radiation intensity decreases exponentially while penetrating through an object along the incident direction. The attenuation is mostly due to absorption and scattering and can be subsumed by a single attenuation coefficient μ as illustrated in Figure 3.2. [12; 15] Because of the material-dependent capability of penetration, attenuation coefficient correlates to the material density [28]. The reduced radiation intensity (I) after passing a distance Δx through an object follows the Lambert-Beers law of attenuation according to equation (1) [12].

$$I = I_0 e^{-\mu x} \qquad (1)$$

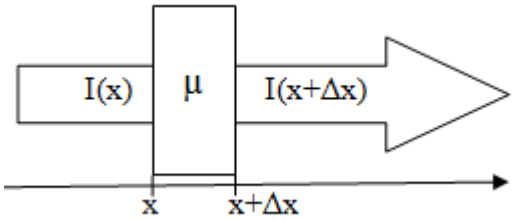

Figure 3.2. *A mathematical model of monochromatic X-ray attenuation. Radiation transmits through an object with constant attenuation coefficient (μ) and thickness (x). [Modified 12]*

where μ, x and I_0 describes attenuation constant of the material (μ), the thickness of object (x) and initial intensity (I_0), respectively.

In output format of digital CT data, the measuring field is divided into stacked 2D images (slices). Pixel describes the smallest unit of each 2D image and one slice consists of certain amount of pixels in *x*- and *y*-direction. In typical CT, the size of the grid is 512 x 512 pixels. [14; 33] A representative 2D μCT image is illustrated in Figure 3.3. When two-dimensional images are stacked forming three-dimensional volume the smallest unit become a voxel (volume element). Each voxel has own intensity value which describes the recorded information and it corresponds to the attenuation coefficient. Therefore resultant grid reveals the material phases within the sample and the different intensity values can be perceived as different colours varying between black and white. [6; 14; 21; 28; 33]

Figure 3.3. *Illustration of 2D μCT image of P(L/D)LA 96/4 joint scaffold and a close-up of it showing the pixel map. Each pixel have own intensity value ranging between black and white. Black pixels describe polymer phase and white pixels empty regions. The image has been taken from the present study.*

The information contained by digital images is usually presented as relative CT values which can vary between -1000 and +3096. On that scale the value of water is 0 and air is -1000. The soft tissues are placed between -100 and +200 and bone between +50 and +550. [33.]

3.3. Biomaterial and tissue engineering applications

The use of computed tomography is a part of a clinical routine and is nowadays the most widely used imaging technology in radiology. Patients with heavy trauma and fractures benefit greatly from the clarification provided by CT as well as surgeons can use this information in order to get an impression of the images that are taken intraoperatively. Beyond CTs medical use, technical, anthropomorphic, forensic, and archeological applications of computed tomography have been developed. [12.] This chapter covers the typical tissue engineering applications and they are summarized in Table 3.1.

The tissue engineering applications of CT can be divided into two categories; visualization and quantitative calculation of structural parameters of tissues and biomaterials. The CT is used to visualize the specifics of surface morphology, internal microstructures and biological processes from 2D and 3D images. In addition comprehensive image data is used to calculate numerical values for various parameters which can be used to assess the functionality of biomaterials and engineered tissues. [1.] First biomedical μCT studies in human medicine were examinations of trabecular 3D structures of bone pioneered by Feldkamp *et al.* at the end of the 1980's. Since then, various μCT applications are being explored which include characterization of scaffolds, regenerated tissue and vascular networks. [28.] Biomaterials and tissues have been scanned in air [6; 14; 20; 41], *in vitro* [27; 68] and *in vivo* [53; 60; 81].

In scaffold research, μCT image data has been applied to determine numerical values for crucial architectural parameters from complex structures. These values can be used to optimize scaffold design and fabrication process [12; 14; 28; 34; 40]. Scaffold

characters such as porosity degree, pore size, interconnectivity, surface area to volume ratio, wall thickness, anisotropy, cross-section area, volume and density have been determined using different image analysis techniques in earlier studies [6; 14; 20; 28; 34; 40; 45; 47; 65]. Applying of more sophisticated image analysis algorithms it is possible to assess also certain functional parameters such as conductivity, diffusivity, elasticity and permeability [6].

The relationship between mechanical strength and microstructure of the scaffold has been studied using computed tomography in order to optimize the mechanical properties for certain tissue engineering application and to inspect the scaffold behavior under mechanical load. The relationship between scaffold structure and elastic modulus, compressive strength and pullout strength has been studied. Yue *et al.* showed the ability of synchrotron radiation μCT for continual monitoring of the pore structure under compression allowing to demonstrate the failure mechanism of scaffold while obtaining stress–strain data. [81.] Computational mechanical analysis of structure has also been tried to perform using μCT-based finite element models (FEM) of bone scaffolds. [22; 32; 59] FEM is considered as an attractive alternative to conventional destructive mechanical testing as simulations can be performed non-destructively via computations [28]. Computational modelling of flow-induced shear stress distribution within 3D polymeric scaffold has been studied using CT image data [77]. The use of these computational models and simulations can be used to compare the functionality of different scaffold architectures which may decrease the need to examine suitability of different architectures in practice [75].

Table 3.1. *Summary of common applications of computed tomography in the fields of biomedical engineering and tissue engineering. [14; 16; 26; 32; 43; 51; 75]*

Applications
Assessment of fluid transport through scaffold
Creation of a model for implant design and fabrication
Determination of structural characters
Evaluation of biological behaviour of scaffold and tissues
Measure the composition of materials and tissues
Non-destructive testing in quality control of implants
Optimization of mechanical properties of scaffold
Visualization

CT image data can be used as guide in implant fabrications. The implant models are produced from CT data and then they can be applied in suitable manufacturing methods such as in solid-free form fabrication or rapid prototyping technology. Computed tomography images are used as guides in fabrication of scaffolds and bone grafts for craniofacial defect repair [29; 43] and in planning and positioning of the dental implants [13]. Three-dimensional CT reconstruction models have also been used to simulate flow conditions and media flow through scaffolds [58].

Computed tomography imaging is used to optimize and assess the biomaterial-tissue-relationship by measuring several different variables. Scaffold function has been evaluated *in vivo* by using repeated monitoring over time and quantifying tissue (e.g. bone, vascular and cartilage) in-growth, response and changes within scaffold during regeneration of tissues. Implant performance and degradation kinetics can be evaluated by measuring the changes in the volume of biomaterial or tissue. [8; 26; 80] This technique is applied in earlier studies of bone defect healing [53; 60; 75]. Infiltration of scaffolds with vascular structures is visualized and also various vessel parameters are determined quantitatively including vessel volume, thickness and connectivity. [18; 26] Cell adhesion and proliferation on the inner surface of the scaffold has also been studied with μCT [16].

The ability of image analysis to distinguish different material phases from CT images is applied to quantitatively determine the amount of each existing region from biomaterials and tissues. Recognition of amorphous and crystalline phases of biomaterials [7], pore and filler ratio of composite scaffolds [51] as well as the analysis of cartilage matrix composition and morphology [55] is studied using image data. In the studies of cartilage matrix, detecting and quantifying proteoglycan content and distribution was successful using negatively charged ionic contrast agents [55]. Computed tomography is observed also to be useful tool in quality control related to scaffold fabrication processes [75] as well as in industrial field [23; 73].

3.4. Image analysis

Several structural characteristics of scaffolds and tissues can be numerically calculated using obtained CT image data. Image analysis requires sufficient hardware and software facilities. [26.] Analyze, ImageJ, Mimics, Tview and VG studio MAX are applied software for scaffold analysis [15; 17; 21; 28; 81]. Preprocessing, prior calculations, typically includes evaluation of image quality, selecting the volume for analysis and segmentation of images. These steps must be carefully solved in order to get reliable results from calculations [4; 26]. The general principle of the four main phases of image analysis process is described in this chapter.

Image quality assessment

Quality assessment of gray scale images is usually based on visual assessment but the assessment can also be based on measurements. The objective measurements allow CT systems to be rated by quantifying the factors which affect image quality such as resolution, contrast and noise. These factors can be compared with the different systems and thus information of imaging system performance is produced. The modulation transfer function and contrast-to-noise ratio are techniques which are applied to measure image quality. The modulation transfer function is a graphical description of the blur or resolution characteristics of imaging system. [72.]

The main interest in visual evaluation is usually image contrast and how easily can the object to be distinguished from the background. Visual assessment is considered relevant technique in clinical diagnostics. If the quality is not sufficient the reliable determination of structural characteristics cannot be achieved in spite of how skilled image analysis there would be. Common factors which affect the image quality are described in Chapter 3.5. [4; 72; 80]

Volume selection for analysis

A crucial step before image-based characterization is to select the volume of interest (VOI). The series of pictures in Figure 3.4. illustrates the principle of volume selection from 2D image set for image analysis.

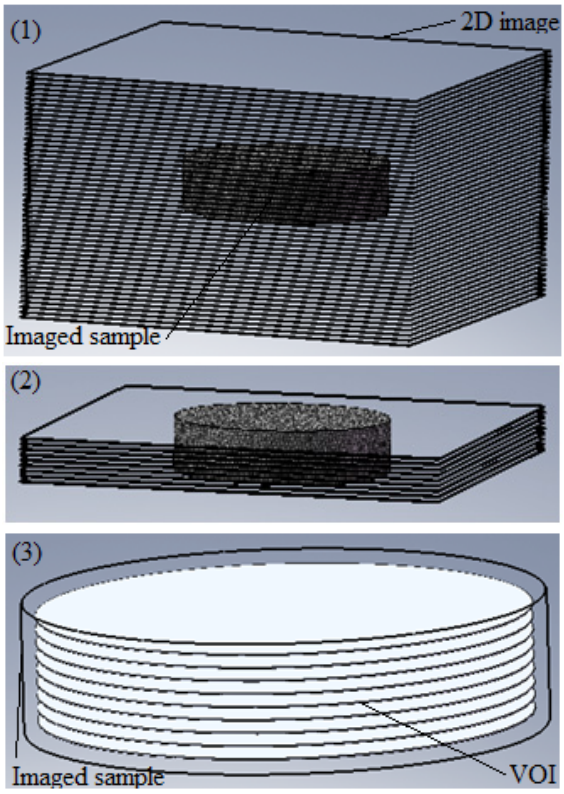

Figure 3.4. *Principle of volume selection from 2D image set. Volume of scanned sample in measuring field of CT device (1), extra slices are cropped (2) and empty space from each remaining 2D image is cut (3) resulting volume which is slightly smaller than sample volume. The pictures were modelled using the CAD programme during the present study.*

Volume selection means that the sample volume is distinguished from the measuring field volume of CT device. Because both sample volume and measuring field varies using different samples and CT devices, the different volume selection is needed in each different study. For example in the study of Darling & Sun they obtained 500 sequential 1024 x 1024 pixel images from each sample but they selected only 62 sequential 200 x 200 pixel images for image analysis. [14.]

A rectangular prism in Figure 3.4. illustrates the measuring field of CT device (1) which consists of stacked sequential gray scale 2D images. Those two-dimensional images form a volumetric 3D image. [6.] A dark cylindrical body located in the middle of prism describes imaged sample. The extra empty volume around the sample volume needs to be cropped vertically and horizontally [21]. Vertical outlining can be performed by selecting only those 2D images which has collected information from the sample (2). Horizontal outlining in turn can be performed by trimming each remaining 2D image according to the shape of the specimen. Finally the extra empty space is completely removed around the sample volume (3) resulting much smaller remaining image volume for analysis. In earlier studies the analyzed volume is selected so that it covers entire scaffold volume [41] or only the core regions of the sample [14] and this selection determines how comprehensively the analysis describes the sample structure.

Image segmentation

Accurate segmentation of obtained images into different regions is essential to the reliable image analysis both in biomaterial characterization and in patient diagnosis. Segmentation can be performed manually by analyzer but there are also several automatic techniques available in literature. Some of the techniques are based on the gray level histograms, some use spatial details while others employ statistical shape models. Conventional segmentation techniques include edge detection and histogram threshold techniques. More sophisticated methods include region growing and different types of deformable models which are developed to overcome the limitations of conventional techniques. [56.] Thresholding is commonly used segmentation technique in earlier biomaterial studies and therefore the technique is described more deeply in following paragraphs [61; 80].

Thresholding is a technique used to identify and distinguish different areas of images. In the case of scaffolds it means empty pores from scaffold material phases. In more detail indicated thresholding identifies the intensity value of image that optimally separates the pore from the solid. [61.] The effect of applied threshold level on visual view of CT image is demonstrated in Figure 3.5., which is taken from the study of Yang *et al.* where their aim was to optimize the amount of contrast agent necessary for X-ray imaging of polymer blend scaffolds. The scaffold structure is viewed as a solid block at the threshold of 0 and 10 while thresholds of 50 and 109 produced realistic images of scaffold architecture. [80.] Similar observations were made in the study of Duvall *et al.* They studied the vasculature of hindlimb of mice with μCT showing that the increase in threshold decreases the vascular volume and amount of vessels. Alteration of the threshold value effect both visual view and on the calculated morphometric parameters. [18.] Figure 3.6. illustrates the dramatic effect of thresholding to the image-based calculated porosity degree values. The exact relationship between the threshold and primary parameters varies depending on the scaffold. [61.]

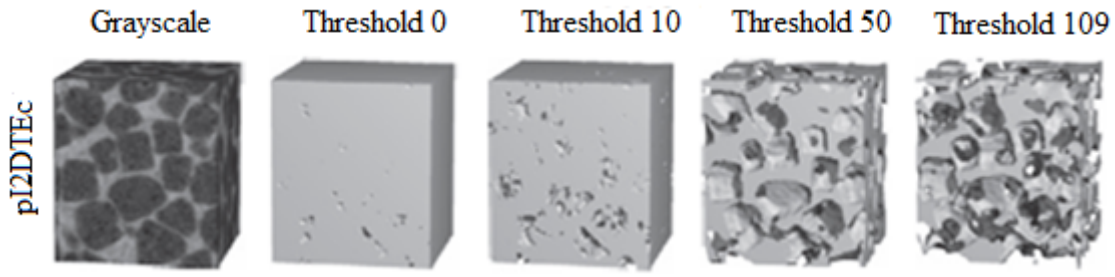

Figure 3.5. *Iodinate analog of poly(desaminotyrosyl-tyrosine ethyl ester carbonate) (pI_2DTEc) scaffold 3D reconstruction at several different threshold values demonstrating the effect of applied threshold level to a visual view of CT image. [Modified 80]*

The threshold level can be set manually or by using automatic threshold methods. Both techniques contain advantages and drawbacks. The reliability of manual selection of threshold level is based on visual assessment which is not always the most recommended method because several factors may disturb its functionality such as room lighting, monitor brightness and contrast, randomness in pore-solid distribution and limited gray-scale shade perception. [61.] However, some researchers have stated that manual selection of threshold levels yield the best results [4]. Also applying of a single manually adjusted threshold value through all images may not be recommended because of disturbing inherent noise in the imaging system and material and structural imperfections in the scaffold [61]. In addition using a single threshold value across specimen is always a compromise between not over-estimating the volume and not missing smaller regions and thus is not always recommended [26; 61].

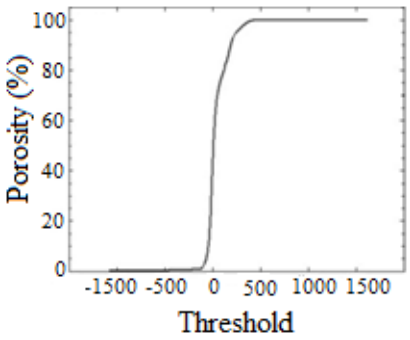

Figure 3.6. *Sensitivity of porosity to thresholding. [Modified 61]*

The automatic threshold methods calculate the threshold levels using different algorithms. The automatic techniques can be classified based on the background theory of an algorithm. There are for example algorithms that determine intensity values based on entropy and histogram. Histogram represents the distribution of the gray values in images and they can be utilized to distinguish different materials and tissues from images. Applying of the grey level histogram of the image, the threshold can be selected between the two peaks of the histogram, which represent the two different materials or tissues. [6; 44] Threshold methods can also be classified to global and local techniques. Global thresholding exploits the correlation between pixels on a global scale whereas

local methods adapt the threshold value locally depending on regional image characteristics. [61.] For local methods the threshold is computed for each pixel according to the image characteristics within a window of radius **r** around it [21].

Calculation of structural parameters

Computed tomography imaging allows the determination of several structural parameters using either 2D or 3D images. Quantitative determination of material, tissue or pore volume is based on that images are thresholded with separate values for each existing material phase. Thus the share of empty space, biomaterial, soft tissue and hard tissue can be distinguished because they represent different intensity values in image pixels. [7; 26] On the other hand, if there are two materials representing same gray levels, their separation could be challenging. Because the gray levels depend strongly on material density, two materials having nearly equal densities could not be easily distinguished from images. [34; 51] For instance, Djukic *et al.* studied carbon fiber polyester composites and reported that the separation of carbon from polymer phase was problematic [15].

Niemelä *et al.* previously studied the composition of polymer matrix composites and distinguished polymer, filler and pore space using manually set threshold values. After thresholding they managed to determine volume ratios of each phase and also studied the distribution, shape and size of fillers using suitable image analysis algorithms. Figure 3.7. represents the thresholded 3D reconstruction core of the sample where filler material is remained visible (white regions) and polymer phase is thresholded invisible. [51.]

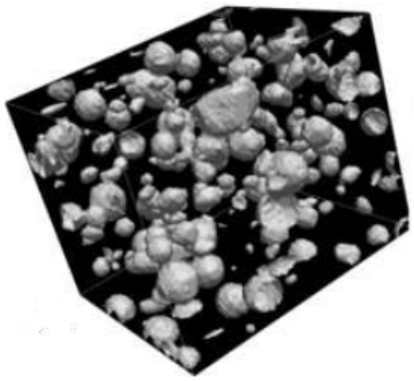

Figure 3.7. *Three dimensional μCT reconstruction of the core volume of poly-L/DL-lactide-bioactive glass composite scaffold. The threshold levels are set so that only filler phase (bioactive glass) has remained visible. [Modified 51]*

Image based characterization of scaffolds can be performed using suitable computerized image analysis program or algorithm which automatically analyze the thresholded data and calculate numerical values for structural parameters. For example Pore Analyzer – program (developed during MIKAMA project) can be used to determine several architectural parameters from 3D reconstructed images such as degree of porosity, pore volume distribution and volume fractions. Some parameters can also be determined

using 2D image(s). In earlier studies, pore sizes are determined by measuring the mean pore width from a 2D image using drawn lines. The distance between the points, where the lines intercepted the pixels of the scaffold matrix was measured. [44.] This method is used in characterization of SEM [47], CLSM [44] and μCT images [14]. Also wall thickness can be calculated from two dimensional images using similar technique than in pore diameter determination [40; 47]. Volumetric 3D image analysis is considered as more reliable characterization method than 2D analysis. The 3D analysis describes better the entire scaffold network. For example, in 3D pore analysis, each individual pore can be analyzed as a separate 3D volume and parameters such as mean pore diameter can be determined applying sufficient algorithm. [34; 51]

Inverting the threshold is useful when pore interconnectivity is studied and pore network is visualized. Inverting changes the thresholds of the gray scale images reversed and thus allows measurement of the volume of all empty spaces (pore spaces) of the images. [14.]

3.5. Limitations of CT in biomaterial studies

In spite of versatility of CT in tissue engineering and biomedical applications, the technique is not without its limitations. Drawbacks are associated with applied CT system and image analysis process. [26.] This chapter covers the generally observed problems related to CT image acquisition and image analysis.

Artifacts

Artifacts are image errors which may reduce image quality or completely destroy the diagnostic value of the image. Artifacts may originate due to a variety of sources and it is possible to group the origin of the artifacts in four categories; patient based artifacts, scanner based artifacts, physics based artifacts and helical and multi-slice artifacts. Patient based artifacts may be caused by the patient movements, patient positioning partly outside the focus or presence of metallic materials. Metallic materials may cause streaking artifacts because the high density of metal cannot be handled by the computer. Scanner based artifact can be caused by the detector which is out of geometric calibration resulting ring artifacts. [5.]

There are several different types of physics based artifacts including partial volume effect and beam-hardening which can result from the physical processes involved in the acquisition of CT data [5]. Beam hardening artifacts are commonly observed if the scanned sample contains two or more materials which have different abilities to absorb X-ray irradiation or if the thickness of the object varies. For example, these artifacts are observed in images when soft tissue is scanned together with metal or bone. [12; 15; 33] An X-ray beam is composed of individual photons with a range of energies and the thicker sections of the object absorb more low energy photons than a thinner section. The beam artifact can be generated as the beam passes through an object resulting that its mean energy increases because the lower-energy photons are absorbed more rapidly

than the higher-energy photons. This increase in mean energy of beam is called beam hardening. Beam hardening can result that scanned materials which have the same absorbing ability of radiation may be seen on different intensities in images. [5; 33] Beam hardening artifact can emerge in images either as cupping artifacts or dark streaks between dense objects. Last mentioned type of beam hardening artifact is illustrated in the left picture in Figure 3.8. and in the right picture is the same image after artifact correction. [5; 12]

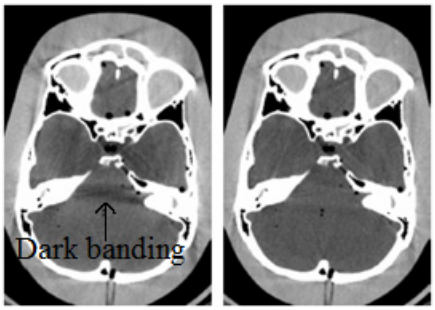

Figure 3.8. *Beam hardening artifact and its correction illustrated in CT images of posterior fossa. The dark banding between dense objects in left picture describes the artifact. The right picture is the same image after beam hardening correction. [Modified 5]*

The helical and multi-slice artifacts include helical artifacts and cone beam effect artifact. These types of artifacts are related to the applied image reconstruction method and can occur in helical and multi-slice scanning. Helical artifacts can be caused by the rapidly changing structures in the z direction. The cone beam effect is related to multi-slice devices and the artifact is caused by the imperfections of rotating detectors. [5.]

The artifact removal may be necessary to perform for images after scanning. Corrections can be done by proper software. Also manufacturers minimize beam hardening using filtering system in CT. [5.] Radiation is filtered before it reaches the sample. The filtering reduces the number of X-ray amount while increasing the average energy of the radiation. Thus beam-hardening artifacts are reduced during image reconstruction as well as the dose to which the sample is exposed. The filtering could be done with thin aluminum or copper sheets which are installed next to the X-ray tube. [12.] Artifacts can also be minimized by positioning specimen carefully and using optimum selection of scanning parameters [5]. Scanning parameters in CT imaging, including anode voltage and current, has a crucial effect on image quality, the patient's radiation exposure and economic efficiency of imaging. Radiation dose should be kept as low as reasonable achievable and it can be done by optimizing the scanning parameters to minimum. However, the potential drawback in low imaging parameter values is an increase in image noise. Therefore, it is essential to tailor imaging parameters to the individual target sample in order to obtain diagnostic images. [57] Because of several artifacts, CT imaging of scaffolds containing metals or metallic implants is not recommended [5; 26].

Lack of contrast and contrast enhancement

Contrast in X-ray image is affected by generated radiation but also sample material properties such as thickness, density and chemical composition has a huge effect on quality of resultant images [15; 33; 80]. Bone as a hard tissue and ceramic materials such as glass, hydroxyapatite (HA) and calcium phosphate (CP) usually possess sufficient contrast. X-ray attenuation in bone is largely caused by the mineral crystals. [6; 15; 22; 34; 75] Instead, a common problem related to CT imaging of low density polymers and soft tissues is that they may not possess sufficient X-ray contrast which results in poor image quality. Conventional polymers and soft tissues have similar radio-opacity due to that they consist mainly of carbon, hydrogen, oxygen and nitrogen. To overcome this limitation, there are applied several techniques for improving the absorbing ability of X-ray irradiation in previous tissue engineering studies and also in medical field. [12; 15; 24; 80] Applied contrast enhancement techniques are described in this chapter and summarized in Table 3.2.

Contrast medium is commonly used in clinical studies to improve the X-ray contrast of tissues. Contrast agents change the density of desired target (e.g. vessels or intestines) so that it differs from environment. Two most common clinical contrast agents are iodine and barium. Contrast of tissue engineering constructs has been enhanced by adding heavy atoms such as barium, bismuth, copper, gadolinium, gold and iodine to sample. The heavy atoms and polymers can be combined as physical mixtures of salts, blends with organic compounds and covalent linkage of heavy atoms to the polymer backbone. Heavy atoms can also be added to the sample by coating [15; 33; 80].

Yang *et al.* enhanced the radio-opacity of polymer scaffold by blending the poly(desaminotyrosyl-tyrosine ethyl ester carbonate) (pDTEC) with an iodinated-pDTEc analog (pI_2DTEc) [80]. Djukic *et al.* studied the polymer matrix composites with μCT by modifying and coating the samples with aluminium oxide resin additives and with several heavy atoms and they reported that, gold, copper and iodine coatings were the most successful techniques. [15.]

Radio-opacity of soft tissues is improved by staining and perfusion. Dorsey *et al.* studied the cell adhesion and proliferation within polymer scaffold and applied toxic osmium tetroxide to enhance the visibility of cells in μCT images. Osmium is a heavy metal that stains the cell membranes. [16.] Perfusion of radiodense silicone rubber contrast medium containing lead chromate is applied to enhance the contrast of vascular networks of murine hindlimbs by Duvall *et al.* [18]. Perfused contrast agent, which polymerizes within the vessels, creates a stable radiodense cast through the vasculature following immediately death. Present perfused contrast agent technique could also be used to visualize and quantify the infiltration of scaffold with vascular structures [26; 60]. Palmer *et al.* applied iodine contrast medium in studies of cartilage extracellular matrix synthesis within biomaterials. Proteoglycan content was determined by imaging the equilibrium partitioning of an ionic contrast medium via micro-CT. [55.] For tissue

engineering applications, it is often preferred that the contrast medium is non-toxic. Lipiodol is non-toxic poppyseed oil which is used in human radiological studies and also in studies of scaffolds. [75.]

Table 3.2. *Applied heavy atoms and techniques for improving radio-opacity of biomaterials and tissues. [15; 16; 18; 55; 75; 80]*

Contrast atoms	**Techniques**
Barium	Blending
Bismuth	Coating
Copper	Covalent linkage
Gadolinium	Perfusion
Gold	Physical mixture of salts
Iodine	
Lead chromate	
Lipiodol	
Osmium	

A few matters need to be taken into consideration when using contrast medium. The inclusion of radiocontrast agents may cause unwanted changes to physiochemical properties and performance of the implant. The biocompatibility and structure should maintain after sample manipulation. [80.] The unwanted structural changes, such as thickening of the sample fiber, are observed drawbacks during coating processes in earlier studies. Fiber thickening may affect also to other parameters including porosity degree and pore sizes. Mentioned challenges can be overcome by determining and using the minimum required amount of contrast atoms. Each available contrast medium is not biocompatible and thus the suitability of these substances varies according to the application. [64; 80]

Thresholding in analyzing biomaterials

Two common challenges in image-based characterization are the absence of a single universally applicable automatic threshold technique and the lack of objective measures which automatically assess the performance of the threshold techniques. The suitability of available thresholding methods needs to be somehow estimated so that the correct threshold levels will be chosen for the structural characterizations. The suitability of threshold techniques is usually done visually by comparing the representative 2D grayscale image and thresholded images visually side by side. [26; 61] Also SEM images and histological sections of same sample are used as guide in thresholding [4; 26].

Maspero *et al.* studied PLGA scaffold structure and assessed the suitability of threshold method by imaging first more simple PLGA structures which were easier to analyze. The threshold levels were set first to images of simple structures and same threshold levels were applied for more complex scaffold geometrics afterwards. [44.]

The evaluation of thresholding can also be done by comparing the structural parameters which are calculated using image-based methods and using other techniques. In earlier μCT studies, the porosity degree of scaffolds is commonly calculated using theoretical calculations and mercury intrusion porosimetry (MIP). Calculated values are compared and it allows assessing the correctness of applied threshold levels. [41; 61] However, one must notice that threshold levels have not been necessarily set correctly even if the method produced the desired values from structural determination. This is due to that two or more visually different images can provide identical porosity degree [61].

In the evaluation of the threshold method, attention must be paid to that any method cannot be considered universally applicable and being suitable for all scaffold images. So the threshold technique must be always chosen, case by case. [61.] For example applying of few global threshold levels would probably work well for detection of bone formed within low attenuating polymeric scaffold. However, more sophisticated threshold methods may be needed to distinguish multiple materials with overlapping density distributions [28]. In case of variable attenuation levels or very thin structures, it is recommended to report data at more than one threshold value [26].

Size of measuring field

Measuring field or focus describes the volume in which the CT device collects information during scanning. The size of focus varies between different CT types. High resolution micro-CT scanners usually contain a measurement chamber where the object is placed on a rotating specimen disk where the maximum sample size varies from 15-40 mm in diameter and 30-80 mm in length. According to technical specification of Planmeca ProMax 3Ds dental CT (Appendix 1), the maximum size of measuring field is a cylindrical Ø50 mm x 80 mm volume. [25; 74] Many clinical CT systems enable even whole body scans. A small measuring field could be a limitation in CT characterization. For example, high resolution micro-CT scanners may not be suitable for medical applications due that the X-rayed size of focus is in general only of a few cubic centimetre. [12.]

Spatial resolution

The resolution is a measure which describes how small details can be distinguished from the image [33]. The visual view of images is significantly dependent on the scanning resolution of the CT device and the dramatic effect of resolution to image-based calculated parameters are also showed in previous studies. Aydogan *et al.* studied the bulk aluminium oxide (Al_2O_3) samples and showed that the resolution of the analyzed images has a significant effect on the image-based determined porosity values [4]. Duvall *et al.* studied the vasculature of mice hindlimb using μCT with different resolutions and showed that the vascular volume and amount of vessels decreased as voxel size increased. The effect of image resolution to visual view of hindlimb

vasculature is illustrated in Figure 3.9. The difference is immediately obvious as the smaller caliber vessels cannot be visualized with larger voxel size. [18.]

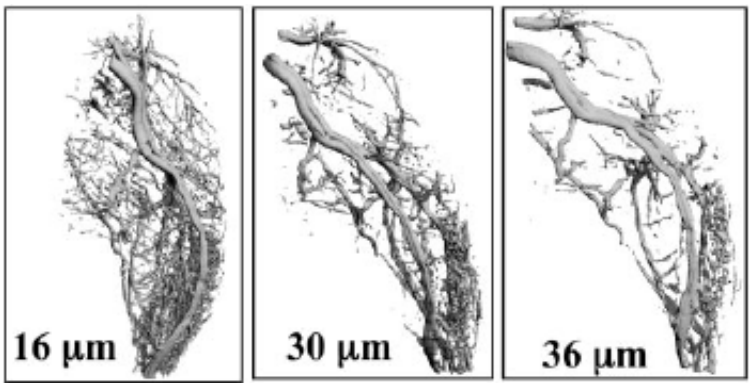

Figure 3.9. *Rendered 3D images of vasculature of mice hindlimb where the same sample was scanned with µCT using three different resolutions. Image voxel sizes are presented in the lower left in the images. [18.]*

The resolution of µCT ranges typically between 1-50 µm but with synchrotron radiation nano-CT may have even 0.1 µm resolution [44; 75]. The size of the focus, the size of the detector elements and the mechanical accuracy of the rotary motion determine spatial resolution in µCT [12]. The resolution required for analyzing tissue formation and vascular in-growth within porous scaffolds is stated to be in the range of 1-30 µm [26]. Scaffold characterization in earlier studies is performed using CT images with resolution ranging from few micrometers to 20 micrometers [14; 41; 44; 46]. Drawback of using smaller resolution in normal laboratory based µCTs is observed to result in longer scanning times and much larger data sets [18].

4. CHARACTERIZATION TECHNIQUES FOR POROUS STRUCTURES

Various techniques, besides CT, are previously used for characterization of the structures of tissue engineering scaffolds and other porous constructs. Each technique produces different information from the object. [28.] In this chapter, applied techniques for structural characterization of biomaterials are introduced and categorized.

4.1. Theoretical methods

Theoretical calculations are used for determination of porosity degree of biomaterial products in earlier studies [47; 70]. They have also been used as a comparative method when the porosity of biomaterial product is defined using more sophisticated methods such as computed tomography [34; 41; 44]. Existing theoretical methods include Archimedes method, liquid displacement, mass technique and unit cube analysis. The two latest mentioned are the main theoretical approaches but Archimedes method and liquid displacement technique are based on similar concepts with only slight variations. Basic equations of unit cube analysis (Eq. 2) and mass technique (Eq. 3) are presented below. The precondition for the reliability of the unit cube analysis is, that the structure of the sample is regular (e.g. honeycombed). The mass technique is more suitable for complex geometries such as for irregular fibrous scaffolds. [28.]

$$Porosity\ degree\ = \left(1 - \frac{V_f}{V_a}\right) 100\% \qquad (2)$$

Produced outcome of theoretical methods are commonly deemed as estimates of porosity. The reliability of both methods is dependent on the accuracy of linear measurements of the specimen as inaccurate volume measurements results errors in calculated porosity values. [28; 44]

$$Porosity\ degree = \left(1 - \frac{V_g}{V_a}\right) 100\% \qquad (3)$$

Equations (2) and (3) look nearly similar except the parameters V_f and V_g which both describes the volume of scaffold material but are differently defined. Parameter V_f is calculated from known deposition pattern according to equation $V_f = \pi L d^2 n_1 n_2 / 4$ where L, d, n_1 and n_2 describes the strut length (L), the strut diameter (d), the number of struts per layer (n_1) and the number of layers per scaffold (n_2), respectively.

Parameter V_g follows more simple equation $V_g = m/\rho$ where m and ρ describes mass of the scaffold (m) and density of the scaffold (ρ). Both equations (2) and (3) include the parameter V_a which describes the scaffold cube volume which is the arrival of the scaffold height (h), the scaffold width (w) and the strut length (L). [28.]

Mutanen and Sippola defined the porosity degree of joint scaffolds in their studies using mass technique. [47; 70] Porosity values from Mutanen will be used as reference values in this work and the results from her study can be found from Appendix 2 [47].

4.2. Conventional methods

There are techniques such as mercury and flow porosimetry, gas pycnometry and adsorption, immersion microcalorimetry technique and photon density wave technique, which allow characterizing porous structures such as tissue engineering scaffolds [19; 28]. Ability to define parameters varies between different techniques as for example gas pycnometry can be used to measure only material volume and porosity degree of the scaffold. Instead gas adsorption technique allows defining several parameters including porosity, pore sizes and shapes, pore volume and cumulative pore size distribution. [28.]

Mercury intrusion porosimetry (MIP) is commonly used technique for characterization of porous scaffolds [41; 44; 46]. The technique is based on that liquid mercury is forced into structure by applying slowly increased pressure. Total volume of penetrated mercury is measured when pressure is at maximum and compared with bulk volume of sample which is determined before penetration. The determination of architectural features is based on the recorded intrusion and extrusion curves. Curves describe the recorded volume of intruded and extruded mercury at each pressure step. [19; 28]

Mercury intrusion porosimetry (MIP) allows defining various parameters including open pore volume, porosity degree, permeability and surface to volume ratio. Pore sizes, ranging from 0.0018 µm to 400 µm, can be studied using MIP. [28.] The technique is at its most accurate when the pore interconnectivity of scaffold is 100 % because MIP does not account for closed pores. Thus in practice measured porosity degree may be a slight underestimation of that true porosity. [61.] Other error factors in MIP characterization may occur from the inaccurate sample volume measurements and from small pores (< 0.0018 µm) which are not intruded with mercury [28; 44]. The toxicity of mercury and elevated pressure makes this technique destructive in polymer scaffold characterization. Elevated pressure also limits methods usability from flexible compressible scaffold design. [19; 28; 44] Mercury reacts with metals such as gold and aluminum to form amalgams, and therefore mercury intrusion porosimetry is not sufficient technique for characterization scaffolds which contain those types of metals [28; 61].

4.3. Imaging techniques

There are several imaging techniques applied for scaffold characterization. Some of them produce 2D images and others enable to produce also 3-dimensional images of the target. Microscopes such as scanning electron microscope (SEM) [44; 46; 76; 80], fluorescence microscopy [16; 17] and atomic force microscopy (AFM) [69] are applied for 2D characterization and visualization of biomaterial structures and cell culture in scaffolds.

Two-dimensional images can be used to achieve visual estimation of microstructure orientation, interconnectivity, cross-section area, anisotropy and morphology of scaffolds. In addition, 2D analysis allows direct measurements of pore diameter and wall thickness. [28; 44; 46; 62] A significant limitation using 2D techniques is that the outcome of these measurements does not always describe truly the 3D structures because a lot of information is lost when characterization is based on analysis of single 2D images [19; 28]. For example, SEM allows to measure pore diameter and wall thickness but offers only qualitative information on porosity and pore interconnectivity [28]. In addition, no quantitative data from pore volume and pore size distribution can be obtained with SEM [19]. Other limitation in characterization of internal structure using these morphological techniques is that they require destructive sectioning of the sample which may cause also compression and edge effects to the scaffold architecture, thereby compromising the results [44; 62].

Confocal laser scanning microscopy (CLSM) [44], multiphoton microscopy (MPM) [42] and optical coherence tomography (OCT) [67] enables to acquire information from 3D structures but these techniques enable to characterize only very thin structures. CLSM allows imaging to a depth of approximately 0.1-1.0 mm and OCT can up to three millimeters. CLSM has poor imaging depth due to the low optical penetration of light into non-translucent biomaterials such as bone, ceramics and many synthetic polymers. [66; 67] In a study of Liu *et al.*, they succeeded to quantify the microstructures of porous biodegradable polymer scaffold using MPM only to a depth of a few hundred microns without the destruction of the sample. However, they succeeded to quantitatively analyze the porosity, pore size distribution and pore interconnectivity. [42.]

Magnetic resonance imaging (MRI) is introduced to the field of tissue engineering but it is still rarely used to study biomaterial scaffolds, probably because of the poor spatial resolution of clinical scanners (approximately 100 μm) and their temporally limited availability for researchers. Also high installation and running costs of common MRI devices as well as relatively slow image acquisition has been limitations for their use. However MRI overcomes some limitations related to optical and X-ray imaging, such as poor dept penetration and radiation damage. [36; 52; 79]

MRI, compared to the other imaging techniques, has the highest sensitivity for visualizing soft tissue and therefore it has been used in studies of soft tissue properties including tissue relaxation time, water diffusion coefficient and stiffness. MRI can also

quantify cell death, assess inflammation and visualize gene expression. In addition, high resolution MRI (slices less than 100 μm) can be used to characterize the structure and composition of regenerating tissues. [79.]

Magnetic resonance imaging can be used for continuous and non-invasive *in vivo* imaging of implants. MRI has been used for the optimization of tissue engineering structures and creating 3D models as guides for fabrication process of implants [52; 71]. Mass transport between scaffold and surrounding medium is investigated using MRI [52]. Also implant-tissue interaction and biological responses to polymer implants are studied *in vitro* and *in vivo*. Occurrences such as hydration, swelling and erosion of implants as well as implant encapsulation have been detected using MRI [36; 60].

The outcome of CT and six introduced characterization techniques is compared in Table 4.1. The ability of these techniques to define eight common parameters is summarized.

Table 4.1. *The suitability of common techniques to define eight typical characters from porous structure. Symbol "+" means that technique can define character and symbol "–" means that it cannot. Abbreviations GA, GP, FP and TM describe gas adsorption, gas pycnometry, flow porosimetry and theoretical methods, respectively. The column "Other parameters" describes that could the method allow determine also other parameters that included in the table. [Modified 28]*

	CT	**SEM**	**MIP**	**GA**
Porosity	+	Qualitative	+	+
Surface area/volume	+	-	+	-
Pore size	+	+	+	+
Permeability	+	-	+	-
Strut thickness	+	+	-	-
Anisotropy	+	Qualitative	-	-
Cross section area	+	Qualitative	-	-
Interconnectivity	+	Qualitative	-	-
Other parameters	Few	Nil	Few	Few
	GP	**FP**	**TM**	
Porosity	+	-	+	
Surface area/volume	-	-	-	
Pore size	-	+	-	
Permeability	-	-	-	
Strut thickness	-	-	-	
Anisotropy	-	-	-	
Cross section area	-	-	-	
Interconnectivity	-	-	-	
Other parameters	Nil	Few	Nil	

The optimal characterization technique should at least provide a comprehensive set of information from studied porous structures. The most attractive approach would be to find out a single method which produces all necessary information from specimen. However, as this chapter showed, usually a combination of several techniques is needed in practice. [28.]

5. BENEFITS OF COMPUTED TOMOGRAPHY

Each existing characterization method contains different individual properties which define the suitability of the technique to study porous biomaterial structures. In this chapter, the advantages of computed tomography imaging as a characterization technique are described and also the properties of CT and other techniques are compared.

Computed tomography has become a very popular technique for porous biomaterial characterization probably due to its versatile properties which other techniques lack. CT enable to visualize biomaterial internal 3D structures which is a significant advantage compared to the theoretical and conventional methods. In addition, computed tomography allows characterizing all kinds of geometrics including compressible and flexible structures whereas the suitability of other methods, including MIP and unit cube technique, depends significantly on sample architecture. Digital CT image analysis also enables to study either a desired part of the sample or entire 3D scaffold network and the internal features of the same sample may be examined multiple times over time. [25; 28]

Computed tomography has also advantages compared to the other imaging techniques. CT allows the characterization of significantly thicker objects than SEM, CLSM and MPM. The measuring field of CT varies from the size of the whole body parts of human down to the nanometer scale of a single cell. The 3D nature of sample can be described throughout from CT images providing both qualitative and quantitative information of objects. 2D imaging techniques produces mainly qualitative information on structural parameters due to low imaging depth and that decrease the reliability of characterization. [12; 28; 46; 54]

Micro-CT enables accurate determination of various different characters from porous biomaterials. Accuracy is mainly from the sufficient spatial resolution of μCT (~1-50 μm) for scaffold research. [44.] The spatial resolution of mentioned 2D techniques is also sufficient for characterization of thin and porous biomaterial scaffolds but normal magnetic resonance imaging devices instead might have a little too rough accuracy for that application [67; 79]. Also image analysis counts entire structure without missing any parts of it. If the porosity determination using CT and MIP are compared, MIP does not count for the closed pores which may lead to underestimation on calculated porosity. [44; 46]

CT is considered as a non-destructive characterization method which does not require the use of toxic chemicals in samples. Even if 2D imaging techniques allow non-destructive scanning, however, the study of internal parts usually requires

sectioning which ruins the sample. Also the use of high pressure and liquid mercury in MIP technique makes the inspection destructive. [28; 44] The non-destructive nature of CT can be utilized for quality control before implantation such that only those that fulfill certain criteria will be placed. The intact samples can also be subjected to other tests after scanning. [54; 75]

Computed tomography and magnetic resonance imaging enable to study biomaterials in air, in bioreactors *in vitro* and in living organisms *in vivo*. Theoretical and conventional methods as well as 2D microscopic methods allow only characterization in air. Bioreactors provide the opportunity to study the effect of culture parameters on tissue growth and differentiation. *In vivo* CT imaging provides noninvasive and precise 3D measurements of scaffold architecture as well as assessment of new tissue formation without the surgical extraction of the implants [36; 75]. Histology has been a standard method for evaluating biomaterial-tissue reactions and tissue formation within the scaffold. Destructive nature, difficulty of sectioning and potentially misleading representation of 3D tissue formation are observed drawbacks in histology studies which could be avoided using computed tomography imaging. [26; 75]

EXPERIMENTAL PART

6. MATERIALS AND METHODS

All the samples studied in this work were bioreconstructive joint scaffolds designed for small joint (metacarpophalangeal joint) reconstruction [30; 31; 78]. This chapter covers the introduction of applied materials, different sample types and manufacturing method. Also the scaffold modification techniques for X-ray contrast enhancement as well as mass, dimensions and structural characterization methods are described.

6.1. Joint scaffold materials

Poly-L/D-lactide 96/4, chitosan and bioactive glass were used for joint scaffolds. The basis for all the scaffolds was polylactide whereas chitosan and bioactive glass were additional materials. All the applied materials were bioabsorbable and well-known.

P(L/D)LA 96/4 raw material was purchased from Purac biochem, Gorinchem, Netherlands under the trade name Purasorb PLD. Medical grade L-lactide/D-lactide copolymer, with an L/D isomer ratio of 96/4, granules had original inherent viscosity of 5.48dl/g and melting range between 158.5-165.8°C. [47; 70]

Applied chitosan was analytical grade with 73 % deacetylation and a molecular weight of 240 kDa. Raw chitosan powder had an average particle size < 100 µm and percentual dry weight of 91.40 %. Bioactive glass was type of 13-93 (of Na_2O 6.0 mol-%, K_2O 7.9 mol-%, MgO 7.7 mol-%, CaO 22.1 mol-% P_2O_5 1.7 mol-%, and SiO_2 54.6 mol-%). Bioactive glass type 13-93 had original density of 2.65 g/³ and the material was developed at Åbo Academi University. [70.] Photographic and microscopic image of 18 mm P(L/D)LA 96/4 scaffold is illustrated in Figure 6.1.

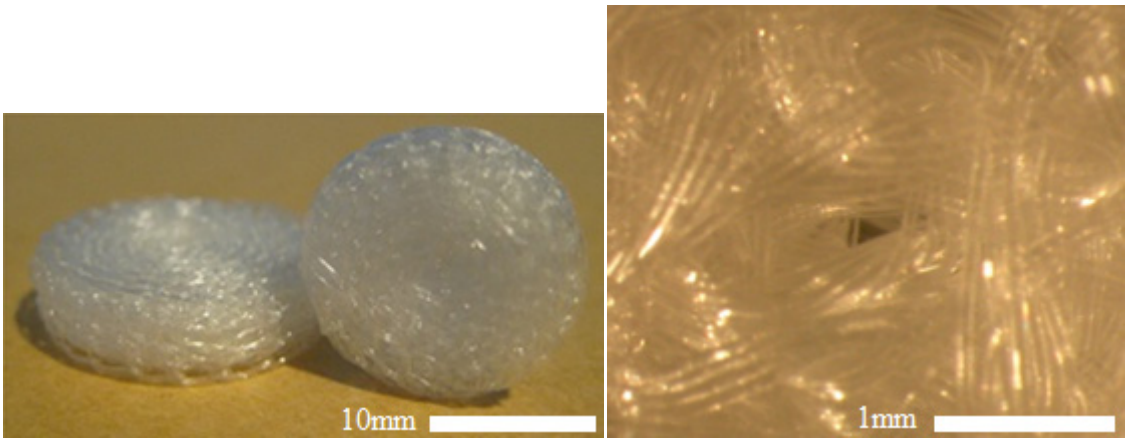

Figure 6.1. *A photographic illustration of gamma irradiated 18 mm P(L/D)LA 96/4 joint scaffolds (left) and a microscopic view showing fibrous structure of the scaffold (right).*

6.2. Joint scaffold types

Altogether five different joint scaffold types were studied and they are presented in Table 6.1. Six sizes of P(L/D)LA scaffolds and one size of P, PC, PG and PCG scaffolds were studied. P(L/D)LA and P type scaffolds consisted only of P(L/D)LA 96/4. PC, PG and PCG type scaffolds consisted of P(L/D)LA 96/4 and chitosan, P(L/D)LA 96/4 and bioactive glass and P(L/D)LA 96/4, chitosan and bioactive glass, respectively.

Table 6.1. *Studied scaffold types, sizes and their manufacturing method.*

Type of scaffold	Materials	Sizes	Reeling
P(L/D)LA	P(L/D)LA 96/4	8, 10, 12, 14, 18, 20	Semiautomatic
P	P(L/D)LA 96/4	10	Hand-rolled
PC	P(L/D)LA 96/4 + chitosan	10	Hand-rolled
PG	P(L/D)LA 96/4 + BaG13-93	10	Hand-rolled
PCG	P(L/D)LA 96/4 + chitosan + BaG13-93	10	Hand-rolled

6.3. Joint scaffold manufacturing methods

The manufacturing methods and design of the joint scaffold has been developed in Tampere University of Technology. P, PC, PG and PCG scaffolds were prepared in 2004 whereas P(L/D)LA 96/4 scaffolds were manufactured in 2008. The preparation method of P, PC, PG and PCG scaffolds is described in more detail by Sippola [70] and manufacturing method of P(L/D)LA 96/4 scaffolds is described in detail by Mutanen [47]. Preparation methods are partly different resulting in slight differences in physical form and size of scaffolds. Both manufacturing techniques are described briefly in following chapters.

Semiautomatic reeling method

The joint scaffolds (QTY1, Ref JS445 Lot S0002679 Sterile R, P(L/D)LA 96/4 2008) were made at the Institute of Biomaterials (currently part of the Department of Biomedical Engineering), Tampere University of Technology for EU-funded demonstration project “Joint Scaffold”. Preparation started with removing the moisture from P(L/D)LA 96/4 granules using vacuum for two days in nitrogen atmosphere. Then raw material was melt-spun to 4-ply multifilament using a single-screw extruder. Melt-spun polymer fiber consisted of four filaments and went through four ovens and three caterpillars before winding. Melt-spun fibers were knitted into tubular structure using knitting machine (Textilmaschinenfabrik Harry Lucas, Neumünster, Germany). Complete tubular knit was cleaned with ethanol in an ultrasonic washing device, dried first in a fume chamber two hours and then moved into a vacuum over night at room temperature. [47.]

The tubular knit was reeled onto a cylindrical roll using a semiautomatic reeling device and the end of the knitting was attached using ultrasonic welding machine. Views of applied reeling device and knitting are illustrated in Figure 6.2. Reeling machine was fixed to the welding instrument. Scaffolds were shaped using heat treatment in a mould. Mass, diameter and height of the scaffolds were determined to make sure that the quality of fabricated scaffolds was in accordance with defined limit values. All manufactured scaffolds were cleaned in ethanol in an ultrasonic washing device and dried in a fume chamber for two hours and then moved into a vacuum over night at room temperature. Prepared samples were packed separately into double pouches and gamma irradiated for sterility. [47.]

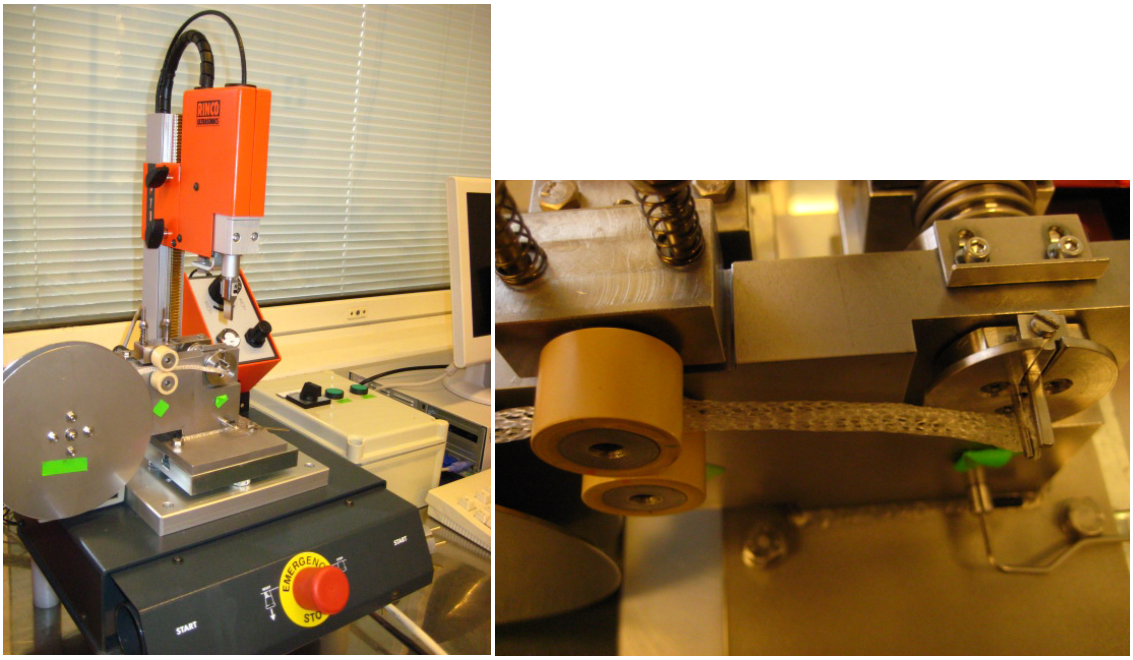

Figure 6.2. *Illustration of semiautomatic reeling device (left) and close-up from attachment mechanism of tubular P(L/D)LA 96/4 knitting for reeling (right).*

Hand-rolled reeling method

Four types of scaffolds were prepared using hand-rolled reeling technique. The melt-spinning and knitting was performed similarly than in semiautomatic reeling method. The most significant differences between these two techniques were related to rolling and attachment of the knit. In addition, the use of chitosan and bioactive glass with P(L/D)LA 96/4 brought little changes in the manufacturing process. [70.]

P type scaffolds were manufactured by rolling 125 mm long P(L/D)LA 96/4 knit to a cylindrical form (Ø = 10 mm) by hand and attached with a polymer glue which consisted of a droplet of P(L/D)LA (70/30) dissolved in acetone. PC type scaffolds were manufactured by dipping prepared P type scaffolds into a 0.5-w/v chitosan liquid and dried for 24 h, and repeated three times. [70.]

Non-woven sheets of bioactive glass were used in PG scaffold preparation. Bioactive glass sheets were formed of melt-spun fibers (stapled after spinning) with a

single glass filament thickness of 15-20 µm. Sheets were sprayed with a 0.25-w/v chitosan solution to fix the structure and improve handling properties. A sheet was put on the P(L/D)LA 96/4 knit and rolled together to form a PG scaffold. Altogether 80 mm of polymeric knit and a glass sheet of 40 mm x 5 mm were used for each scaffold. PCG type scaffold was manufactured by dipping prepared PG scaffolds into chitosan similar to those P type scaffolds. Scaffolds were heat-treated, washed, dried, packed and gamma irradiated. [70.]

6.4. Contrast enhancement

A common challenge in computed tomography imaging of polymeric materials is that they may not possess sufficient X-ray contrast which weakens the image quality. In order to find out if the image quality could be improved, some of the P(L/D)LA 96/4 scaffolds were modified. Two different techniques were performed to improve radio-opacity and they are explained in the following chapters. Both techniques utilized calcium phosphate and hydroxyapatite. Applied materials were chosen for the study because of their ability to absorb X-ray irradiation and thus image contrast are known being better than that of low-density polymeric materials, as it was described in theoretical part in Chapter 3.5.

6.4.1. Biomimetic coating

Simulated body fluid (SBF) is an acellurar solution with an ion concentration similar to that of human extracellular fluids and it was developed by Kokubo *et al.* in 1990 [38]. SBF has been applied to form biomimetic calcium phosphate (CP) and hydroxyapatite (HA) coating on metal, polymer, bioactive glass and composite biomaterials [17; 37; 64]. Polymeric tissue engineering scaffolds have been coated with SBF in several studies [2; 17; 48]. It is reported that the biomimetic layer improves mechanical properties of the polymeric scaffold without affecting its highly interconnected and porous structure. In addition, it has been perceived that homogenously distributed hydroxyapatite coating supports osteoblasts growth and vitality and improves bioactivity, osteoconductivity and osteointegration of the surface. [2.]

In the present study the biomimetic coating was applied to improve radio-opacity of the highly porous P(L/D)LA 96/4 scaffolds. It was also aimed to prepare a coating which would not affect scaffold structure, such as pore sizes and filament thickness, significantly. Prepared SBF solution had ion concentration five times greater than human plasma and it was prepared according to Al-Munajjed [2]. First volumetric flask was half filled with demineralized water and a magnetic stirrer was turned on. Then reagent-grade chemicals were weighed and dissolved into the water. Weighing hoppers were rinsed carefully with demineralized water so that all weighed reagents were flown into the solution. Amount of applied reagents and their mixing order are presented in Table 6.2.

Table 6.2. *Reagents for 5 x SFB. [Modified 2]*

Order	Reagent	Amount
1	Demineralized water	1000.0ml
2	NaCl	40.06g
3	$NaHCO_3$	1.77g
4	KCl	1.13g
5	K_2HPO_4	1.15g
6	$MgCl_2 * 6H_2O$	1.53g
7	$CaCl_2 * 2H_2O$	1.40g
8	Na_2SO_4	0.36g

Chemicals were dissolved for two hours and then pH 7.45 was adjusted with Tris (hydroxymethyl aminomethane) and HCl. Five volumetric flasks (250 ml) were filled with 100 ml of SBF solution and one individual scaffold was immersed in each of the dishes. Volumetric flasks were placed in an incubator at 37°C under constant shaking. The length of the coating period was optimized by immersing the scaffolds in solution for different time periods. Thus it was possible to regulate radio-opacity and thickness of coating layer. Length of coating periods, sample sizes and number of samples are shown in Table 6.3.

Table 6.3. *The sizes of coated scaffolds and the length of the coating periods.*

Coating period [days]	Scaffold diameter [mm]	Parallel samples [pieces]
1	12	1
1	18	1
2	12	1
2	18	1
5	12	1
6	18	1
14	18	1
14	18	5

The simulated body fluid solution was renewed every three days. Finally immersed scaffolds were taken away from SBF solution and placed to dry. In last experiment, five 18 mm scaffolds were coated 14 days, coated scaffolds were put into fume chamber for three days and then into vacuum for one day at room temperature. In all other experiments the drying occurred in a heating chamber at 37°C over night. Dried joint scaffolds were scanned using cone beam computed tomography subsequently. A photographic view and a microscopic image of coated joint scaffold are shown in Figure 6.3.

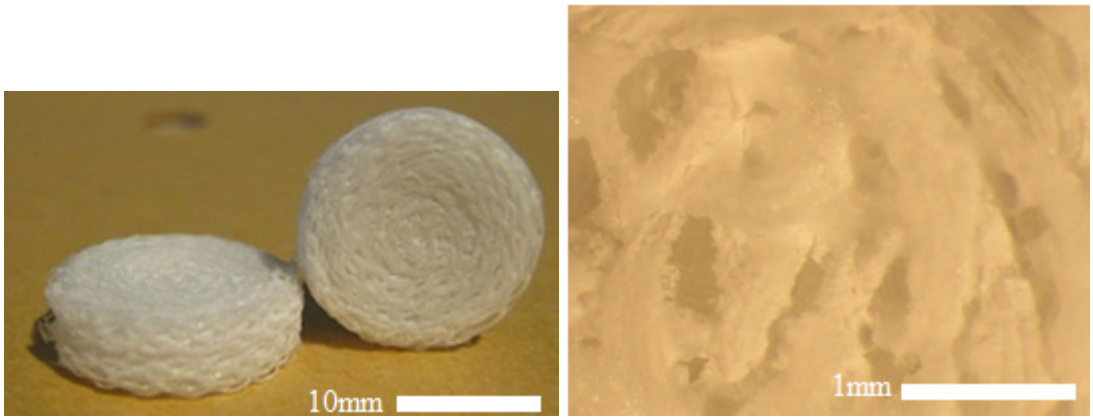

Figure 6.3. *A photographic illustration of SBF coated 18 mm P(L/D)LA 96/4 joint scaffolds (left) and a microscopic image showing a closer view of coated fibers of the scaffold (right). Coating period was 14 days.*

6.4.2. Hydroxyapatite and beta-tricalcium phosphate moulding

Purpose of this experiment was to mould P(L/D)LA 96/4 scaffolds to hydroxyapatite (HA) and beta-tricalcium phosphate (β-TCP) and subsequently scan them using computed tomography. 1.633g of hydroxyapatite (Batch; P81B) and 1.631g of β-tricalcium phosphate (Fluka Chemical Co, 21218, 1kg, 443410/1, 34603122) powder were weighed. Powders were put into separate test tubes of 10 ml and tubes were filled about one third with distilled water. Test tubes were then shaken so that powder and water would mix. It was perceived that HA and β-TCP does not dissolve in the water much and that the formation of the sediment started immediately.

A 12 mm scaffold was immersed into both suspensions. Scaffolds were forced to the bottom of the tubes with a plastic rod. A descending sediment layer kept scaffolds on the bottom of the tubes but to ensure that scaffolds would not rise to the surface, rod was left into tubes. An ultrasonic washing device (Vibra Clean VC, Vibraclean Oy, Lahti, Finland) was used to force powder to distribute into the scaffold structure evenly. After eight minutes of ultrasonic washing, additional water was sucked away with syringe and tubes were put into fume chamber so that water and moisture would evaporate away. Moulded scaffolds were left into the test tubes but were taken away during the computed tomography imaging.

6.5. Mass and dimension determination

Mass of the P(L/D)LA 96/4 joint scaffolds (n = 35) were measured using analytical balance (Mettler AG245 Toledo, accuracy 0.0001g). The height and diameter of the scaffolds were measured using the slide gauge. The 18 mm scaffolds (n = 5) were also measured after SBF coating. Irregular structure of the scaffolds and softness of material made dimension determination difficult to perform. Thus dimensions were determined as an average of three measurements to enhance their reliability.

The main purpose of performed measurements was to analyse the correlation between porosity degree, mass and volume of the scaffold. Scaffold volume was estimated using the equation for cylindrical object, $V = A * h$, where A and h describe circular area of scaffold bottom (A) and height of scaffold (h), respectively. The results are presented and interpreted in Chapter 8.7.

Also the possible change in mass and dimensions due to SBF coating was studied. The results are presented in Chapter 7.6. and interpreted in Chapter 8.6.

6.6. Structural characterization using Planmeca ProMax 3Ds

This chapter covers the structural characterization of joint scaffolds using cone-beam computed tomography (CBCT) and computerized image analysis process. The main purpose was to find out the suitability of the Planmeca ProMax 3Ds for joint scaffold characterization. Operational principle of computed tomography is described in theoretical part in Chapter 3.2. Theoretical background for image-based characterization is described in Chapter 3.4. and definitions for structural characteristics are given in Chapter 2.

6.6.1. Assembly

A cone-beam computed tomography (ProMax 3D s, Planmeca, Helsinki, Finland) was used to characterize the structure of joint scaffolds. The photographic view of the device is shown in Figure 6.4. The imaging assembly consisted of three main parts; CBCT device, 3D Reconstruction Server and Image Acquisition Work Station. The device was connected to 3D Reconstruction Server where the images were automatically recorded after scanning. The Image Acquisition Work Station was a computer used to view and analyze images in two and three dimensions immediately after scanning. The device was located in the Tampere University of Technology at the Department of Biomedical Engineering.

For image acquisition, the sample was put on the sample holder and the exposure parameters were adjusted from control panel. The measuring field of the device was a cylindrical volume and the size of it could be varied using preprogrammed target sites. The volume height was set to *lower* and patient size to *young adult*. Thus only the lower half of the maximum measuring field volume was exposed. The use of that smaller target volume was required in order to apply *high resolution mode*. *High resolution mode* was selected from the control panel and it was used in each scan in order to get more accurate images. The voxel size was 100 µm at *high resolution mode*. Exposed cylindrical volume had a diameter of 50 mm and height of 50 mm. Jaw size was selected to *average*, side to *left* and target area to *incisor*. The *3D standard exposure* program was applied.

Previously described adjustments were kept constant during the whole study. Exposure voltage and current seemed to have the biggest impact on image quality and

therefore they were the main variable parameters during scanning. Anode voltage and current could be varied in the range of 54-84 kV and 1-16 mA, respectively, and were adjusted from control panel. Filtering assembly consisted of a constant copper sheet (3 mm) and variable aluminium sheets (0-45 mm). A 5 mm and four 10 mm thick aluminium sheets were possible to regulate by hand. More exact technical specifications of Planmeca ProMax 3Ds can be found from Appendix 1.

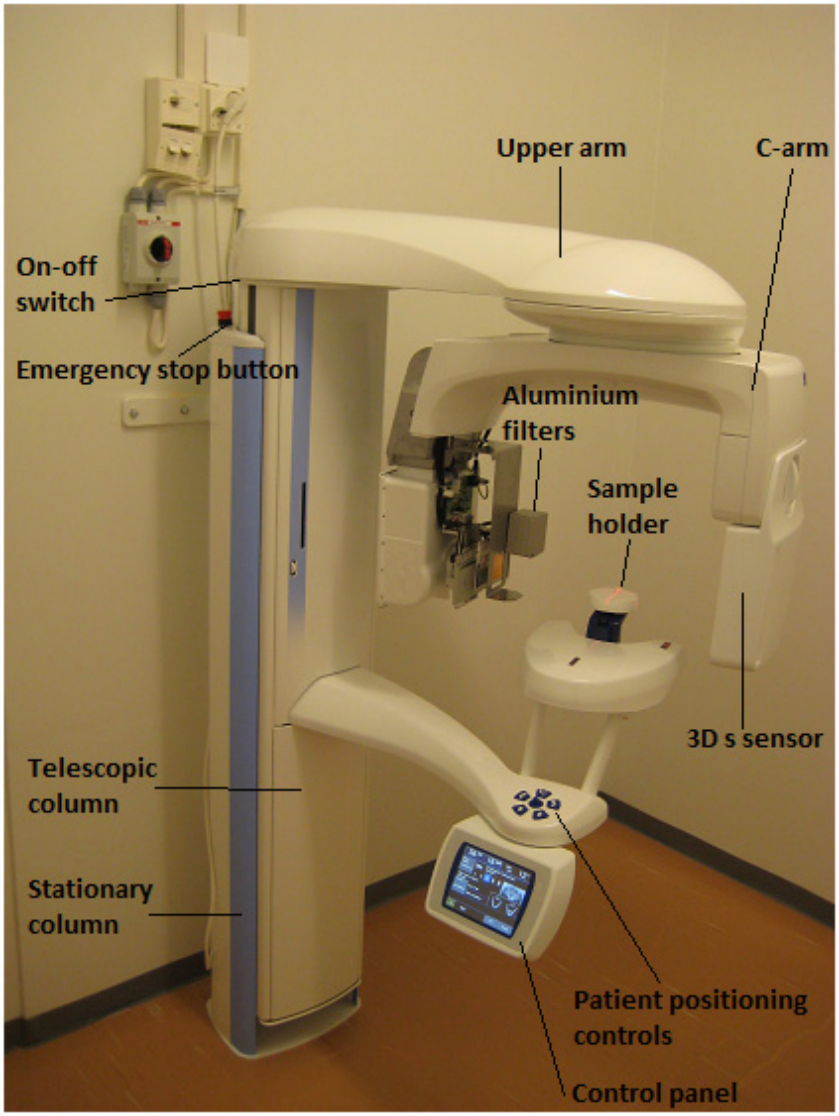

Figure 6.4. *Planmeca ProMax 3D s*

6.6.2. Imaging

First P(L/D)LA 96/4 scaffolds were scanned with and without contrast enhancement. Contrast enhancement processes by coating and moulding was described in Chapter 6.4. In addition some of the P(L/D)LA 96/4 scaffolds were scanned immersed in liquids and slurries in order to improve the image quality. Different combinations for anode voltage and current were experimented in order to optimize the imaging parameters and image quality. The aim was also to find out if the image quality could be improved using

contrast enhancement techniques. Table 6.4. summarizes all performed P(L/D)LA 96/4 scaffold characterization approaches using cone-beam computed tomography. Hand-rolled scaffolds (P, PC, PG and PCG) were taken into this study afterwards and thus contrast enhancement or imaging parameter optimization were not performed for these scaffolds. Scanning processes are described in following paragraphs.

Table 6.4. *Performed Planmeca ProMax 3Ds imaging approaches for joint scaffold structural characterization.*

Scaffold type	Contrast enhancement	Scaffold size [mm]
P(L/D)LA 96/4	no	8 10 12 14 18 20
P	no	10
PC	no	10
PG	no	10
PCG	no	10
P(L/D)LA 96/4	SBF coating	12 18
P(L/D)LA 96/4	HA molded scaffold	12
P(L/D)LA 96/4	β-TCP molded scaffold	12
P(L/D)LA 96/4	Iodine solution	8 14
P(L/D)LA 96/4	HA slurry	12 18
P(L/D)LA 96/4	β-TCP slurry	12 18
P(L/D)LA 96/4	BaSO4 slurry	12 18
P(L/D)LA 96/4	SBF solution	12 18
P(L/D)LA 96/4	Water	12 18

Imaging in air

This approach include scanning of plain P(L/D)LA 96/4 and hand-rolled scaffolds in air without contrast enhancement and also imaging of SBF coated and HA and β-TCP moulded P(L/D)LA 96/4 scaffolds. Scanning was very easy to perform as the samples were simply put onto cleaned sample holder and desired imaging parameters were selected from the touch screen of the device. HA and β-TCP moulded joint scaffolds were scanned at the same time so that the image quality could be better compared afterwards.

Imaging immersed in liquids and slurries

P(L/D)LA 96/4 joint scaffolds were immersed in commercially available iodine contrast medium, water, SBF solution and prepared radio-opaque slurries and then CT scanned. Immersion studies were tried in order to get the structure of the scaffold to be distinguished better from the background of obtained images. The experiments were based on the assumption that the ability of polymer to absorb X-ray irradiation could be

too close to the absorbing ability of air which may cause the unclarity of the images. It was supposed, that the contrast differences would be bigger if solution which absorbs the radiation considerably more than the polymer is used instead of air. Because polymeric scaffold has much lower radio-opacity than prepared suspensions, the scaffold structure would be seen as an empty region in images. Inspection of acquired images required inverting the threshold, so that the polymeric structure could be visualized.

Pure water and an iodine contrast agent solution ($Omnipaque^{TM}$, 180 mg iodine/ml, IOHEXOL, batch 10744137) were as such used. Instead, slurries of hydroxyapatite (HA), beta-tricalcium phosphate (β-TCP), barium sulphate ($BaSO_4$) and simulated body fluid (SBF) solution needed to prepare in the laboratory. These materials were tried for two reasons, some of them were chosen because they are generally clinically used radio contrast agents (barium and iodine) and rest of them were tried because their radio-opacity was supposed to be higher than P(L/D)LA 96/4 has. In Figure 6.5. three different sample arrangement types for imaging are illustrated. P(L/D)LA 96/4 scaffold was immersed into the iodine solution and barium sulphate slurry (right picture) for CBCT imaging and a plain scaffold was scanned without contrast enhancement by putting it on a sample holder (left picture).

Figure 6.5. *Illustration of three different imaging approaches. P(L/D)LA 96/4 scaffold was scanned in air without any contrast enhancement by putting it on a sample holder (left). Scaffolds were also scanned immersed in transparent iodine solution (left tube) and slurry of barium sulphate and water (right tube). In right tube scaffold lays on the bottom under the precipitation of* $BaSO_4$.

Three different concentrations of water soluble and transparent iodine contrast agent solution were experimented. First the unmixed contrast medium was applied by injecting 2.0 ml of iodine solution into a plastic dish. Two lower concentration solutions were prepared afterwards of water and iodine solution. First of them consist of 1.5 ml iodine solution and 1.5 ml water and other of 1.5 ml of iodine solution and 3.0 ml of water. A 14 mm P(L/D)LA 96/4 scaffold was immersed in contrast medium. Dish was strongly shaken until the solution had penetrated into the sample structure completely which took about 3-5 minutes. In spite of shaking, there were observed several tiny air bubble-looking spots in scaffold structure. Therefore scaffold was pressed lightly with plastic tube to remove them before imaging.

The slurries were prepared by putting 2±0.5 g of HA, β-TCP and $BaSO_4$ powders into separate cylindrical dishes and then dishes were filled with water. Used powders did not dissolve into water very much and precipitate was formed to the bottom of the dish in couple of minutes. Each slurry was poured into a separate plastic or glassy cylindrical dish of 10 ml and a gamma irradiated joint scaffold was immersed in solution. The slurries did not penetrate into the structure easily and thus the dishes needed to be shaken heavily for couple of minutes. The dishes, in which the scaffold was immersed, were put on the sample holder of Planmeca CBCT and scanned after the scaffold was settled on the bottom of the dish. The imaging was first tried to perform before sediment sheared to descend. The imaging was also tried to perform after the sediment layer was descended on the bottom of the dish. It succeeded by pressing the scaffold with plastic tube to the bottom of the dish. Scaffolds were also scanned immersed in SBF solution which was prepared for scaffold coating (described in Chapter 6.4.1.).

6.6.3. Image quality evaluation

The quality of each obtained image from different imaging approaches was visually evaluated and compared in order to conclude which imaging approach produced best image quality and which are the optimal imaging parameters. Structural parameters were aimed to be determined using only visually best image data.

Image quality evaluation was performed immediately after scanning using The Planmeca Romexis 3D Explorer, ImageJ (ImageJ 1.43v, National Institutes of Health, USA) and Slicer 3D software. The image quality evaluation was based on the comparison of 2D images in axial, coronal and sagittal views using Planmeca software. Slicer 3D and ImageJ were used to view inverted images of moulded scaffolds and scaffolds scanned immersed in radio-opaque solutions. The image contrasts and brightness were adjusted in order to get best visual view. In quality evaluation, attention was paid most to the contrast and accuracy of images.

Four types of hand-rolled scaffold (P, PC, PG and PCG) were intended to be characterized without image quality evaluation. The quality evaluation was not made because it was supposed that the image quality would be similar than for P(L/D)LA 96/4 scaffolds because they consist mainly of same material. More extensive analysis of the success of different Planmeca ProMax 3Ds imaging approaches is described in Chapter 7.1.

6.6.4. Image analysis of P(L/D)LA 96/4 joint scaffolds

ImageJ program was applied to determine numerical values for porosity degree using obtained Planmeca ProMax 3Ds image data. ImageJ was chosen for analysis because it is free and available program. Pore analysis of the scaffolds was performed using Pore Analyzer program which was developed during Tekes funded MIKAMA project. Each

phase from pre-processing of images to calculations is described in this chapter in detail.

Porosity degree determination

Image data was obtained from the CBCT system and reconstructed automatically into 2D image sets. REC formed image sets were opened using ImageJ program with given parameters in Table 6.5. With these parameters the output format for each sample was a set of 501 quadratic 521 x 521 bitmap images with a pixel size of 100 µm.

Table 6.5. *Opening parameters for Planmeca ProMax 3Ds image*

Parameter	Selection
Image type	16-bit unsigned
Width	521
Height	521
Offset to first image	0
Number of images	501
Gap between images	0

Desired measurements were chosen from the set measurements dialog box. *Area, Area fraction* and *Limit to threshold* were checked. In that case *Area* described the amount of non-zero regions in selection in square pixels. *Area fraction* gave the percentage value of how much non-zero pixels are in relation to the total amount of pixels in selection. Because *Limit to threshold* was checked only thresholded pixels were included in calculations. [21.]

Left picture in Figure 6.6. illustrates obtained cross-sectional 2D CBCT image of P(L/D)LA 96/4 scaffold before exact thresholding. Right image is a cross-sectional 2D SEM image of the scaffold which was applied to adjust threshold levels.

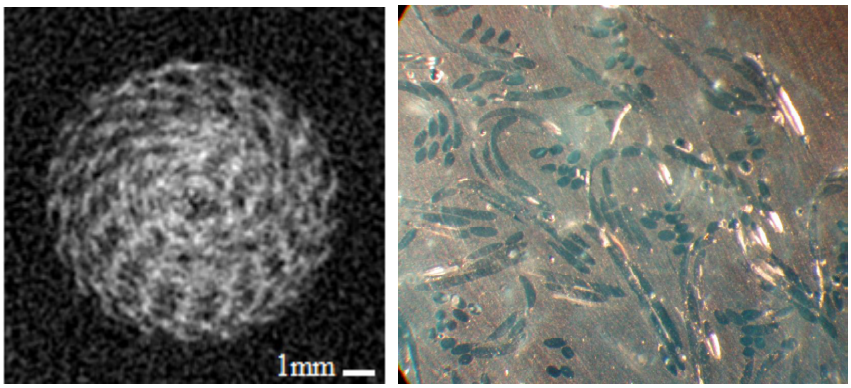

Figure 6.6. *Left image represents a Planmeca ProMax 2D image from the cross-section of 10mm P(L/D)LA 96/4 joint scaffold without exact thresholding. The right image is the 2D SEM image from the cross-section of PCG scaffold taken by Sippola. The black regions in SEM image represent the P(L/D)LA phase and bright parts on some of the fibres represent chitosan phase. The bioactive glass phase can be seen as whitish regions. [70.]*

Thresholding was used to segment obtained gray scale images into regions of interest and background. Images were thresholded using both manually adjusted levels and automatic (local and global) thresholding methods.

Each automatic thresholding method (16 global and 6 local methods) in the ImageJ was tried to be adapted to the acquired images. The background theory of each threshold method is described in detail on Fiji's Auto Threshold website, but in this work only their functionality to scaffold images are described. [21.] The evaluation of the suitability of applied automatic techniques was required and it included both a visual assessment of the thresholded images and the comparison of calculated porosity values. Both the visual assessment and the calculated porosity values should correspond so that the threshold method could be considered correct. First thresholded representative slice images of joint scaffolds were compared visually with SEM image (Fig. 6.6.) and microscopic view (Fig. 6.1.) of the scaffold. The visual assessment of the automatic thresholding methods was performed using *Try all* tool which created a montage of all the local (Fig. 6.7.) and global methods (Fig. 6.8.). These images allowed exploring how the different image analysis algorithms performed on a particular scaffold image.

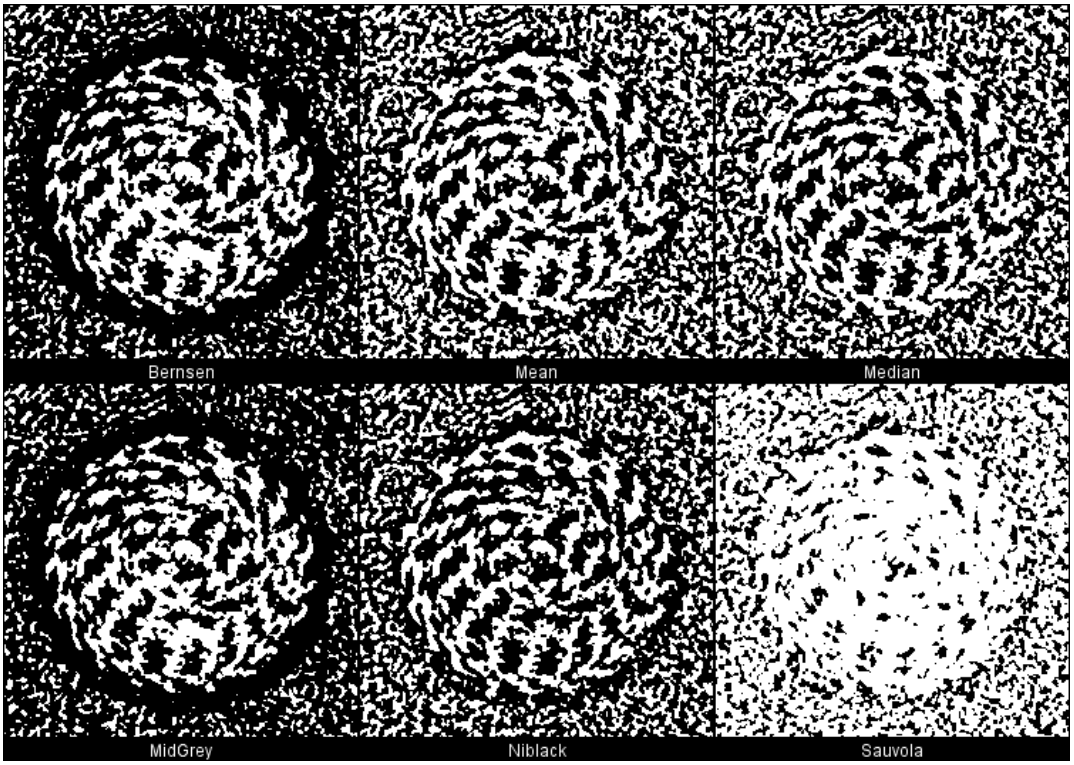

Figure 6.7. *A montage of six local threshold methods*

Applying of local automatic methods was allowed only for 8-bit images so the original 16-bit images needed to be converted into 8-bit form before thresholding. Five visually most suitable thresholding methods were intend to be chosen and porosity degree was aimed to be calculated using only images which were thresholded using chosen techniques. The second phase of suitability evaluation was that obtained image-based

calculated values were compared with the gravimetrically calculated values and it is described in Chapters 7.2. and 8.2.

Three different manually adjusted levels were also applied and they were set based on visual assessment. Images were compared with microscopic view of the scaffold during the adjustment. Threshold levels were manually adjusted using *over/under* threshold mode and *default* threshold method. Lower threshold level was set to have constant values of 192, 265 and 300 and upper threshold level was set to always have its maximum value. *Over/under* mode displays pixels below the lower threshold value in blue, pixels above the upper threshold value in green and thresholded pixels in grayscale (Figure 6.9. left). *Default* method is the original method of auto thresholding available in ImageJ, which is a variation of the IsoData algorithm. [21.]

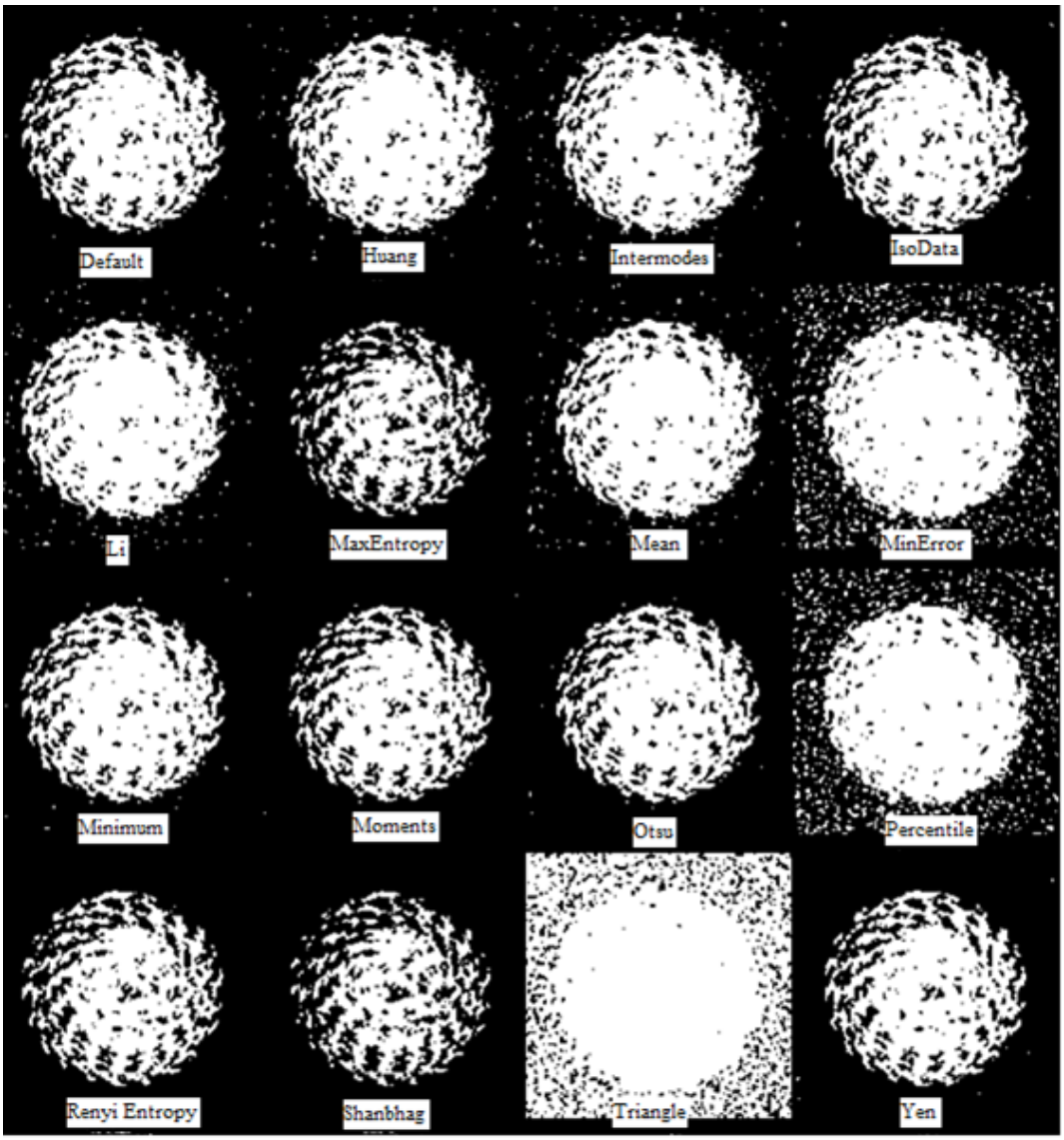

Figure 6.8. *A montage of 16 global threshold methods.*

The volume of the sample needed to be separated from the measuring field of the CBCT before calculations. Volume of interest (VOI) was selected manually based on visual assessment and was performed separately for each image set. VOI selection consisted of

two parts. First the extra empty space was cut in vertical direction. That meant in practice that extra 2D images were removed from the image set using *Duplicate* command. Only those slices in which the scaffold was totally visible were remained.

After the desired images were separated from the image set, the extra empty space was removed in horizontal direction and in practice that was done by cropping each remaining slice image. Due to the cylindrical shape of the samples, images were cropped using *elliptical selection* -tool. The diameter of circle-shaped selection was set as 90 % of the nominal diameter of the scaffold which ensured that empty space was not included in the selection. Applied sizes of area selections for porosity determination are summarized in Table 6.6. The image cropping using *elliptical selection* tool is illustrated in left image in Figure 6.9. The meaning of horizontal and vertical direction is illustrated right picture in Figure 6.9.

Table 6.6. *Sizes of applied area selections.*

Diameter of scaffold scaffold [mm]	Diameter of selection [pxl]	Number of slices [pieces]	Pixel size [µm]	Physical volume [mm³]
8	72	22-30	100	89.6 - 122.1
10	90	21-29	100	133.6 - 184.5
12	108	24-30	100	219.9 - 274.8
14	126	25-31	100	311.7 - 386.5
18	162	30-33	100	618.4 - 680.2
20	180	29-39	100	738.0 - 992.4

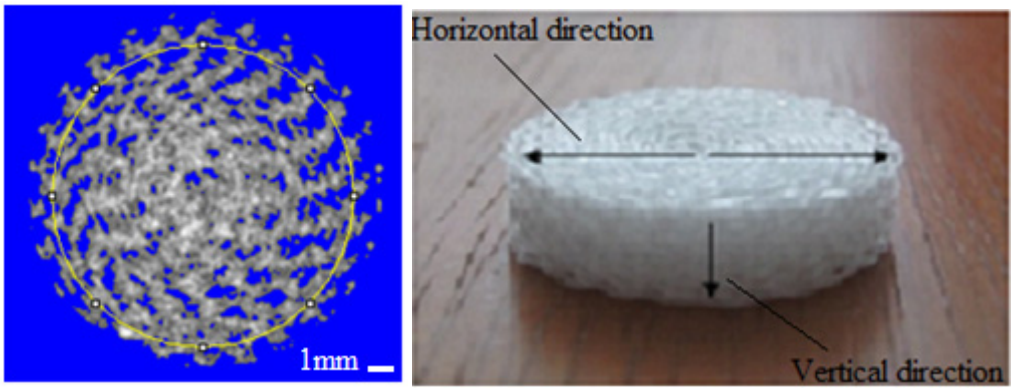

Figure 6.9. *Left picture is a representative CBCT slice image of P(L/D)LA 96/4 joint scaffold which is selected using elliptical selection tool and thresholded using manually adjusted levels of 192-max. The right picture illustrates the purposes of horizontal and vertical directions in area selection.*

Same sized circular selections were used for parallel samples so that the calculated porosity degree values could be better compared. However, the analyzed volume was not absolutely the same on all the parallel samples because the number of analyzed 2D slice images was not constant because of the different physical sizes of the samples. Therefore the number of the remaining images varied in every image set.

Porosity degree of the entire scaffold was determined by first counting the amount of non-zero pixels from each remaining 2D image using *Analyze particles* command. The command measured all the circular regions on all remaining images automatically and created a results table with either one row per image. Then the total amount of pixels in circular selection in single 2D slice was counted using *Measure* command. [21.]

The result table was opened and an average of non-zero pixels in all remaining 2D images was calculated using spreadsheet. Porosity degree was calculated as relation of empty region with the total region using equation (4):

$$Porosity\ (\%) = \left(\frac{A_T - A_S}{A_T}\right) * 100\% \qquad (4)$$

where A_T and A_s describes the total amount of pixels in circle area, average amount of non-zero pixels in circle area, respectively. Parameter A_T can also be calculated manually using geometric equation of circle πr^2 where r describes the radius of circle in pixels.

Porosity distribution determination in horizontal direction

Porosity degree in different sections of the scaffold was determined in order to find out if the porosity varies in scaffold structure. Porosity distribution was determined both in vertical and in horizontal direction as described in Figure 6.9. The determination was performed similarly as in previous chapter except volume selection and thresholding. The total volume of the scaffold for each sample was kept same than in porosity determination but it was divided into smaller segments (either vertical or in the horizontal direction) and the porosity of each segment was calculated separately.

The area selection of remaining images and calculations were done using *ROI Manager* –tool which enables selecting and calculating of several different segments at the same time. First, the area of each remaining image was divided into three percentually equal parts as illustrated in Figure 6.10. The diameter of the largest selection was 90 % of the nominal diameter of the scaffold.

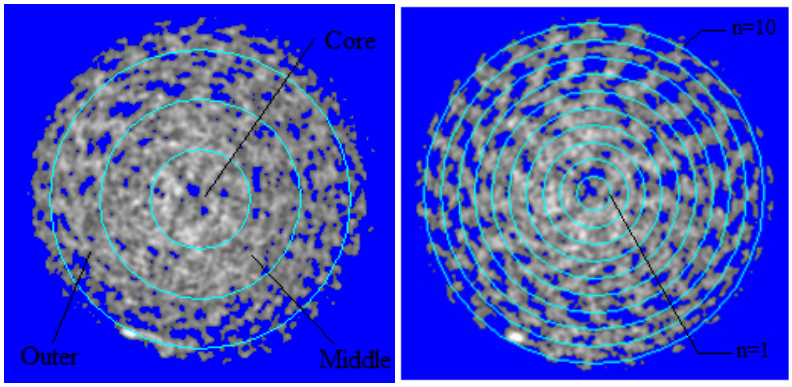

Figure 6.10. *Multiselected CBCT 2D images of P(L/D)LA 96/4 joint scaffold. Sample is imagined from above and the achieved data is divided into three segments (left) and ten segments (right).*

Applied area selection values are presented in Table 6.7. One must notice that the largest circular area was same size than the selection used when porosity of entire scaffold was determined.

One local automatic threshold method and two manually adjusted levels were applied to Planmeca CBCT image data. Manually adjusted levels were set using *over/under* threshold mode and *default* threshold method. Lower threshold level was set to have constant values of 192 and 300 and upper threshold level was set to always have its maximum value. *Niblack* was also applied because it was best performing automatic method in previous measurements.

Table 6.7. *Applied area selection parameters in horizontal porosity distribution determination.*

Diameter of scaffold [mm]	Core [pxl]	Middle [pxl]	Outer [pxl]
8	24	48	72
10	30	60	90
12	36	72	90
14	42	84	126
18	54	108	162
20	60	120	180

The porosity distribution was also determined using larger amount smaller segments as illustrated in the right picture in Figure 6.10. The number of segments was chosen according to size of the scaffold so that the amount would be reasonable in proportion to the diameter of the scaffold. The images of the smaller scaffolds (d = 8, 10 and 12 mm) were divided into smaller segments than the bigger scaffolds (d = 14, 18 and 20 mm). Smallest circle had a diameter of either 15 or 20 pixels depending of scaffold size and diameter was always the same amount enlarged (15 or 20 pixels). The sizes and number of the circular selections were kept constant between parallel samples. Used area selection parameters are shown in Table 6.8.

Table 6.8. *Area selection parameters in horizontal porosity distribution determination.*

Diameter of scaffold [mm]	Smallest circle [pixel, (mm)]	Enlargement of diameter of the circle [pixel]	Number of circles [pieces]
8	15, (1.5)	15	5
10	15, (1.5)	15	6
12	15, (1.5)	15	8
14	20, (2.0)	20	7
18	20, (2.0)	20	9
20	20, (2.0)	20	10

Multi measure –tool from *ROI Manager* dialog box was utilized when porosity degree in different sections was calculated. ImageJ enabled to calculate the non-zero pixel

number of every circular selection but the non-zero pixel amount of each narrow segment needed to be calculated separately using spreadsheet. The share of the empty region (porosity) of the each segment was calculated with the equation (5).

$$Porosity\ (\%) = \left(1 - \frac{(A_n - A_{n-1})}{(M_n - M_{n-1})}\right) * 100\% \qquad (5)$$

where, A_n, M_n and n describes amount of non-zero pixels in circle area n (A_n), total amount of pixels in area n (M_n) and ordinal number of circle (n), respectively. The values that have been used in the equation (5) are averages that have been calculated of remaining slices.

Porosity distribution determination in vertical direction

Images were thresholded using *over/under* threshold mode and *default* threshold method. Lower threshold level was set to have a constant value of 300 and upper threshold level was set to always have its maximum value. The measured volume was selected similarly as in the porosity determination as illustrated in left picture in Figure 6.9. The sizes of applied circular selections are presented in Outer chart in Table 6.7. Porosity distribution determination in vertical direction based on that the porosity of each slice was calculated separately.

Distribution was also calculated so that measured volume was divided vertically to three separate volumes and the porosity was calculated from each section. One volume consisted of 10 circular selected 2D images. Calculation of zero pixels was performed using ImageJ *Analyse particles* –command and the porosity distribution was calculated using obtained image data in spreadsheet.

Pore analysis

Pore analysis was performed on P(L/D)LA 96/4 scaffold image data using Pore Analyzer program. Six scaffold sizes were analyzed using three parallel samples. Pore analysis is based on that the software fits different sized spherical volumes into the empty space of sample structure and calculates the total volume for different sphere sizes.

Threshold levels and volume selection were set prior analysis using ImageJ. Pore Analyzer operates only if the images are quadratic selected. First sequential 2D image sets were cropped using *duplicate* command. Remaining slices were selected from the center of each sample using *rectangular selection* tool. The sizes of the applied quadratic selections varied according to the size of the scaffold and the used parameters are shown in Table 6.9. Images were thresholded using local automatic method *Niblack* because the method performed better than other applied automatic methods in previous porosity calculations.

Total volume of three different sizes of spherical volumes was intended to be determined using the results file and bar graph produced by Pore Analyzer program.

The aim was to determine the total volume of pores with diameters of 100 µm, 200 µm and 300 µm because these sizes are in range of generally recommended scaffold pore sizes as described in Chapter 2. The average values for fitted sphere volumes are calculated using spreadsheet and results are reported as a percentual share of total analyzed volume. Determined representative bar graft of 12 mm P(L/D)LA 96/4 joint scaffold is attached to the Appendix 3.

Table 6.9. *Pore analysis parameters for P(L/D)LA 96/4 joint scaffold images.*

Diameter of scaffold [mm]	Number of samples [pieces]	Rectangular selection [pxl]	Number of slices [pieces]	Physical volume [mm³]
8	3	50 x 50	28 - 30	72.5
10	3	65 x 65	30 - 38	150.0
12	3	80 x 80	32 - 35	214.4
14	3	90 x 90	33 - 36	279.5
18	3	120 x 120	39 - 40	568.8
20	3	140 x 140	36 - 42	705.6

6.6.5. Image analysis of hand-rolled scaffolds

Porosity degree of P, PC, PG and PCG type scaffolds was calculated and the glass content of PG and PCG scaffolds was determined. The principle of image analysis was similar than for P(L/D)LA 96/4 scaffold images described in Chapter 6.6.4. but the image analysis parameters were partly different.

Porosity degree

The applied parameters for porosity determination are presented in Table 6.10. Porosity was determined using *Niblack* method and manually set levels of 300. Manual levels were set using *B&W* threshold mode and *default* threshold method. The *B&W* mode displays features in black and background in white [21]. The number of applied 2D images varied according to physical size of the sample. The determination was performed using 65-74 circularly cropped two-dimensional sequential images.

Table 6.10. *Parameters for porosity degree determination.*

Diameter of selection [pxl]	Number of slices	Threshold level	Pixel size [µm]	Physical volume [mm³]
90	65 - 74	300, Niblack	100	413.5 - 470.8

Glass content

Applied parameters for glass content determination are presented in Table 6.11. A constant volume of 260.8 mm³ was selected for analysis for each sample. A constant threshold level of 450 was applied and adjustment based on visual assessment.

Table 6.11. *Parameters for glass content determination.*

Diameter of selection [pxl]	Number of slices	Threshold level	Pixel size [µm]	Physical volume [mm³]
90	41	450	100	260.8

The Planmeca CBCT images were cropped for image analysis using *elliptical selection* tool and by using it, a cylinder-shaped volume was selected. The yellow circle in left picture in Figure 6.11. illustrates the applied area selection and it had a diameter of 90 pixels. The glass content was determined by thresholding the images so that only the glass phase was remained visible as illustrated in right picture in Figure 6.11. Then the non-zero pixels were calculated using *Analyze particles* command similar than in Chapter 6.6.4. in porosity calculations.

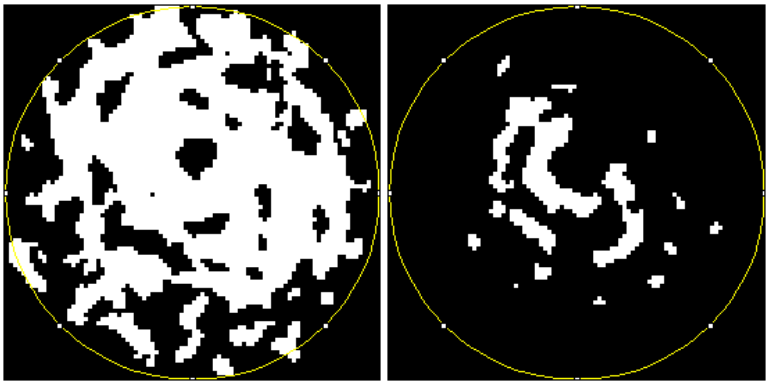

Figure 6.11. *Representative 2D images of PG type scaffold using Planmeca ProMax 3Ds. The left image is thresholded using level of 300 and right image using level of 450. White regions in left image describe the polymer and glass phases. Polymer phase is thresholded invisible from right image and only glass phase can be distinguished. The size of the selection (yellow circle) is 90 pixels which correspond to physical size of 9 mm.*

6.7. Structural characterization using Skyscan-1072

This chapter covers the imaging and structural characterization of joint scaffolds using high resolution micro-computed tomography (µCT). The main purpose of this study was to achieve comparative results for structural parameters which could be used to assess the reliability of performed Planmeca ProMax 3Ds characterization.

6.7.1. Assembly and imaging

Five different types of scaffolds were scanned using a SkyScan-1072 desktop fan-beam micro-CT (SkyScan, Aartselaar, Belgium). The imaging was performed by co-workers of MIKAMA project in University of Turku and the image data was analyzed afterwards in Tampere University of Technology.

Each sample was scanned using constant imaging parameters of 50 kV and 197 µA. The raw image data was manually reconstructed to 8-bit form using SkyScan NRecon

version 1.6.3 software. The output format for each sample was a set of 1024 x 1024 bitmap images. The imaging resolution varied according to the physical size of the sample. The image pixel size was approximately 8.4 µm for 8 mm scaffolds and 11.1 µm for hand-rolled scaffolds. The studied scaffold types, amounts and achieved image pixel size are presented in Table 6.12.

Table 6.12. Type and number of scanned scaffolds

Scaffold type	Diameter [mm]	Number of samples	Pixel size [µm]
P(L/D)LA 96/4	8	4	8.370
P	10	2	11.135
PC	10	2	11.135
PG	10	2	11.135
PCG	10	2	11.135

6.7.2. Image analysis

Achieved image data was applied for porosity degree determination of each scanned sample and the glass content of PCG and PG type scaffolds was also calculated. Also volumetric pore size distribution was determined from six samples.

Porosity degree

Porosity of scaffolds was determined using 2D image sets. The image data was analyzed similarly as the Planmeca ProMax 3Ds image data, described in Chapter 6.6.4. The image analysis was performed using ImageJ and received values were summed up using spreadsheet. Slices of 8 mm scaffolds were tried to crop so that the size of the circular selection would be physically equal to the size used in Planmeca ProMax study. However, analyzed physical volume was still not exactly the same compared to Planmeca CBCT study because there were not relevant images enough. Image analysis parameters for porosity determination are summarized in Table 6.13.

Table 6.13. *Applied image analysis parameters for porosity degree determination*

Scaffold type	Number of samples [pieces]	Diameter of selection [pxl]	Number of slices [pieces]	Threshold level	Physical volume [mm³]
P(L/D)LA 96/4	4	860	264 - 330	50	89.9 - 112.3
P	2	720	500	50	276.5
PC	2	720	500	50	276.5
PG	2	720	500	10	276.5
PCG	2	720	500	15	276.5

A cylinder-shaped volume from the core of each hand-rolled scaffold (P, PC, PG and PCG) was selected for analysis as 500 slice images and circular selection with a

diameter of 720 pixels was applied. Slice sets were cropped using *elliptical selection* tool. The applied circular selection is illustrated in right picture in Figure 6.12. as a thresholded 2D image of P type scaffold is selected (yellow circle). White regions in the image represent polymer phase and black regions empty space.

Each cylindrical-shaped image set was thresholded using manual selection of threshold levels and they were set based on visual assessment. Threshold levels were adjusted using *B&W* threshold mode and *default* threshold method. Scaffolds which consisted of only polymers were thresholded using constant level of 50. Scaffold which contained glass needed different threshold levels. PG scaffolds were thresholded using level of 10 and PCG samples using threshold level of 15. *Analyze particles* command was used to calculate the amount of zero pixels from each slide and result tables were saved. The porosity was calculated using the received result table with a spreadsheet.

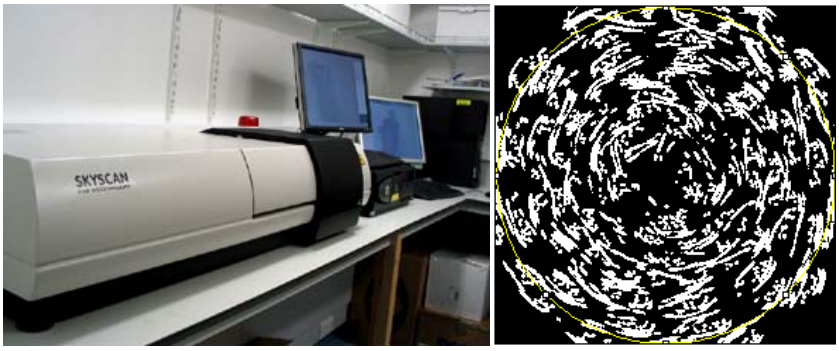

Figure 6.12. *SkyScan 1072 desktop micro-CT (left) [74] and representative 2D image of P type joint scaffold using manually set threshold levels of 50 (right).*

Glass content

Glass content of PG and PCG scaffolds was determined using same cylindrical-shaped volumes than in the porosity determination. The glass content determination was based on that the radio-opacity of glass phase and polymer phase is different. The threshold levels were adjusted visually so that glass phase remained visible but polymer phases became invisible as illustrated in Figure 6.13.

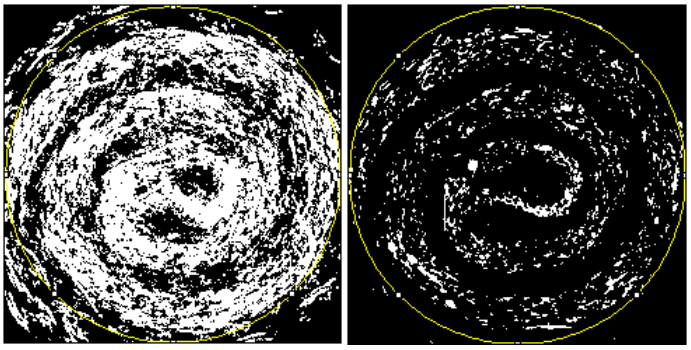

Figure 6.13. *Representative 2D images of glass containing PG scaffold. The left image is thresholded using level of 10 and right image has a threshold level of 40. The glass and polymer phases are visible in left image but the polymer phase is thresholded invisible in right image.*

The glass content was calculated using two different threshold levels, 40 and 50, because it was challenging to notice the exact threshold level visually where the polymer phase disappeared. The amount of zero pixels from each slice was calculated using *Analyze particles* command and result tables were saved as a spreadsheet form for the calculation of the glass content.

Pore analysis

Prior analysis the reconstructed image data was cropped to quadratic shape using *rectangular selection* tool in ImageJ and the analysis was performed using the Pore Analyzer software similarly than in Planmeca ProMax study described in Chapter 6.6.4. Analysis was first tried to perform using the quadratic volume of about 600 x 600 x 340 and then 600 x 600 x 256 pixels but our hardware facilities was not sufficient to do that and image sets needed to resize smaller. Finally, the sufficient volume for analysis was 400 x 400 x 256. Volume size of 600 x 600 x 256 could be applied for one 8 mm P(L/D)LA 96/4 sample and rest samples were analyzed using volume size of 400 x 400 x 256. Applied parameters in pore analysis are summarized in Table 6.14.

Table 6.14. *Applied pore analysis parameters*

Scaffold type	Number of samples [pieces]	Rectangular selection [pxl]	Number of slices [pieces]	Threshold level	Physical volume [mm³]
P(L/D)LA 96/4	2	600 x 600	256	50	54.1
		400 x 400	256	50	24.0
P	1	400 x 400	256	50	56.6
PC	1	400 x 400	256	50	56.6
PG	1	400 x 400	256	10	56.6
PCG	1	400 x 400	256	15	56.6

7. RESULTS

Cone beam computed tomography (Planmeca ProMax 3Ds) and high resolution micro-computed tomography (SkyScan 1072) were used to characterize joint scaffold structures. The results from visual evaluation of image quality are described in Chapter 7.1. The calculated values for porosity degree, porosity distribution, pore volume distribution and glass content are presented in Chapters 7.2 - 7.5. The effects of SBF coating to scaffold mass, diameter and height are described in Chapter 7.6.

7.1. Evaluation of Planmeca ProMax 3Ds image quality

The obtained CT images without using any contrast enhancement and images of SBF coated scaffolds were chosen for structural analysis because they produced the best image quality. The optimized scanning parameters and number of samples for structural characterization are presented in Table 7.1. The advantages and drawbacks of each performed CBCT imaging approach are discussed in detail in following chapters.

***Table** 7.1. Chosen scaffold types for structural characterization using Planmeca ProMax*

Scaffold type	Size [mm]	Samples [pieces]	Voltage [kV]	Current [mA]
P(L/D)LA 96/4	8	6	62	13
P(L/D)LA 96/4	10	6	62	13
P(L/D)LA 96/4	12	6	62	13
P(L/D)LA 96/4	14	6	62	13
P(L/D)LA 96/4	18	5	62	13
P(L/D)LA 96/4	20	6	62	13
P	10	3	62	13
PC	10	3	62	13
PG	10	3	62	13
PCG	10	3	62	13
14 days SBF coated P(L/D)LA 96/4	18	5	60	13

7.1.1. P(L/D)LA 96/4 scaffolds without contrast enhancement

Scanning and image reconstruction took less than four minutes on average so acquisition of the 2- and 3-dimensional views of the scaffold was very fast. In Figure

7.1., representative 2D and 3D views of P(L/D)LA 96/4 joint scaffold is illustrated in the Romexis programme. The general structure of the scaffolds can be recognized easily from 2D images. Also the structural changes such as empty regions in the middle of the scaffold can easily be seen from 2D view. Still the individual filaments could not be identified neither from the 2D nor 3D images, as it was assumed. The 3D view of the scaffold was poor because it did not give very realistic overview of the scaffold fibrous structure.

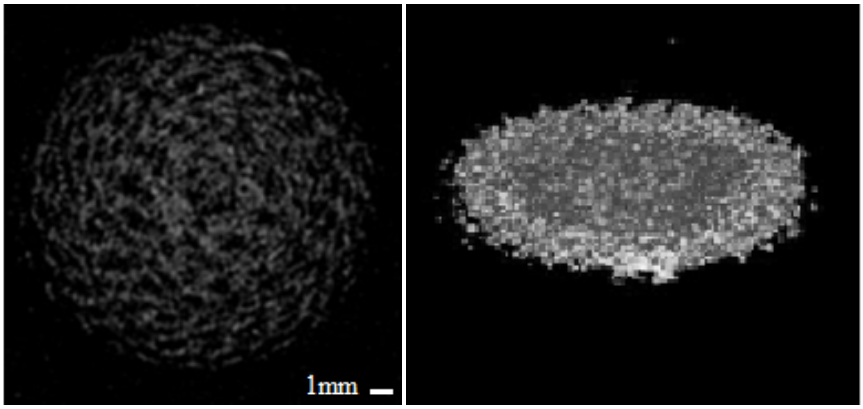

Figure 7.1. *A representative 2-dimensional slice image (left) and 3-dimensional view of gamma irradiated 20 mm P(L/D)LA 96/4 joint scaffold captured from the Romexis program.*

Both the X-ray contrast and the accuracy of grayscale images were moderate. Immediately after imaging the screen was completely black and it needed very careful thresholding and also adjustments for contrast and brightness before the scaffold structure could be distinguished from the background. It was also difficult to find operational imaging parameters because the range of suitable values for anode voltage and current proved to be very limited. If too high values for voltage and current were applied, the images were totally black. It may have been caused by the generating of too high energetic radiation which was not able to absorb into the low density polymer because of the weak absorbing ability of the material. If the imaging parameters were set to be lower than the suitable range, the scaffold structure could be distinguish from image but the images were very blurred. According to the literature, the blurring of images may have been caused by the noise [57].

7.1.2. SBF coated joint scaffolds

SBF coating improved the contrast of scaffold images and the success of coating process depended on the length of coating period. The sufficient coating period had to find by trial and error. Obtained images show that the coating did not penetrate through the entire structure of scaffold evenly if the coating period was only one or two days (Figure 7.2. (left)). However, the coating was evenly distributed into scaffold structure when scaffolds were coated for 5, 6 or 14 days as seen from right picture in Figure 7.2. It was perceived that sharp images can be acquired more easily from coated scaffolds

compared to uncoated scaffolds because the range of suitable imaging parameters was wider.

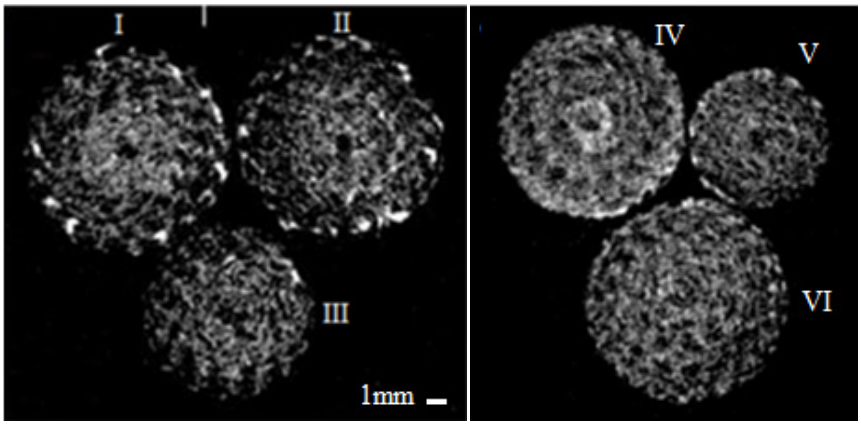

Figure 7.2. *Two-dimensional CBCT slice images of SBF coated P(L/D)LA 96/4 scaffolds. Left image has a one day coated (I), a two days coated (II) and uncoated scaffold (III). Right image has a 14 days coated (IV), five days coated (V) and six days coated (VI) scaffold.*

It was possible to visualize the polymeric and formed hydroxyapatite phases separately by manual thresholding. Hydroxyapatite formation started at the periphery and progressively went on towards the inner part of the scaffold. Similar observations have been made in an earlier study of SBF immersed bioactive-glass ceramic scaffolds [64].

The structure of the joint scaffolds was observed to harden and hardening was increased as a function of coating time. There was also a possibility that some pores were closed and thickness of filaments was increased. Also the filaments could be partly attached to each other. The thickness or volume of formed HA layers was not calculated but earlier study has shown that 5 and 14 days coating period resulted in 5 µm and 9 µm thick HA layer on scaffold surface [64]. Because of these structural changes, the visibility of the individual filaments from the images did not improve compared to the images of uncoated scaffolds. The degree of occurred structural changes in scaffolds was determined by measuring the changes in diameter, height and mass of the coated scaffolds and the results are represented in Chapter 7.6.

7.1.3. Hydroxyapatite and beta-tricalcium phosphate moulded joint scaffolds

Hydroxyapatite (HA) and beta-tricalcium phosphate (β-TCP) showed very strong absorbing ability of the X-ray irradiation and there were wide range of suitable imaging parameters. It was possible to assume the good visibility of HA and β-TCP because earlier studies have also proved it [6]. HA was observed to be even more clearly seen in images than β-TCP.

In spite of good CT visibility of HA and β-TCP, the fibrous structure of scaffold could not be recognized clearly from obtained images as seen from Figure 7.3. Because

of poor image quality it was assumed that reliable structural characterization could not be performed.

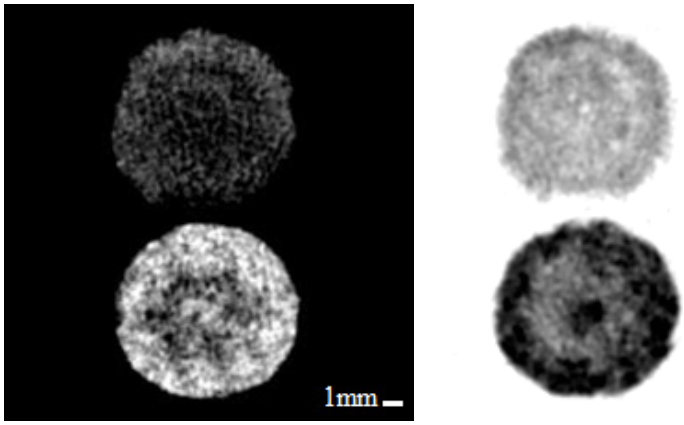

Figure 7.3. *Left 2D image represents hydroxyapatite (lower regions) and beta-tricalcium phosphate (upper regions) moulded joint scaffolds. Image is taken using 64 kV and 2 mA. The image is inverted afterwards with Slicer 3D and illustrated in right picture.*

Poor image quality may be due to that HA and β-TCP absorbed X-ray radiation too strongly and covered the thin polymeric regions from the images. Other disadvantage in this approach was that the HA and β-TCP was not completely evenly distributed in the scaffold structure. It was perhaps due to that the powder had not penetrated into the structure of the scaffold evenly during modification or then dried and brittle powder was partly fallen away from scaffold during transporting. Also the repeatability of this experiment is not good.

7.1.4. Joint scaffold immersed in iodine contrast medium

Applying of iodine contrast agent solution was easy because the solution was totally homogenous and thus there was no need to worry about of the formation of sediment as in imaging approaches of radio-opaque slurries. Also those structural changes which were observed due to SBF coating were not perceived. The image contrast seemed to depend on the concentration of iodine solution. As seen in Figure 7.4. the structure of the scaffold can be easily distinguished from the background.

The image quality seemed to be highest when the concentration of solution was lowest. Sufficient voltage value varied according to the ion concentration of the solution. The more concentrated the solution was, the higher anode voltage needed to get sharp images of polymeric structure.

The clear white dots in images (Fig. 7.4.) were found in each obtained images. It seemed that the dots had been created because of some air bubbles which were stuck in the fibrous structure. An attempt was made to remove them by pressing carefully the scaffold on a plastic rod but it did not succeeded completely. Remained dots lowered image quality significantly and caused that determination of structural parameters was not reasonable using these images.

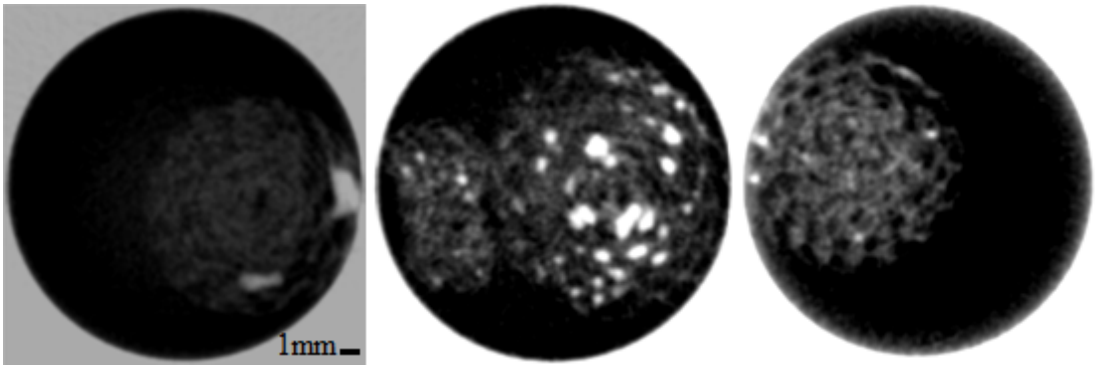

Figure 7.4. *Inverted representative 2D images of scaffolds immersed in three differently concentrated iodine solutions. Highest concentrated solution is on the left and lowest on the right. Two different scaffolds are immersed in middle image. Used parameters were 84 kV,13 mA, 80 kV, 13 mA and 68 kV,13 mA respectively.*

7.1.5. Joint scaffold scanned in radio-opaque slurries

Used powders mixed with water showed very strong radiocontrast abilities. The scaffold structure could be recognized from inverted images, but the contrast of scaffold phase remained near same as in the images of the scaffold without using any contrast enhancement. The contrast varies in images between different regions of the scaffold as seen in left image in Figure 7.5. That may be due that the powder was not totally evenly distributed in structure of specimen. Also the accuracy of inverted images seemed to be little weaker than images obtained without using contrast enhancement. The lower accuracy could be due to that the abilities of scaffold material and powders to absorb X-ray radiation differ too much from each other. One significant advantage using radio-opaque slurries instead of SBF coatings is that the use of slurries may not cause unwanted structural changes to the specimens.

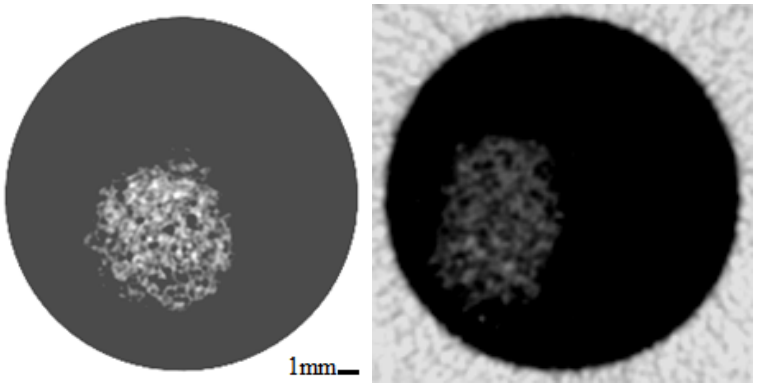

Figure 7.5. *Inverted representative 2D images of P(L/D)LA 96/4 scaffold immersed in $BaSO_4$ slurry (left) and HA slurry (right). Left image was acquired using scanning parameters of 72 kV and 10 mA and right image of 60 kV and 2 mA.*

The insolubility of the powders with water made the imaging approach difficult to perform, lowered the process repeatability and also weakened the image quality. Due to insolubility, the sediment layer was quickly formed to the bottom of the dish. Even

though the particle size was very small the slurries should be more homogenous so that the powder would be evenly distributed in the scaffold structure. The use of iodine contrast medium was easier to apply compared to use of radio-opaque slurries.

The scaffolds were immersed both in glass and polymer dishes filled with slurries. It was noticed that the quality of the images was affected by whether the scaffold was scanned immersed on a glass or on plastic dish. Also the suitable imaging parameters were different in case of plastic and glass dish. Higher voltage and current values were needed when scaffold was scanned on a glass dish due to better X-ray absorbing ability of glass.

7.2. Porosity degree

The porosity degree of joint scaffolds was determined using Planmeca ProMax 3Ds and SkyScan 1072 image data. The results from Planmeca study are presented first and results from SkyScan study after it. The results are compared and analyzed more deeply in Chapter 8.2.

Porosity degree determined using the Planmeca ProMax 3Ds data

Porosity degree of four types of hand-rolled joint scaffolds and SBF coated scaffolds was calculated using two different threshold levels and the results are presented in Table 7.2. The reference values, taken from the study of Sippola, are also presented in Table 7.2. Applied threshold methods were chosen based on their earlier performance as automatic method *Niblack* and manually thresholded level of 300-max produced porosity values nearest reference values.

Table 7.2. *Average porosity degree (%) of five types of joint scaffolds calculated using Planmeca ProMax image data using two different thresholding methods. The size of the SBF coated scaffolds was 18 mm (n = 5) and the rest of the scaffolds were 10 mm (n = 3). Reference values were taken from study of Sippola [70].*

Scaffold	Niblack	Upper error	Lower error
P	51.0	0.2	0.4
PC	51.7	0.5	1.0
PG	52.8	1.2	1.6
PCG	51.3	0.9	0.9
SBF coated	59.4	1.0	0.4
Scaffold	**300 - max**	**Upper error**	**Lower error**
P	70.6	3.3	2.5
PC	58.2	2.5	2.9
PG	52.9	7.0	7.6
PCG	54.3	2.9	4.7
SBF coated	53.1	10.8	10.6
Scaffold	**Mass technique**		
P	73.3		
PC	73.8		
PG	76.9		
PCG	75.4		

In P(L/D)LA 96/4 scaffold characterization, it was visually observed that the best performing local thresholding techniques were *Bernsen, MidGrey* and *Niblack* and global techniques *Shanbhag* and *MaxEntropy*. These techniques were applied to the CBCT image data for calculating the porosity degree values for P(L/D)LA 96/4 scaffolds. Also three constant manually adjusted threshold levels were applied. The results are shown in Table 7.3. with reference values which were measured using mass technique by Mutanen [47]. According to Mutanen's study, the average porosity degree of P(L/D)LA 96/4 joint scaffolds was 75.3 ± 3 % for all nine sizes of scaffolds (n = 10) and 75.7 % for six sizes presented in present study.

Table 7.3. *Average porosity degree (%) of P(L/D)LA 96/4 joint scaffolds calculated using Planmeca ProMax image data applying eight different thresholding levels. Standard deviation values are in parentheses. Also the reference values (mass technique) are included. Image based determined porosity was calculated as an average of six parallel samples except scaffold size 18 mm where n = 5. Reference values were taken from study of Mutanen [47].*

Scaffold	Bernsen	MidGrey	Niblack
8 mm	33.4 (3.3)	34.6 (3.5)	45.4 (1.5)
10 mm	43.3 (3.9)	44.5 (4.0)	52.3 (1.2)
12 mm	44.8 (2.3)	46.0 (2.5)	54.0 (1.0)
14 mm	45.9 (1.0)	47.0 (1.0)	54.6 (0.6)
18 mm	47.7 (2.3)	48.9 (2.2)	55.9 (0.6)
20 mm	47.0 (1.8)	48.1 (1.8)	55.9 (0.4)
Scaffold	**Shanbhag**	**MaxEntropy**	**M (300-max)**
8 mm	26.4 (4.0)	12.0 (6.0)	49.1 (6.9)
10 mm	35.3 (2.1)	25.3 (26.1)	87.8 (4.0)
12 mm	33.7 (2.2)	18.1 (7.0)	86.8 (2.5)
14 mm	31.7 (1.3)	22.9 (4.3)	83.7 (1.0)
18 mm	35.3 (1.9)	26.4 (11.2)	80.9 (8.7)
20 mm	32.3 (1.4)	20.0 (5.1)	80.1 (10.4)
Scaffold	**M (265-max)**	**M (192-max)**	**Mass technique**
8 mm	31.9 (5.9)	8.4 (2.9)	69.5 (1.7)
10 mm	72.8 (7.3)	30.7 (8.5)	74.8 (1.3)
12 mm	72.1 (3.9)	30.8 (5.1)	76.0 (1.3)
14 mm	68.4 (0.9)	29.8 (0.8)	78.5 (1.2)
18 mm	66.0 (11.9)	30.1 (11.6)	78.1 (1.2)
20 mm	64.9 (12.9)	26.3 (8.8)	77.2 (0.9)

Porosity degree determined using the SkyScan 1072 data

Porosity degree of five different types of joint scaffolds was determined using obtained SkyScan-1072 µCT image data. Each image set was thresholded using a constant manually adjusted level of 50. The results are presented in Table 7.4. Analyzed samples were also studied in previous Planmeca study but the number of reference samples was different.

Table 7.4. *Average porosity degree (%) of five types of joint scaffolds calculated from SkyScan-1072µCT data using manually set threshold level of 50. Four parallel 8 mm scaffold and two parallel hand-rolled scaffolds were analyzed.*

Scaffold	Size	Porosity	Lower error bar	Upper error bar
P(L/D)LA	8	67.3	2.1	2.4
P	10	71.2	1.5	1.5
PC	10	68.0	0.7	0.7
PG	10	55.1	1.7	1.7
PCG	10	62.6	1.9	1.9

7.3. Porosity distribution in scaffold architecture

The porosity distribution in P(L/D)LA 96/4 joint scaffold structure was determined for six different scaffold sizes using Planmeca ProMax 3Ds image data as described in Chapter 6.6.4. First, the results determined from the horizontal direction are presented and then in vertical direction. One must notice that the amount of reference samples varies in determinations.

Distribution in horizontal direction

Porosity distribution was determined using Planmeca CBCT image data where the measured volume of the scaffold was divided to three different segments horizontally as illustrated in Figure 6.10. Image data was thresholded using automatic *Niblack* method and manually set level of 300-max. The results with error bars are presented in Figures 7.6. and 7.7.

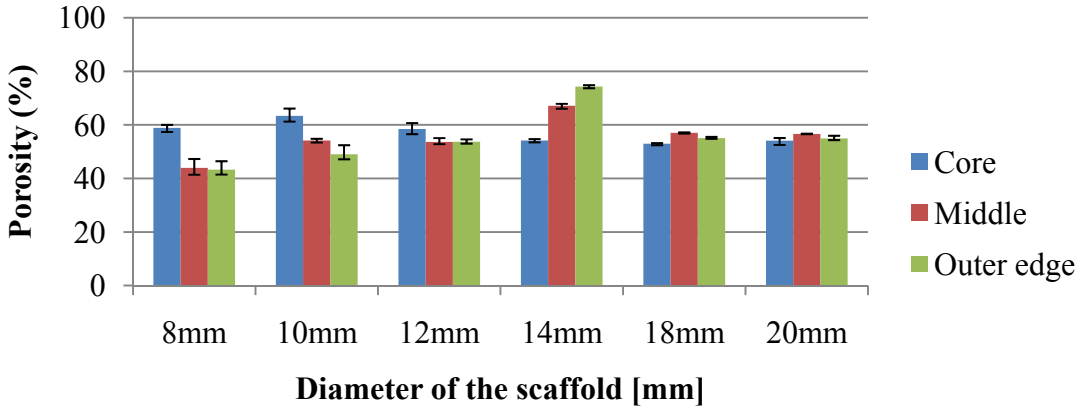

Figure 7.6. *Porosity degree of three different segments of P(L/D)LA 96/4 scaffold structure calculated in horizontal direction. Planmeca CBCT image data was thresholded using automatic threshold method Niblack. n = 3.*

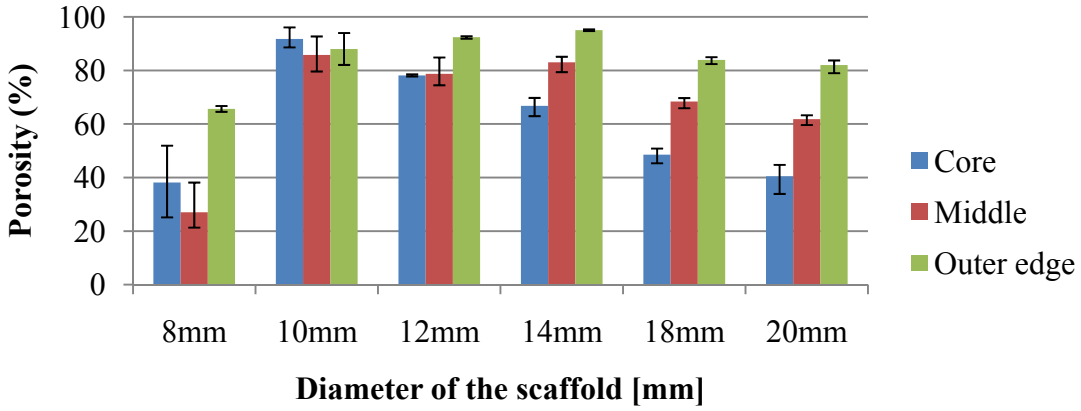

Figure 7.7. *Porosity degree of three different segments of P(L/D)LA 96/4 scaffold structure calculated in horizontal direction. Planmeca CBCT image data was manually thresholded using constant levels of 300-max. n = 3.*

Core segment means the innermost part of the scaffold looked from above and the *outer edge* segment describes the outermost parts of the sample. *Middle* segment means the region between *core* and *outer edge.*

The porosity distribution was also calculated using smaller segments. The scaffold volume was divided into several segments according to the size of the scaffold. Number of reference samples was five for 18 mm scaffolds and six for other scaffold sizes. The results with error bars are presented in bar charts in Figure 7.8.

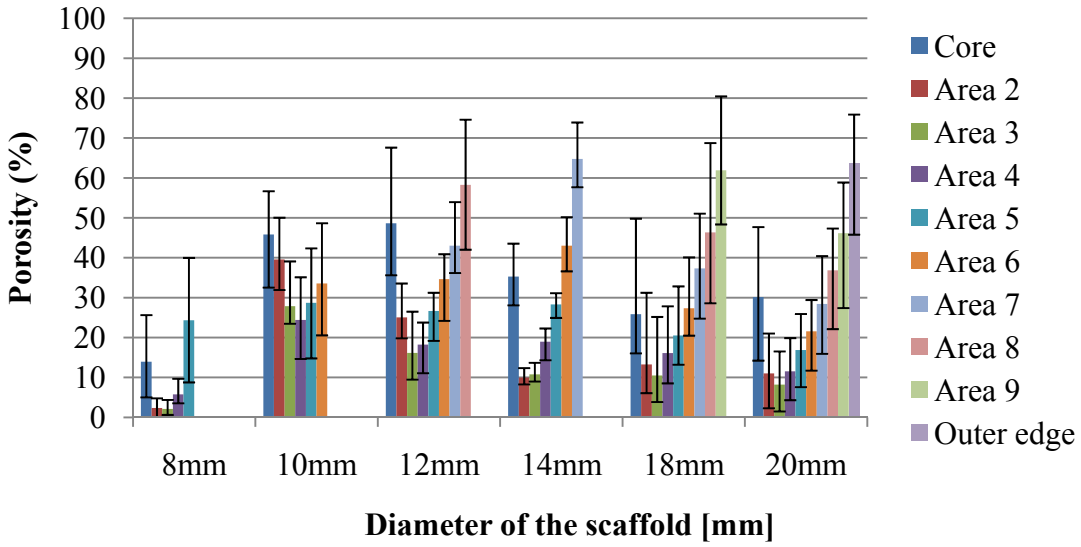

Figure 7.8. *Porosity degree of several different segments of P(L/D)LA 96/4 scaffold structure calculated in horizontal direction. Planmeca CBCT image data was manually thresholded using constant levels of 192-max. n = 6 (except size 18 mm in which n = 5).*

Distribution in vertical direction

Image data was analyzed for six scaffold sizes. Results with error bars are presented in bar charts in Figure 7.9., where the porosity degree of each segment is presented.

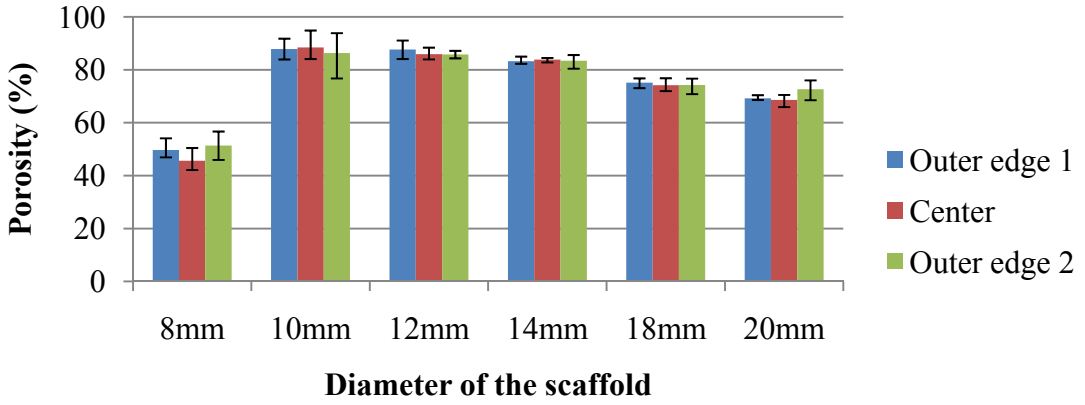

Figure 7.9. *Porosity degree in three different segments in P(L/D)LA 96/4 scaffold structure calculated in vertical direction. Planmeca CBCT image data was manually thresholded using constant levels of 300-max. n = 3.*

Analysis was performed so that the measured volume of the scaffold was divided to three separate segments vertically and then porosity degree of each segment was calculated. One segment consisted of 10 circularly cropped slice images. The *outer edge 1* and *outer edge 2* describes the top and bottom regions of the scaffolds when the sample is looked from the side. The *center* describes the region between the *outer edge 1* and *outer edge 2*. Three parallel samples were determined.

The image data was analyzed also such that the porosity of each 2D image was calculated without dividing the volume to three segments. Only one sample of each scaffold size was determined because each sample volume consisted of different number of slices. Measurements resulted in a continuous curve as presented in Figure 7.10. The length of the each line curve describes the number of applied 2D images and thus also the height of the measured volume. Because the physical height of the scaffolds varied, also the measured volume and length of the curve varies according to scaffold physical size.

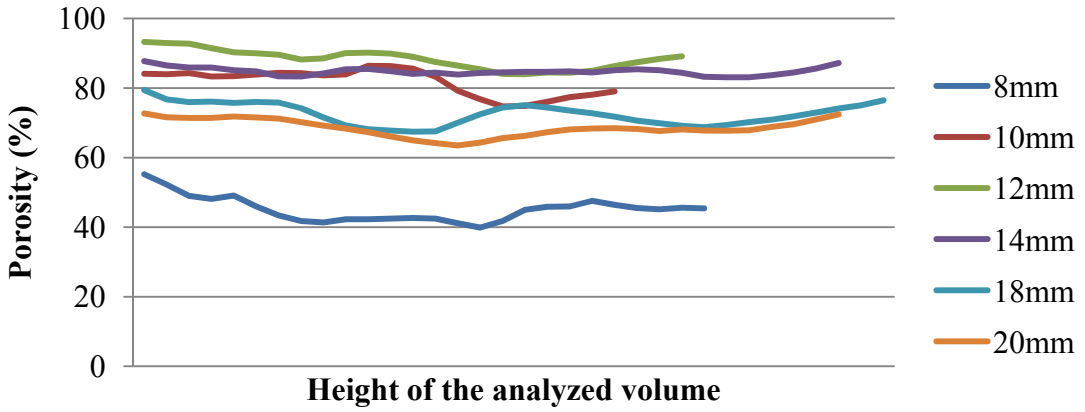

Figure 7.10. *Porosity degree distribution in P(L/D)LA 96/4 scaffold determined in vertical direction. Planmeca CBCT image data was manually thresholded using a level of 300-max, n = 1.*

7.4. Pore analysis

Volumetric pore analysis was performed using both Planmeca ProMax 3Ds and SkyScan 1072 image data. The results from Planmeca study are presented first and results from SkyScan study after it.

Pore volume distribution determined using the Planmeca ProMax 3Ds data

Pore volume distribution of the P(L/D)LA 96/4 joint scaffolds was determined for six scaffold sizes using three parallel samples. Image data was thresholded using *Niblack* method. Pore Analyzer produced a 3D reconstruction model from the core of the specimen using quadratic cropped 2D image sets as illustrated in Figure 7.11. Grey regions in 3D model represent polymer phase and the rest empty regions. Empty regions are filled with the spherical volumes of different sizes.

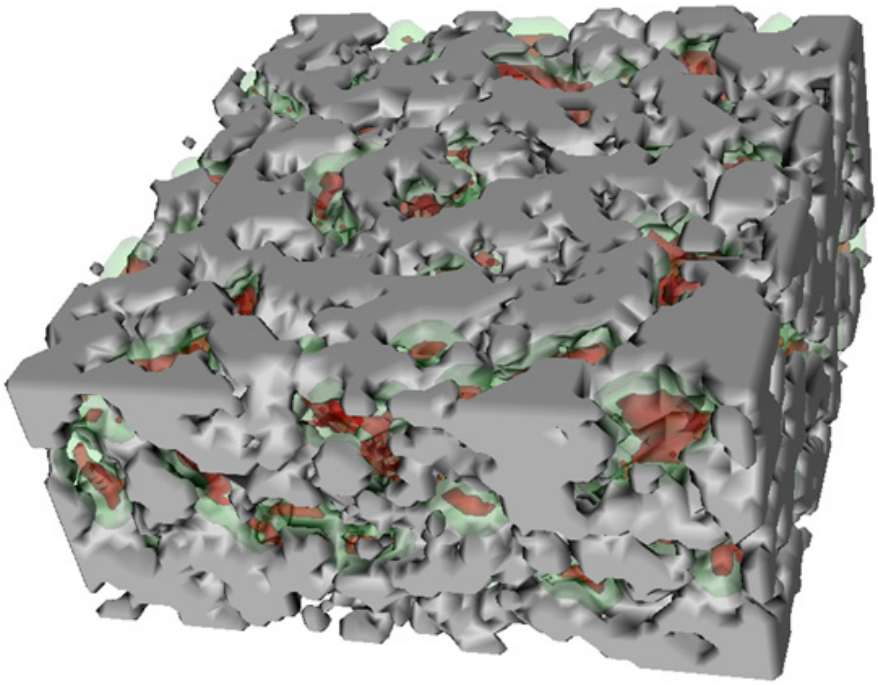

Figure 7.11. *Representative 3D reconstructed model from the core of 12 mm P(L/D)LA 96/4 joint scaffold. Image acquisition was performed using Planmeca ProMax 3Ds and 3D model was produced using Pore Analyzer program. Image set was thresholded using Niblack method.*

The results from pore analysis with error bars are presented in Figure 7.12. In the bar graft, *100um pores* describes the percentual share of 100 ± 15 µm pore volume of total analyzed volume, *200um pores* describes the percentual share of 200 ± 15 µm pore volume of total analyzed volume and *300um pores* describes the percentual share of 300 ± 20 µm pore volume of total analyzed volume. Analyzed volume describes the sample core average volume when n = 3.

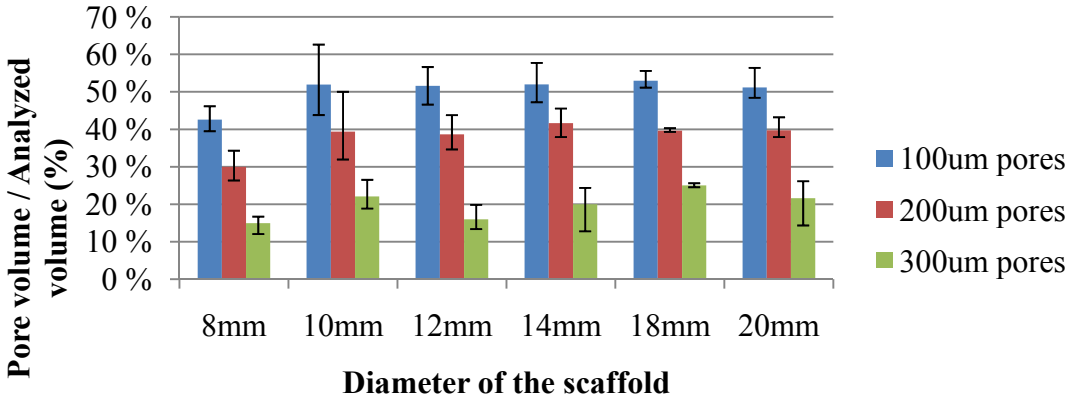

Figure 7.12. *Pore analysis using Planmeca ProMax image data. Data was thresholded using automatic threshold method (Niblack). Columns describe the percentual share of the fitted sphere volume of the analyzed volume. The fitted sphere volumes are calculated for three different sphere sizes. n = 3.*

Pore volume distribution determined using the SkyScan 1072 data

Volumetric pore volume distribution was determined for 8 mm P(L/D)LA 96/4 scaffolds and for hand-rolled scaffolds. Two 8 mm scaffolds and one of each hand-rolled scaffold types were analyzed. Image data was thresholded using manually set level of 50 for 8 mm P(L/D)LA 96/4, P and PC type scaffolds. Threshold level was 10 and 15 for PG and PCG scaffolds, respectively. The results with error bars are presented in Figure 7.13. In bar graft, *100um pores* describe the percentual share of 100 ± 10 µm pore volume of total analyzed volume, *200um pores* describes the percentual share of 200 ± 15 µm pore volume of total analyzed volume and *300um pores* describes the percentual share of 300 ± 35 µm pore volume of total analyzed volume. Pore Analyzer program produced a 3D reconstructed model from the core of each analyzed sample. Representative SkyScan-1072 3D model is illustrated in Figure 7.14.

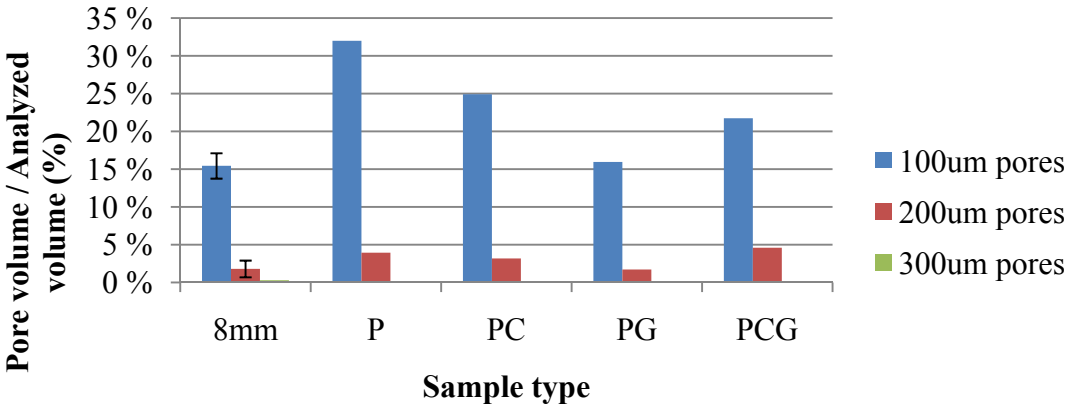

Figure 7.13. *Pore analysis using SkyScan µCT image data. Data was thresholded using manually adjusted levels. Columns describe the percentual share of the fitted sphere volume of analyzed volume. The fitted sphere volumes are calculated for three different sphere sizes. For 8 mm samples n = 2 and for rest n = 1.*

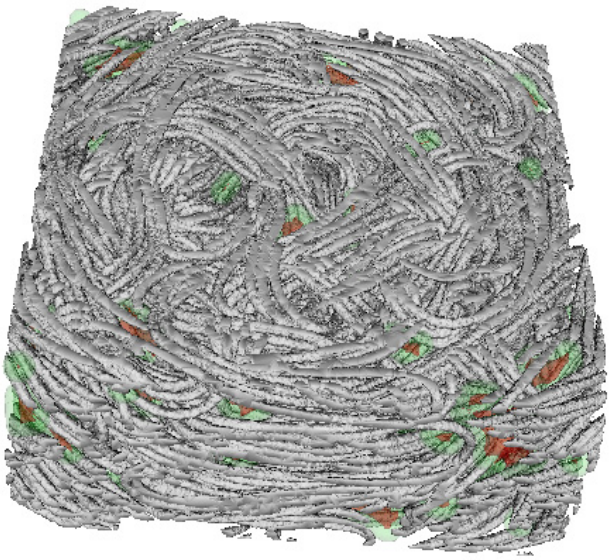

Figure 7.14. *Representative 3D reconstructed model from the core of 8 mm P(L/D)LA 96/4 joint scaffold. Image acquisition was performed using SkyScan-1072 and 3D model was produced using Pore Analyzer program. Image set was thresholded using manually set level of 50.*

7.5. Glass content determination

Percentual glass content of hand-rolled PG and PCG type scaffolds was determined using both Planmeca ProMax 3Ds and SkyScan 1072 image data. Results from Planmeca study are presented first and then results from SkyScan study.

Glass content determined using the Planmeca ProMax 3Ds data

Image sets were thresholded using a constant manually set level of 450 and three parallel samples were examined. Glass content was determined from the core of the samples and the size of the analyzed volume was same for all samples (261.0 mm³). Results with error bars are presented in Figure 7.15.

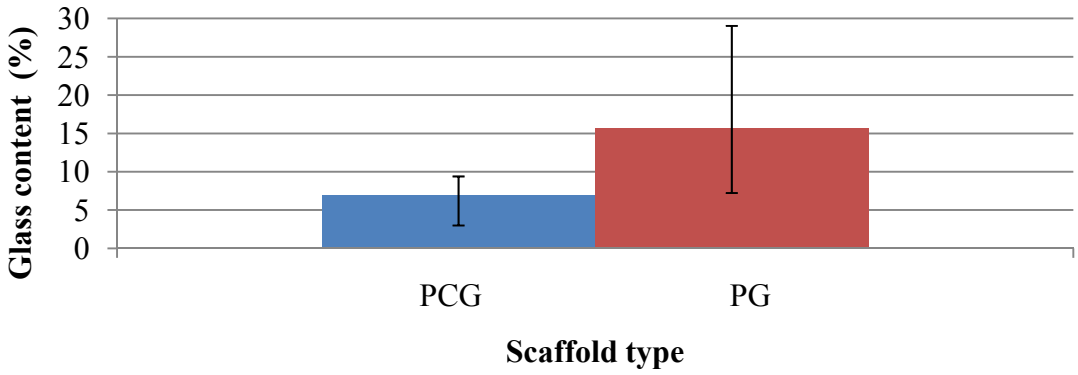

Figure 7.15. *Percentual glass content of PG and PCG type scaffolds calculated using Planmeca ProMax image data. Data was thresholded using a constant level of 450. n = 3.*

Glass content determined using the SkyScan-1072 data

The glass content was determined from SkyScan μCT images using two different manually set threshold levels. The analyzed physical volume remained constant for each sample and it was 276.5 mm³. The results are presented in Figure 7.16.

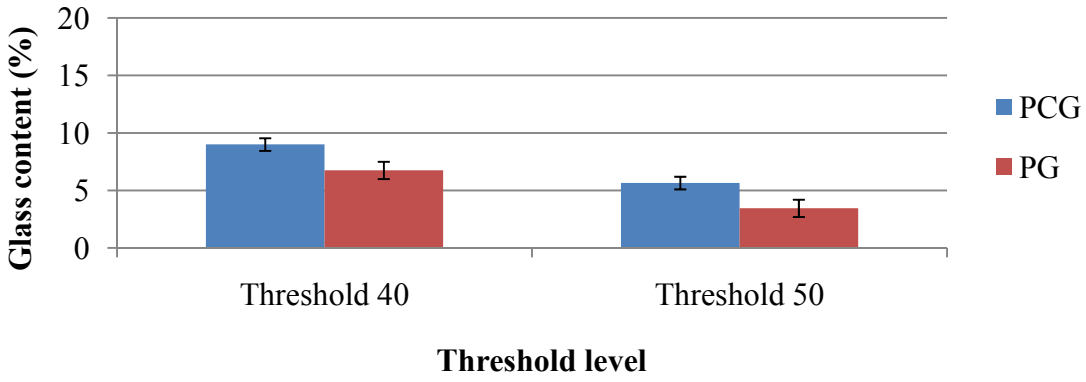

Figure 7.16. *Percentual glass content of two different types of joint scaffolds calculated using SkyScan-1072 image data. Data was thresholded using two different manually adjusted levels. n = 2.*

7.6. Structural changes of SBF coated scaffolds

Changes in mass, diameter and height were determined for five 18 mm scaffolds which were coated using SBF solution. The results are presented in Table 7.5. The values of columns were obtained by deducting the values that were measured after coating from the values that were measured prior coating. Mass changes are presented in milligrams and dimension changes in millimetres. Also the values for percentual and average change are calculated and presented.

Table 7.5. *Mass, diameter and height of 18 mm scaffolds determined prior and after SBF coating. Values are averages and calculated using 5 parallel samples. Standard deviation values are in parentheses.*

Mass prior coating [mg]	**Mass after coating [mg]**	**Percentual mass change [%]**
368.8 (42.4)	449.6 (32.3)	22.4 (6.4)
Diameter prior coating [mm]	**Diameter after coating [mm]**	**Percentual diameter change [%]**
18.2 (0.3)	17.9 (0.4)	-1.7 (0.9)
Height prior coating [mm]	**Height after coating [mm]**	**Percentual height change [%]**
5.2 (0.3)	6.5 (0.5)	26.0 (3.3)

8. DISCUSSION

The results from performed studies are interpreted in this chapter. The image acquisition process using Planmeca ProMax 3Ds is described in Chapter 8.1. The success and reliability of image-based calculated structural parameters are discussed in Chapters 8.2.-8.5, 8.7. and 8.8. Effects of SBF coating to scaffold structure are discussed in Chapter 8.6. and suitability of experimented CT devices for scaffold characterization is discussed in Chapter 8.9.

8.1. Image acquisition using Planmeca ProMax 3Ds

Even at the beginning of this study, it was assumed that the accuracy of the Planmeca ProMax 3Ds (detector resolution 127 μm x 127 μm) is not sufficient to identify individual filaments (diameter of ~80 μm) of the fibrous structure of P(L/D)LA 96/4 joint scaffold and obtained images proved that assumption to be true. The differences in image accuracy can be seen if Planmeca ProMax and SkyScan-1072 images are visually compared. Planmeca and SkyScan images which correspond to each other are for example 3D reconstructed models in Figure 7.11. and Figure 7.14. It is also earlier reported, that the reliable scaffold characterization requires that the resolution of obtained CT images is finer than the minimal pore size or wall thickness of the specimen and this statement did not occur in Planmeca study [14].

Other factor which weakened quality of Planmeca ProMax images was moderate contrast. Even after the optimization of scanning parameters, the contrast was still not as good as needed. The scanning parameters in Planmeca ProMax 3Ds (54-84 kV and 1-16 mA) are maybe too high for polymer imaging which may cause that the X-ray irradiation did not absorb into material and thus it impaired of contrast. For example micro-CT scanning was performed using parameters of 50 kV and 197 μA which cannot be used in Planmeca device. However, the contrast in obtained Planmeca images was good enough that it was possible to use them to calculate structural parameters.

The use of simulated body fluid coating and iodine contrast medium as well as barium sulphate, hydroxyapatite and tricalcium phosphate slurries as contrast enhancement agents seemed to improve the image contrast. The image quality enhancement was still insignificant. There were more drawbacks in these approaches than advantages. Computed tomography is commonly considered as a non-destructive testing method, but so that it also would remain such, the imaging should be performed without using any contrast enhancement which damages the samples. Each applied contrast enhancements technique ruined the sample and thus the same scaffolds could

not be used clinically after scanning. Therefore scaffold imaging without contrast enhancement in air is the most suitable approach in scaffold characterization. Also the comfort and the repeatability of the characterizing process are highest when no contrast enhancement is used. This has to be taken into consideration if the device will be used later in the quality control of the manufacturing process.

Visual evaluation of the images of P(L/D)LA 96/4 scaffold and SBF coated scaffolds was more practical to perform than other images because the images could be assessed without inverting the threshold. This made the evaluation much faster and comfortable to perform. The problem was related to Planmeca Romexis 3D Explorer image analysis program which was not able to invert images. Therefore the use of Slicer 3D and ImageJ was required for that.

The suitable imaging parameters for each approach found by trial and error. The functional values varied according to each approach and the rough estimates for suitable ranges are presented in Table 8.1. On the basis of the obtained images, it seemed that the material class and the medium around the sample affected most to the functionality of applied imaging parameters and thus image quality. Smaller imaging parameters were performed better if the scaffold was scanned in air compared if the sample was scanned immersed in radio-opaque solutions. That could be due to that air absorbs less X-ray irradiation than radio-opaque solutions. Also the glass dish absorbs more radiation and thus needed higher anode voltage and current than polymer dish. It was noticed that the range of suitable imaging parameters was generally wider for ceramic materials than for polymers. No significant advantage from the use of filtering in present study was noticed and therefore those sheets were not used in final imaging.

Table 8.1. *Ranges of functional imaging parameters for each performed Planmeca ProMax 3Ds experiment without filtering.*

Scaffold type	Contrast agent	Voltage [kV]	Current [mA]
P(L/D)LA 96/4	-	60-64	10-16
P(L/D)LA 96/4	Water	-	-
P(L/D)LA 96/4	SBF coating	56-64	7-16
P(L/D)LA 96/4	Iodine solution	68-84	6-16
P(L/D)LA 96/4	HA slurry	60-72	2-10
P(L/D)LA 96/4	β-TCP slurry	60-72	2-10
P(L/D)LA 96/4	$BaSO_4$ slurry	72-84	10-16
P(L/D)LA 96/4	SBF solution	-	-
P(L/D)LA 96/4	HA molded scaffold	56-66	1-16
P(L/D)LA 96/4	β-TCP molded scaffold	56-66	1-16

Some of the imaging approaches were unsuccessful. When scaffolds were scanned immersed in pure water and SBF solution, the scaffold structure could not be recognized. In case of water, this could be due to that the absorbing ability of the X-ray radiation of water and low density polymer (P(L/D)LA 96/4) is nearly same [33]. In

case of SBF solution, the images were blurred maybe due to the heterogeneous nature of the SBF solution. Because of that the solution was not seen as evenly background and thus the structure of the scaffold could not be distinguished clearly.

8.2. Porosity degree determination

Both SkyScan-1072 and Planmeca ProMax 3Ds studies showed the sensitivity of image-based determined porosity degree values to the applied threshold level. Thus, it was reasonable to calculate and present the values using several threshold levels as it was also recommended in literature (Chapter 3.5.) [26]. The results can be considered reliable if their calculated values are of the same size with reference values and if the images match visually with real structure [26; 28; 61]. As it is seen from the results of the Planmeca ProMax 3Ds study (Table 7.2. and Table 7.3.) not one of the automatic thresholding methods produced results near of the same size than the mass technique. However, the local threshold techniques functioned better than the global methods. Similar observations have been reported earlier by Rajagopalan *et al.* [61]. *Niblack* performed best producing an average porosity which still differed more than 30 % from reference values. The calculated porosity degree values using global threshold methods *Shanbhag* and *MaxEntropy* seemed to be poor because they differed approximately 57 % and 73 % from reference values, respectively. The porosity values achieved from Planmeca study are closer to the reference values using a constant manually adjusted threshold level, but even so, thresholding may not be very reliable because of several possible error factors related to manually set threshold levels, described in Chapter 3.5. The average porosity degree of all six sizes of P(L/D)LA 96/4 scaffolds differed only 3 % from reference values. One must notice that the image based determined values and reference values do not need to correlate exactly with each other because studied specimens were not same, but however, the values should be nearly same. When results are examined, it is also good to pay attention that image-based determined porosity values do not correspond to real sample perfectly because the analyzed sample volume represented the core volume of the sample without taking into account the fringe parts of the sample.

Porosity variation between different sizes of scaffolds is not unambiguous. For example, according to Planmeca study (Table 7.3.) the porosity determined using local threshold methods (*Niblack, Bernsen and MidGrey*) increased when the size of the scaffold increases whereas when manually adjusted threshold levels were applied, the porosity was the highest on medium-sized (Ø = 10 and 12 mm) scaffolds. According to Mutanen's mass technique experiment, the porosity was highest for 14 mm and 18 mm scaffolds.

The deviation of porosity degree values between parallel samples seemed to be in general smaller using automatic threshold methods than manually set levels except *MaxEntropy* which produced a deviation which was distinctly larger than others. Standard deviation of porosity values was the smallest on 14 mm scaffolds except

Niblack method and mass technique which both produced the smallest deviation for 18 mm scaffolds.

The SBF coating process formed a HA layer on 18 mm scaffold structure because of which it was assumed that porosity degree would decrease. That assumption came true if the manually thresholded and calculated values are compared. Before coating the porosity degree was approximately 81 % and afterwards 53 %. Renghini *et al.* has reported similar observations [64]. However, in this study, the similar decrease in porosity did not occur when the automatically thresholded image data was calculated. Once again the sensitivity of porosity values to the applied threshold levels was proved.

Micro-CT study observed to produce more reliable results for porosity degree (Table 7.4.) as the visual view of the images was good and also calculated values were near reference values. The image based determined porosity values of P, PC and 8 mm P(L/D)LA 96/4 scaffolds were only a slight underestimation compared to the reference values. The porosity degree of glass containing scaffolds PG and PCG were bigger underestimation compared to the reference values. Images of PG and PCG scaffolds were challenging to threshold so that every material phase would exist in images and look realistic. The difficulties in thresholding may have caused the error also to the porosity values. Polymer and glass possess X-ray contrast very differently and that could be the reason which made the thresholding problematic. A representative SkyScan-1072 reconstructed 3D model of PCG scaffold illustrating the blurred visual view of scaffold structure is shown in Appendix 4.

8.3. Porosity distribution in scaffold architecture

According to the results in horizontal distribution (Fig. 7.6., 7.7. and 7.8.) one can perceive that porosity variation calculated using automatic and manual thresholded data has produced differing results. However, the distribution calculated using two manually set levels (192 and 300) has produced more similar results. Because the results are not unanimous and are so sensitive to applied threshold level, it is hard to conclude how the porosity degree really varies in scaffold structure.

However, it is clear that the porosity is not constant in scaffold structure and the distribution seems to be higher in horizontal direction than in vertical direction as the Figure 7.7. and 7.9. shows. According to the results calculated using manually thresholded data (Fig. 7.7. & 7.8.) in horizontal distribution, it can be roughly conclude that the porosity degree is higher in the core and in the outermost parts of the scaffold compared to the middle regions. The high porosity degree in the core region of the semiautomatically rolled scaffolds can be explained by that the reeling machine may have caused the hole in the middle of the scaffold. According to the results calculated using automatically thresholded (*Niblack*) data (Fig. 7.6.), the porosity distribution seems to be smaller in scaffold structure.

Porosity variation in vertical direction seems to be very small as the highest variation occurs on 8 mm scaffold structure whereas the lowest porosity variation

occurs on 14 mm scaffolds. According to the Figure 7.9., the porosity difference between center and outer edge in 8 mm scaffolds is approximately 6 %. The smallest porosity variation seems to be on 14 mm scaffolds where the largest fluctuation is approximately 1 %. The results from Figure 7.10. show also that the distribution is highest on 8 mm scaffolds and smallest on 14 mm scaffolds.

8.4. Pore analysis

Volumetric pore analysis was performed using both Planmeca and SkyScan image data. Reliability of the results can be evaluated from produced 3D models of analyzed sample core volumes illustrated in Figures 7.11. and 7.14. Pore analysis using Planmeca data cannot be considered reliable because the 3D model is not similar with real scaffold structure. The SkyScan-1072 reconstructed model instead is much more realistic and therefore it can be assumed, that the calculated numerical values are also much more reliable. However, the quality of μCT models of glass containing scaffolds (PG and PCG) were not as good as models of polymeric scaffolds.

One must notice that the earlier performed pore analysis studies and the pore analysis study in the present work differ considerably from each other. Sippola [70] determined pore sizes of the hand-rolled scaffolds by measuring the distances between filaments from 2D microscope images of the scaffold using computerized image analysis and Mutanen [47] determined the pore sizes of P(L/D)LA 96/4 scaffolds using similar technique. In this study, the pore analysis was performed using 3D volumetric data instead of using single 2D images. Therefore, performed 3D pore analysis was more comprehensive and describes better the 3D nature of joint scaffolds.

The outcome of these studies is different as Mutanen and Sippola calculated the average pore diameter of scaffolds (distance between filaments) but in the present study, the percentual total pore volume was determined. Performed volumetric pore analysis has not been done for P(L/D)LA 96/4, P, PC, PG or PCG type scaffolds earlier so there are no comparative results available.

8.5. Glass content determination

The percentual glass content was calculated for PG and PCG scaffolds using both Planmeca ProMax 3Ds and SkyScan-1072 image data. It was challenging to distinguish the glass phase from polymer phase from Planmeca images by thresholding which weakened the reliability of the characterisation (Figure 7.15.). The difference in image accuracy is obviously seen if the Planmeca image (Figure 6.11.) and SkyScan image (Figure 6.13.) are visually compared. It was easy to threshold the polymer phase invisible from the SkyScan images what also improved the reliability of the calculated glass content values.

As seen from the results of SkyScan study (Figure 7.16.), even a slight change in the threshold level affected significantly to calculated values of glass content. Threshold

level was set manually and it was proved to be challenging to adjust it exactly correct based on visual assessment because the images thresholded using levels of 40 and 50 looked very similar.

Calculated values for glass content are probably a slight overestimation from true values because the images were cropped so that the fringe areas of the scaffold did not include in analyzed volume as it is seen from Figure 6.13. Fringe areas consisted only of polymeric phase because the rolled glass sheet was shorter than the P(L/D)LA 96/4 knitting and thus the glass phase did not reach to the outer edges of the scaffold [70].

Theoretically it would have been possible to measure also the chitosan content in the same way as the glass content was determined. However, it proved that it was not possible to distinguish P(L/D)LA 96/4 and chitosan phases from CT images, probably due to their similar abilities to absorb X-ray irradiation. Similar absorbing ability results same contrast levels in images. Sippola showed that these two polymer phases could be distinguished from 2D SEM images as it is illustrated in Figure 6.6. (right) but the determination of chitosan or glass content was not performed in her study [70]. This was the first study in which the glass content of the hand-rolled scaffolds was determined.

8.6. Structural changes of SBF coated scaffolds

According to the results from Table 7.5., it can be easily said that the coating process affected both the mass and the dimensions of scaffold. The mass of each sample significantly increased (22.4 %) after coating. It was possible to predict the increase of the mass because the formed biomimetic coating layer was visible on scaffold filaments as shown in Figure 6.3.

The height of each sample increased after coating but the change in diameter was opposite as it was observed to decrease. However, the change in diameter was low, only 1.7 %. The perceived changes can be explained as the structure of the scaffold seems to be returned to its original form in which it was prior heat treatment. Studied P(L/D)LA 96/4 scaffolds have been heat-treated which gives the final form to the scaffold and the process is studied earlier by Mutanen [47] and Kulmala [39]. They observed that the heat treatment in mould shrank polymer fibers and decrease pore sizes and dimensions of the scaffold. In the present study, the simulated body fluid solution, in which the sample was immersed during the coating process, may have caused the relaxation of fibers and thus scaffold dimensions changed in the direction in which they were before the heat treatment. [39; 47] Kulmala reported that gamma sterilization of P(L/D)LA 96/4 scaffold (heat treated at 80 °C) has resulted growth in scaffold height and diameter, approximately 0.05 mm and 0.02 mm, respectively [39]. According to Mutanen, hydrolysis tests of P(L/D)LA 96/4 fibers *in vitro* showed changes in tensile strength, molecular weight, crystallinity and glass transition temperature of the polymer but the effect of the hydrolysis on the dimensions was not reported [47].

8.7. Correlation between mass, volume and porosity degree of P(L/D)LA 96/4 scaffolds

The purpose was to examine if the mass differences affect the porosity degree values and also to consider if there is correlation between mass, porosity and volume of the scaffolds. Porosity degree, mass and volume of P(L/D)LA 96/4 joint scaffolds (n = 35) were determined and results for each sample are presented in Table 8.2. The porosity degree was determined from Planmeca images which were thresholded using a manually adjusted level of 300. Volume values are rough estimations, determined using an equation for cylindrical volume as described in Chapter 6.5. Volume is expressed in cubic millimeters and mass in milligrams. Table 8.2. also includes the average (aver.) and standard deviation values (stdv.) calculated for each scaffold size.

Table 8.2. *Comparison of mass, porosity degree and volume of P(L/D)LA 96/4 scaffolds.*

Sample	Mass [mg]	Porosity [%]	Volume [mm³]	Sample	Mass [mg]	Porosity [%]	Volume [mm³]
8mm 1	74.5	45.1	187.5	**14mm 1**	191.9	84.8	746.1
8mm 2	62.8	47.3	186.0	**14mm 2**	169.3	81.9	648.6
8mm 3	66.3	53.6	186.7	**14mm 3**	189.0	84.4	742.3
8mm 4	76.0	55.5	214.8	**14mm 4**	175.3	83.2	678.6
8mm 5	77.5	38.1	192.5	**14mm 5**	174.1	83.9	618.3
8mm 6	71.8	55.1	197.3	**14mm 6**	188.4	83.8	760.1
aver.	**71.5**	**49.1**	**194.1**	**aver.**	**181.3**	**83.7**	**699.0**
stdv.	**5.8**	**6.9**	**11.0**	**stdv.**	**9.5**	**1.0**	**58.8**
10mm 1	98.1	81.7	332.3	**18mm 1**	409.1	72.5	1275.3
10mm 2	99.7	87.6	402.4	**18mm 2**	398.2	76.0	1327.4
10mm 3	81.3	93.6	361.9	**18mm 3**	390.7	75.8	1331.2
10mm 4	86.1	90.5	340.4	**18mm 4**	328.1	92.7	1442.9
10mm 5	94.3	87.1	339.2	**18mm 5**	318.1	87.6	1320.0
10mm 6	101.7	86.1	378.8				
aver.	**93.5**	**87.8**	**359.1**	**aver.**	**368.8**	**80.9**	**1339.3**
stdv.	**8.1**	**4.0**	**27.3**	**stdv.**	**42.4**	**8.7**	**62.1**
12mm 1	127.7	88.4	501.1	**20mm 1**	539.1	68.5	1719.6
12mm 2	134.2	84.7	467.2	**20mm 2**	466.6	70.9	1586.3
12mm 3	124.3	86.2	461.6	**20mm 3**	490.5	72.7	1656.8
12mm 4	145.6	89.8	580.1	**20mm 4**	419.2	88.0	1801.0
12mm 5	139.2	83.5	499.7	**20mm 5**	433.0	90.0	1746.7
12mm 6	133.5	88.4	511.6	**20mm 6**	437.4	90.4	1901.4
aver.	**134.1**	**86.8**	**503.6**	**aver.**	**464.3**	**80.1**	**1735.3**
stdv.	**7.7**	**2.4**	**42.5**	**stdv.**	**44.8**	**10.4**	**110.1**

The values in Table 8.2. proved to be unanimous and it seems that there is no clear correlation between porosity degree, mass and volume. Theoretically, the large mass value should correspond to low porosity value if the volume remains constant. According to the results, the highest mass and lowest porosity value match on 8 mm, 18 mm and 20 mm scaffolds. Lowest mass value and highest porosity value match only on 10 mm scaffolds. If the three lowest mass values and three highest porosity values are compared, it can be observed that all the three values match only on 20 mm scaffolds.

The standard deviation of mass, porosity degree and volume values were highest for 20 mm scaffolds. The distribution of porosity was lowest on 14 mm scaffolds whereas the dispersion of mass and volume values were lowest on 8 mm scaffolds.

8.8. Reliability of image-based characterization

The reliability of the determination of structural parameters depends on the properties of the CT device and sample material (as described in Chapter 8.1.), but also from how the image analysis process has been carried out. During the Planmeca study, it was perceived challenging to solve the cause of poor accuracy of 2D images and 3D reconstruction. The cause could be due to insufficient spatial resolution of the device or that the unsuited threshold method was applied. The suitability of threshold techniques needed to be evaluated. It was hoped that by finding a suitable threshold method the images would be visually correct and also porosity degree and pore analysis could be reliably determined.

Slice image sets were thresholded using three manually set levels and 22 automatic methods. The thresholded 2D images were compared visually with microscopic, photographic and SEM views of scaffold. Several different threshold levels were applied because it could not be easily said which performed better than the other. Digital and real structures were not similar regardless of what threshold method was used. This probably caused that the calculated porosity degree values of P(L/D)LA 96/4 scaffolds differed significantly from reference values. It also referred to that the spatial resolution of the Planmeca ProMax 3Ds was not good enough to produce sufficiently accurate images. Because of rough image accuracy, the pores and filaments which were smaller than the voxel size of Planmeca system may not be detected by image analysis and it could cause the underestimation to calculated porosity values. The four filament bundles in scaffold structure were probably imagined as one thick fiber. In this case, the digital image would lose the significant amount of empty space from between the filaments. The accuracy differences can be perceived by comparing Planmeca image (Figure 7.1.) and SkyScan image (Figure 6.12.). Mentioned lower estimations on porosity degree values due to too rough resolution of CT system are also observed by other researchers and it is also stated that partial volume effect may result that underestimation as well [46].

To ensure that the inaccuracy of the images was not caused by applying unsuitable threshold method and that the rest of performed image analysis process was suitable, the

comparative study with SkyScan-1072 was decided to perform as well. The study showed that even the complex and thin-filamented structure of polymeric scaffold is easy to bring out from images when the images are acquired with the device having sufficient spatial resolution (8.4-11.1 μm). The threshold levels were easy to adjust manually correct on P(L/D)LA 96/4 scaffold images. On the basis of SkyScan study, it can be concluded that the image accuracy affected to the obtained results for porosity and pore analysis. SkyScan study also proved that the applied image analysis process was correct. These results showed the unsuitability of Planmeca device to acquire enough accurate images of P(L/D)LA 96/4 scaffold which would be needed to calculate reliable values for structural parameters. It could still be possible to enhance the image quality by using some specific image pre-processing tools but it is not very probable.

Planmeca ProMax 3Ds enables to scan and analyze the entire implant structure and that was the main reason why the P(L/D)LA 96/4 scaffold characterization was performed using Planmeca device instead of high resolution SkyScan-1072. Six scaffold sizes were scanned using Planmeca ProMax 3Ds. The 8 mm P(L/D)LA 96/4 scaffolds and 10 mm hand-rolled scaffolds were scanned using SkyScan-1072. Even though the measuring field of both applied devices was large enough to cover whole volume of the specimen, it proved to be challenging to digitally select the analyzed volume so that it would match perfectly with the volume of the sample. That was mostly because of the rounded off corners and uneven surfaces of the scaffold. In case that analyzed volume is selected larger than sample volume, calculated porosity degree would be an overestimation and in turn if analyzed volume is selected smaller than sample volume, determined character represent only a core volume of the sample. Thus, to ensure that extra empty space was not included in present determinations, analyzed volume was selected on purpose smaller than the real volume of the sample. Thus, the calculated porosity degree values described the porosity of the scaffold except for its outermost fringe areas and they do not correspond to the porosity of the entire scaffold totally. In several earlier studies it has not been presented clearly, how large the analyzed volume was in relation to the volume of the sample [14; 44; 46].

In earlier studies, the image analysis for all parallel samples is usually performed using a same constant number of 2D slices [14; 44]. It was not possible to use constant number of images in P(L/D)LA 96/4 scaffold characterization in the present study and same time analyze the entire sample volume because the parallel samples were not physically identical. Micro-CT experiment in present study was performed using constant number of 2D images, but however in Planmeca experiment the used number of images varied according to the size of each specimen. Changes in the size of analyzed volume may affect to the calculated results of porosity.

Micro-CT study showed that the measuring field of the device is sufficient to cover at least the 8 mm and 10 mm scaffold. The image analysis process was performed analyzing 2D image sets with ImageJ and analyzing 3D reconstructed model with Pore Analyzer program. During the image analysis, it was perceived that it is difficult to analyze the entire scaffold volume due to very large amount of image data. That set very

high requirements for computer facilities and made image analysis much slower compared to analysis of Planmeca image data. The SkyScan image analysis was especially inconvenient and slow to perform when the analysis was done using the 3D reconstructed model in Pore Analyzer. Therefore the pore analysis was possible be performed analyzing only a very small core volume of the sample. The analysis of 2D SkyScan image sets with ImageJ succeeded much faster than pore analysis and it was possible to analyze as large volume than in Planmeca ProMax image analysis. The Planmeca image analysis using 2D sets with ImageJ was very comfortable to perform with normal portable computer.

Obtained results from Planmeca ProMax 3Ds and high resolution SkyScan-1072 studies proved that the reliability of image-based characterization of complex biomaterial structures requires the acquisition of high-quality images and skilled image analysis. Skilled image pre-processing can improve the quality of images and thus enhance the correctness of the image-based structural characterization. However, if the quality of the obtained images is too poor, the reliable characterisation of the structure cannot be produced irrespective of how skilled image analysis there is. In order to ensure from the reliability of the calculated results, one must confirm that the thresholded 2D images and 3D reconstruction are visually identical with the target design and also that the values from image-based and non-image-based characterization of the structure should be nearly same. These two criteria must come true because there is no globally functional method to assess the image quality or the suitability of applied threshold method.

8.9. Comparison of applied CT techniques and their suitability for quality control

Two different types of computed tomography devices were applied to characterize polymeric based joint scaffolds in present study and it showed that both methods have advantages and limitations. The measuring field of Planmeca ProMax 3Ds is cylindrical Ø50 mm x 80 mm and maximum recommended sample size for SkyScan 1072 µCT is 15 mm x 15 mm x 30 mm. Thus the focus of both devices is enough large to cover the entire scaffold volume [74]. Planmeca ProMax 3Ds proved to have very fast image acquisition as the scanning and automatic image reconstruction took together only about four minutes for each sample. SkyScan image reconstruction needed to be performed manually which made image acquisition slower. The exact scanning time using SkyScan-1072 is not reported, but however, it is generally observed that using normal high resolution µCT results in longer scan times [18].

Image quality was significantly finer in SkyScan µCT images as both the contrast and the accuracy were better than in Planmeca ProMax images. Better image quality resulted also more reliable values for structural parameters. However, the image analysis was slower and more inconvenient to perform because of larger SkyScan µCT data sets.

Even though the image quality was not sufficient to calculate reliable numerical values for structural parameters using Planmeca ProMax images, present study showed that it is possible to image polymeric materials with Planmeca ProMax 3Ds and also that the contrast of images is sufficient to carry out image analysis for structural characterization. It can be assumed that the calculated values for porosity degree and pore volume of P(L/D)LA 96/4 joint scaffold using Planmeca ProMax image data could be comparable. Achievement of comparable values would still require standardizing at least the scanning parameters, image thresholding and volume selection. For example, porosity degree calculated with standardised parameters could be used for analysing the mutual differences of parallel samples. Applying the introduced image analysis process, the porosity of the entire scaffold or the porosity or of its certain section in two directions could be examined. In addition to the porosity determination, the polymer content could be also measured using same image analysis technique. Because no contrast enhancement would be needed, the non-destructive nature of CT would remain and the examined samples could be returned to production or to other tests after quality control. In addition, the 2D visualization could be used to detect certain factory defects as the broken knitting or large holes from the structure of the scaffold.

9. CONCLUSION

In the present study, five different types of P(L/D)LA 96/4 based joint scaffolds were characterized using two different computed tomography devices with and without contrast enhancement. This study brought out each step of image acquisition showing that both sample material and spatial resolution of imaging device affects to image quality significantly. Spatial resolution affected mostly to the accuracy of obtained images. Material ability to absorb X-ray irradiation showed to have dramatic effect on image contrast. Radio-opacity of P(L/D)LA 96/4 observed to be weaker than ceramic materials but however, it was shown that Planmeca ProMax 3Ds can be used effectively for biopolymeric and bioceramic imaging with complex geometrics which size could be even larger than joint scaffold. Different contrast enhancement approaches were applied including the use of barium sulphate, hydroxyapatite, tricalcium phosphate and iodine. Contrast improvement was observed to be challenging to perform so that the repeatability would be retained and that the sample structure would remain unchanged.

Applied 2D image set analysis with ImageJ and 3D reconstruction model analysis with Pore Analyzer software showed the versatility of computed tomography in scaffold characterization but the versatility depends on the computational capability of the software and hardware. Technique enabled to visualize internal structures of scaffold in sectional 2D images and in 3D view and also allowed calculation of porosity degree, pore volumes and glass content of scaffolds. Porosity degree of different geometrical sections of scaffold architecture was also calculated successfully which is a special feature of CT compared to theoretical and conventional characterization methods. In the previous studies, the P(L/D)LA 96/4 scaffold porosity degree and pore sizes were characterized only qualitatively from a single microscopic image but instead in the present study, each structural characteristic was quantitatively determined from three dimensional sample volume.

This study proved that the spatial resolution of Planmeca ProMax 3Ds is too rough to obtain realistic visual view and reliable values for structural parameters. The two main limitations in image analysis were the challenge of thresholding and accurate sample volume selection from measuring field. Each applied threshold method produced different visual view of sample structure resulting also different numerical values for calculated characteristics. Uneven edges of the scaffold made it difficult to distinguish the entire scaffold volume from measuring field.

10. SUGGESTIONS FOR FURTHER STUDIES

Imaging of biomaterial structures is recommended to carry out without using any contrast enhancement. If the contrast enhancement is still required, then the amount of applied contrast agents should be carefully optimized to the minimum. Instead of adding contrast enhancement to sample, the image quality should be optimized by finding proper imaging parameters. That way, the structure of the sample will be most reliably imaged and the non-destructive nature of CT is retained. The Planmeca ProMax 3Ds is suited better for imaging of ceramics than polymers. This is probably due to that the device has been originally designed for dental imaging and also that ceramics has higher absorbing ability of X-ray irradiation than polymeric materials.

Image quality evaluation in the present study was based on visual assessment which may contain several error factors. In future studies, some new image quality evaluation approaches should be experimented, for example optimal contrast level determination using mathematical calculation methods, in order to improve the reliability of characterization.

Two biggest challenges in image analysis were thresholding and selecting the analyzed volume. This study proved again that the local and global thresholding methods did not perform well in acquired Planmeca ProMax images of P(L/D)LA 96/4scaffold. Therefore it is recommended to threshold obtained images using manually adjusted levels based on visual assessment rather than using automatic methods. Values for structural parameters should be calculated using couple of different threshold levels because it cannot be sure when threshold is set correct. Other observed challenge in image analysis was to select the volume for analysis so that it would have totally matched with sample volume. Therefore it is recommended to select the volume so that it is sure that no extra empty space is included in it. If it is aimed to determine and compare the calculated values between parallel samples, same size of analyzed volume from the core of the sample should be analyzed.

In the present study, the image analysis process was performed by analyzing 2D image sets with ImageJ and analyzing 3D reconstructed model with Pore Analyzer. These analysis techniques have several differences which should notice when choosing a method for image analysis. The structural characterization using 2D image sets with ImageJ was observed faster to perform and larger volume could be analyzed. The drawback of ImageJ characterization was that the manual spreadsheet was needed in order to get the values from 3D volume. Pore Analyzer instead observed to be more versatile allowing determination of various structural parameters automatically from the core volume of sample. The biggest advantage of Pore Analyzer compared to 2D image

set analysis with ImageJ was the ability to perform the volumetric pore analysis using 3D reconstructed model. In many earlier scaffold characterization studies, the subject of interest has been to determine the average pore diameters of the scaffold. The Pore Analyzer still does not allow determining pore diameters which is a significant limitation of the software. In order that all desired parameters could be determined in future studies, applied software must be carefully chosen before characterization.

The assessment of the impact of expose of different X-ray irradiation doses on the material properties was not included in this study. Even though computed tomography is generally considered as a non-destructive testing method, the changes in e.g. glass transition temperature, melting temperature, molecular weight, crystallinity and biocompatibility of scaffold could be determined. It could also be interesting to try if the Planmeca ProMax 3Ds is suitable to measure the structural changes of P(L/D)LA 96/4 scaffold if the structure is altered to physical loading. Also the suitability of the device to scan cell seeded scaffolds in order to study their permeability, migration and proliferation could be studied. Mentioned research frames could give significant advantage for the development of tissue engineering scaffolds.

REFERENCES

[1] Agrawal P, Strijkers GJ, Nicolay K. Chitosan-based systems for molecular imaging. Adv Drug Deliv Rev. 2010;62(1):42-58.

[2] Al-Munajjed AA, Plunkett NA, Gleeson JP, Weber T, Jungreuthmayer C, Levingstone T, et al. Development of a biomimetic collagen-hydroxyapatite scaffold for bone tissue engineering using a SBF immersion technique. Journal of Biomedical Materials Research - Part B Applied Biomaterials 2009;90(2):584-591.

[3] Antheunis H, Van Meer J-D, De Geus M, Kingma W, Koning CE. Improved mathematical model for the hydrolytic degradation of aliphatic polyesters. Macromolecules. 2009;42(7):2462-71.

[4] Aydogan B, Hannula M, Moritz N, Levänen E, Hyttinen J. In: Analysis of multiple resolution μ-CT image sets for pore-size distribution estimation. 2009. p. 1261-1264.

[5] Barrett JF, Keat N. Artifacts in CT: Recognition and avoidance. Radiographics. 2004;24(6).

[6] Bedini R, Meleo D, Pecci R, Pacifci L. The use of microtomography in bone tissue and biomaterial three-dimensional analysis. Annali dell'Istituto Superiore di Sanita. 2009;45(2):178-184.

[7] Bischof JC, Mahr B, Choi JH, Behling M, Mewes D. Use of X-ray tomography to map crystalline and amorphous phases in frozen biomaterials. Ann Biomed Eng. 2007;35(2):292-304.

[8] Brey DM, Chung C, Hankenson KD, Garino JP, Burdick JA. Identification of osteoconductive and biodegradable polymers from a combinatorial polymer library. Journal of Biomedical Materials Research - Part A. 2010;93(2):807-816.

[9] Bronnikov AV. In: Phase-contrast CT: Fundamental theorem and fast image reconstruction algorithms. Progress in biomedical optics and imaging - proceedings of SPIE, 2006.

[10] Bronzino JD. The Biomedical Engineering HandBook, Second Edition. Florida 2000, CRC Press. 3185 p.

[11] Buijs JOD. Measuring fluid transport through scaffolds for engineered tissue. California 2008, SPIE Medical Imaging. 2 p.

[12] Buzug, T.M. Computed Tomography- From Photon Statistics to Modern Cone-Beam CT. Germany 2008, Springer. 521 p.

[13] ConeBeam.Com – CBCT for everyone [www]. [cited 11/2010]. available: http://www.conebeam.com/planning

[14] Darling AL, Sun W. 3D microtomographic characterization of precision extruded poly-ε-caprolactone scaffolds. Journal of Biomedical Materials Research - Part B Applied Biomaterials. 2004;70(2):311-317.

[15] Djukic LP, Herszberg I, Walsh WR, Schoeppner GA, Gangadhara Prusty B, Kelly DW. Contrast enhancement in visualisation of woven composite tow architecture using a MicroCT Scanner. Part 1: Fabric coating and resin additives. Composites Part A: Applied Science and Manufacturing 2009 5;40(5):553-565.

[16] Dorsey SM, Lin-Gibson S, Simon Jr. CG. X-ray microcomputed tomography for the measurement of cell adhesion and proliferation in polymer scaffolds. Biomaterials. 2009;30(16):2967-2974.

[17] Douglas T, Pamula E, Hauk D, Wiltfang J, Sivananthan S, Sherry E, et al. Porous polymer/hydroxyapatite scaffolds: Characterization and biocompatibility investigations. J.Mater.Sci.Mater.Med. 2009;20(9):1909-1915.

[18] Duvall CL, Taylor WR, Weiss D, Guldberg RE. Quantitative microcomputed tomography analysis of collateral vessel development after ischemic injury. American Journal of Physiology - Heart and Circulatory Physiology. 2004;287(1 56-1):302-310.

[19] Egger CC, Du Fresne C, Raman VI, Schädler V, Frechen T, Roth SV, et al. Characterization of highly porous polymeric materials with pore diameters larger than 100 nm by mercury porosimetry and x-ray scattering methods. Langmuir. 2008;24(11):5877-5887.

[20] Filmon R, Retailleau-Gaborit N, Grizon F, Galloyer M, Cincu C, Basle MF, et al. Non-connected versus interconnected macroporosity in poly(2-hydroxyethyl methacrylate) polymers. an X-ray microtomographic and histomorphometric study. Journal of Biomaterials Science, Polymer Edition. 2002;13(10):1105-1117.

[21] Ferreira, T.A. & Rasband, W. The ImageJ User Guide. Canada 2010, Centre for Research in Neuroscience, McGill University. 166 p.

[22] Follet H, Bruyère-Garnier K, Peyrin F, Roux JP, Arlot ME, Burt-Pichat B, et al. Relationship between compressive properties of human os calcis cancellous bone and microarchitecture assessed from 2D and 3D synchrotron microtomography. Bone. 2005;36(2):340-351.

[23] General Electric Company [www]. [cited 10.12.2010]. available: http://www.ge-mcs.com.

[24] Giachetti A, Zanetti G. Vascular modeling from volumetric diagnostic data: A review. Current Medical Imaging Reviews. 2006;2(4):415-423.

[25] Guldberg R, Cartmell S, Case N, Coleman R, Duty A, Duvall C, et al. In: Tissue engineering applications of microcomputed tomography (micro-CT) imaging. ; 2002. 76 p.

[26] Guldberg RE, Duvall CL, Peister A, Oest ME, Lin ASP, Palmer AW, et al. 3D imaging of tissue integration with porous biomaterials. Biomaterials. 2008;29(28):3757-3761.

[27] Hagenmuller H, Kohler T, Hofmann S, Merkle HP, Meinel L, Muller R. Monitoring and quantifying formation of tissue engineered human bone in situ by micro-computed tomography. J Biomech 2006;39(Suppl. 1):218-223.

[28] Ho ST, Hutmacher DW. A comparison of micro CT with other techniques used in the characterization of scaffolds. Biomaterials 2006;27(8):1362-1376.

[29] Hollister SJ, Levy RA, Chu T-, Halloran JW, Feinberg SE. An image-based approach for designing and manufacturing craniofacial scaffolds. Int J Oral Maxillofac Surg. 2000;29(1):67-71.

[30] Honkanen PB, Kellomäki M, Konttinen YT, Mäkelä S, Lehto MUK. A midterm follow-up study of bioreconstructive polylactide scaffold implants in metacarpophalangeal joint arthroplasty in rheumatoid arthritis patients. Journal of Hand Surgery: European Volume. 2009;34(2):179-185.

[31] Honkanen PB, Kellomäki M, Lehtimäki MY, Törmälä P, Mäkelä S, Lehto MUK. Bioreconstructive joint scaffold implant arthroplasty in metacarpophalangeal joints: Short-term results of a new treatment concept in rheumatoid arthritis patients. Tissue Eng. 2003;9(5):957-965.

[32] Jaecques SVN, Van Oosterwyck H, Muraru L, Van Cleynenbreugel T, De Smet E, Wevers M, et al. Individualised, micro CT-based finite element modelling as a tool for biomechanical analysis related to tissue engineering of bone. Biomaterials. 2004;25(9):1683-1696.

[33] Jauhiainen J. TL9181 Lääketieteelliset mittauslaitteet. Kuopion yliopisto, Sovelletun fysiikan laitos. p.20.

[34] Jones JR, Poologasundarampillai G, Atwood RC, Bernard D, Lee PD. Non-destructive quantitative 3D analysis for the optimisation of tissue scaffolds. Biomaterials. 2007;28(7):1404-1413.

[35] Karageorgiou V, Kaplan D. Porosity of 3D biomaterial scaffolds and osteogenesis. Biomaterials. 2005;26(27):5474-5491.

[36] Kempe S, Metz H, Pereira PGC, Mäder K. Non-invasive in vivo evaluation of in situ forming PLGA implants by benchtop magnetic resonance imaging (BT-MRI) and EPR spectroscopy. European Journal of Pharmaceutics and Biopharmaceutics. 2010;74(1):102-108.

[37] Kim S-, Park MS, Gwak S-, Choi CY, Kim B-. Accelerated bonelike apatite growth on porous polymer/ceramic composite scaffolds in vitro. Tissue Eng. 2006;12(10):2997-3006.

[38] Kokubo T, Kushitani H, Sakka S, Kitsugi T, Yamamuro T. Solutions able to reproduce in vivo surface-structure changes in bioactive glass-ceramic A-W3. J Biomed Mater Res. 1990;24(6):721-734.

[39] Kulmala, T. Development of the manufacturing process of the bioreconstructivefinger joint implant. Master of science thesis. Tampere 2002. Tampere University of Technology, Institute of Biomaterials. 98p.

[40] Lin ASP, Barrows TH, Cartmell SH, Guldberg RE. Microarchitectural and mechanical characterization of oriented porous polymer scaffolds. Biomaterials. 2003;24(3):481-489.

[41] Lin-Gibson S, Cooper JA, Landis FA, Cicerone MT. Systematic investigation of porogen size and content on scaffold morphometric parameters and properties. Biomacromolecules. 2007;8(5):1511-1518.

[42] Liu E, Treiser MD, Johnson PA, Patel P, Rege A, Kohn J, et al. Quantitative biorelevant profiling of material microstructure within 3D porous scaffolds via multiphoton fluorescence microscopy. Journal of Biomedical Materials Research - Part B Applied Biomaterials. 2007;82(2):284-297.

[43] Markowska O, Gardzińska A, Chrzan R, Urbanik A, Miechowicz S. Use of computer tomography and 3DP rapid prototyping technique in cranioplasty planning - analysis of accuracy of bone defect modelling. Polish Journal of Radiology. 2009;74(4):43-46.

[44] Maspero FA, Ruffieux K, Müller B, Wintermantel E. Resorbable defect analog PLGA scaffolds using CO2 as solvent: Structural characterization. J Biomed Mater Res. 2002;62(1):89-98.

[45] Mather ML, Morgan SP, White LJ, Tai H, Kockenberger W, Howdle SM, et al. Image-based characterization of foamed polymeric tissue scaffolds. Biomedical Materials. 2008;3(1).

[46] Moore MJ, Jabbari E, Ritman EL, Lu L, Currier BL, Windebank AJ, et al. Quantitative analysis of interconnectivity of porous biodegradable scaffolds with micro-computed tomography. Journal of Biomedical Materials Research - Part A. 2004;71(2):258-267.

[47] Mutanen, M. Studies of bioreconstructive small-joint prosthesis. Master of science thesis. Tampere 2004. Tampere University of Technology, Institute of Biomaterials. 92p.

[48] Müller FA, Müller L, Hofmann I, Greil P, Wenzel MM, Staudenmaier R. Cellulose-based scaffold materials for cartilage tissue engineering. Biomaterials 2006;27(21):3955-3963.

[49] Nair LS, Laurencin CT. Biodegradable polymers as biomaterials. Progress in Polymer Science (Oxford). 2007;32(8-9):762-798.

[50] Narayan R. Biomedical materials. Chapel Hill 2009, Springer. 566 p.

[51] Niemelä T, Aydogan D B, Hannula M, Hyttinen J, Kellomäki M. Determination of bioceramic filler distribution and porosity of self-reinforced bioabsorbable composites using microcomputed tomography. Department of Biomedical Engineering, Tampere University of Technology. p.37.

[52] Nitzsche H, Metz H, Lochmann A, Bernstein A, Hause G, Groth T, et al. Characterization of scaffolds for tissue engineering by benchtop-magnetic resonance imaging. Tissue engineering.Part C, Methods. 2009;15(3):513-521.

[53] Oest ME, Dupont KM, Kong H-, Mooney DJ, Guldberg RE. Quantitative assessment of scaffold and growth factor-mediated repair of critically sized bone defects. Journal of Orthopaedic Research. 2007;25(7):941-950.

[54] Oliveira AL, Malafaya PB, Costa SA, Sousa RA, Reis RL. Micro-computed tomography (μ -CT) as a potential tool to assess the effect of dynamic coating routes on the formation of biomimetic apatite layers on 3D-plotted biodegradable polymeric scaffolds. J Mater Sci Mater Med. 2007;18(2):211-223.

[55] Palmer AW, Guldberg RE, Levenston ME. Analysis of cartilage matrix fixed charge density and three-dimensional morphology via contrast-enhanced

microcomputed tomography. Proc Natl Acad Sci U S A. 2006;103(51):19255-19260.

[56] Park S, Cho W, Park S, Lee M,. Segmentation for medical image using a statistical initial process and a level set method [www]. [cited 19.4.2011]. Available: www.scopus.com.

[57] Passariello R, Catalano C, Francone M, Ascarelli A, Mangia M, Iacucci I. Optimizing radiation dose and image quality. European Radiology, Supplement. 2007;17(SUPPL. 6):F26-32.

[58] Porter B, Zauel R, Stockman H, Guldberg R, Fyhrie D. 3-D computational modeling of media flow through scaffolds in a perfusion bioreactor. J Biomech. 2005;38(3):543-549.

[59] Poukalova M, Yakacki CM, Guldberg RE, Lin A, Saing M, Gillogly SD, et al. Pullout strength of suture anchors: Effect of mechanical properties of trabecular bone. J Biomech. 2010;43(6):1138-1145.

[60] Rai B, Oest ME, Dupont KM, Ho KH, Teoh SH, Guldberg RE. Combination of platelet-rich plasma with polycaprolactone-tricalcium phosphate scaffolds for segmental bone defect repair. Journal of Biomedical Materials Research - Part A. 2007;81(4):888-899.

[61] Rajagopalan S, Lu L, Yaszemski MJ & Robb RA. Optimal segmentation of micro computed tomographic images of porous tissue-engineering scaffolds. Journal of Biomedical Materials Research – Part A. 2005;75(4):877–887.

[62] Ratner BD, Hoffman AS, Schoen FJ & Lemons JE. Biomaterials Science - An Introduction to Materials in Medicine 2nd Edition. California 2004, Elsevier. 851 p.

[63] Ravi Kumar MNV. A review of chitin and chitosan applications. React Funct Polym. 2000;46(1):1-27.

[64] Renghini C, Komlev V, Fiori F, Verné E, Baino F, Vitale-Brovarone C. Micro-CT studies on 3-D bioactive glass-ceramic scaffolds for bone regeneration. Acta Biomaterialia. 2009;5(4):1328-1337.

[65] Santo VE, Duarte ARC, Gomes ME, Mano JF, Reis RL. Hybrid 3D structure of poly(d,l-lactic acid) loaded with chitosan/chondroitin sulfate nanoparticles to be used as carriers for biomacromolecules in tissue engineering. Journal of Supercritical Fluids. 2010;54(3):320-327.

[66] Schmidt C, Bezuidenhout D, Beck M, Van der Merwe E, Zilla P, Davies N. Rapid three-dimensional quantification of VEGF-induced scaffold

neovascularisation by microcomputed tomography. Biomaterials. 2009;30(30):5959-5968.

[67] Sharpe J, Ahlgren U, Perry P, Hill B, Ross A, Hecksher-Sørensen J, et al. Optical projection tomography as a tool for 3D microscopy and gene expression studies. Science. 2002;296(5567):541-545.

[68] Sikavitsas VI, Bancroft GN, Lemoine JJ, Liebschner MAK, Dauner M, Mikos AG. Flow perfusion enhances the calcified matrix deposition of marrow stromal cells in biodegradable nonwoven fiber mesh scaffolds. Ann Biomed Eng. 2005;33(1):63-70.

[69] Simon Jr. CG, Eidelman N, Kennedy SB, Sehgal A, Khatri CA, Washburn NR. Combinatorial screening of cell proliferation on poly(l-lactic acid)/poly(d,l-lactic acid) blends. Biomaterials. 2005;26(34):6906-6915.

[70] Sippola, L. Tissue engineering scaffolds for osteochondral damage. Master of science thesis. Tampere 2004. Tampere University of Technology, Institute of Biomaterials. 93p.

[71] Starly B, Shor L, Fang Z, Sun W. In: Design and freeform fabrication of load bearing tissue scaffolds. ; 2005. p. 163-165.

[72] Suomalainen, A. Cone beam computed tomography in oral radiology. Doctoral thesis. Helsinki 2010. Department of Oral Radiology, Institute of Dentistry, University of Helsinki, Finland. 80p.

[73] The Open Access NDT Database [www]. [cited 9.10.2010]. available: http://www.ndt.net.

[74] University of Aberdeen, Institute of Medical Sciences [www]. [cited 10.12.2010]. available: http://www.abdn.ac.uk/ims/index.php

[75] van Lenthe GH, Hagenmüller H, Bohner M, Hollister SJ, Meinel L, Müller R. Nondestructive micro-computed tomography for biological imaging and quantification of scaffold-bone interaction in vivo. Biomaterials. 2007;28(15):2479-2490.

[76] Van Tienen TG, Heijkants RGJC, Buma P, De Groot JH, Pennings AJ, Veth RPH. Tissue ingrowth and degradation of two biodegradable porous polymers with different porosities and pore sizes. Biomaterials. 2002;23(8):1731-1738.

[77] Voronov R, VanGordon S, Sikavitsas VI, Papavassiliou DV. Computational modeling of flow-induced shear stresses within 3D salt-leached porous scaffolds imaged via micro-CT. J Biomech. 2010;43(7):1279-1286.

[78] Waris E, Ashammakhi N, Lehtimäki M, Tulamo R, Kellomäki M, Törmälä P, et al. The use of biodegradable scaffold as an alternative to silicone implant arthroplasty for small joint reconstruction: An experimental study in minipigs. Biomaterials. 2008;29(6):683-691.

[79] Xu H, Othman SF, Magin RL. Monitoring tissue engineering using magnetic resonance imaging. Journal of Bioscience and Bioengineering. 2008;106(6):515-527.

[80] Yang Y, Dorsey SM, Becker ML, Lin-Gibson S, Schumacher GE, Flaim GM, et al. X-ray imaging optimization of 3D tissue engineering scaffolds via combinatorial fabrication methods. Biomaterials 2008;29(12):1901-1911.

[81] Yue S, Lee PD, Poologasundarampillai G, Yao Z, Rockett P, Devlin AH, et al. Synchrotron X-ray microtomography for assessment of bone tissue scaffolds. J Mater Sci Mater Med. 2010;21(3):847-853.

APPENDIX 1: A TECHNICAL SPECIFICATIONS OF PLANMECA PROMAX 3DS

X-ray tube	Toshiba D-054SB-P
X-ray beam	Cone
Anode voltage	54 -84mV ± 5%
Anode current	1-16 mA ± 10%
Exposure time	Pulsed, effective 2.4-12s
Filtering	range 3-48 mm, 5 and 10 mm thick aluminium sheets
Focal spot	0,5 mm, fixed anode
Image detector	Amorphous silicon flat panel
Gray scale	15 bit
Detector resolution	630 x 1024 pixels pixel size 127 µm x 127 µm
Voxel size	100 x 100 x 100 µm, isotropic 200 x 200 x 200 µm, isotropic
Image acquisition	Single 200 degree rotation
Total scan time	18s, pulsed X-ray
Reconstruction time	15-60 s
Standard volumes (diameter x height)	Ø50 x 80 mm (child mode Ø42 x 68 mm) Ø50 x 50 mm (child mode Ø42 x 42 mm)
Stitched volume (w x d x h)	90 x 60 x 130 mm
3D Reconstruction server	Proprietary Feldkamp type back projection reconstruction algorithm Improved Artefact Removal (IAR) for high contrast object compensation
Magnification	Constant 1,57
SID	527 mm (20,74in.)
Software	Planmeca Romexis

APPENDIX 2: CALCULATED POROSITY VALUES USING MASS TECHNIQUE [Modified 47]

Diameter of the scaffold [mm]	Average porosity (%)	Standard deviation
8	69,53	1,67
10	74,81	1,34
12	75,95	1,27
14	78,53	1,20
18	78,07	1,21
20	77,21	0,90

APPENDIX 3: A RESULT CHART FROM PORE ANALYSIS

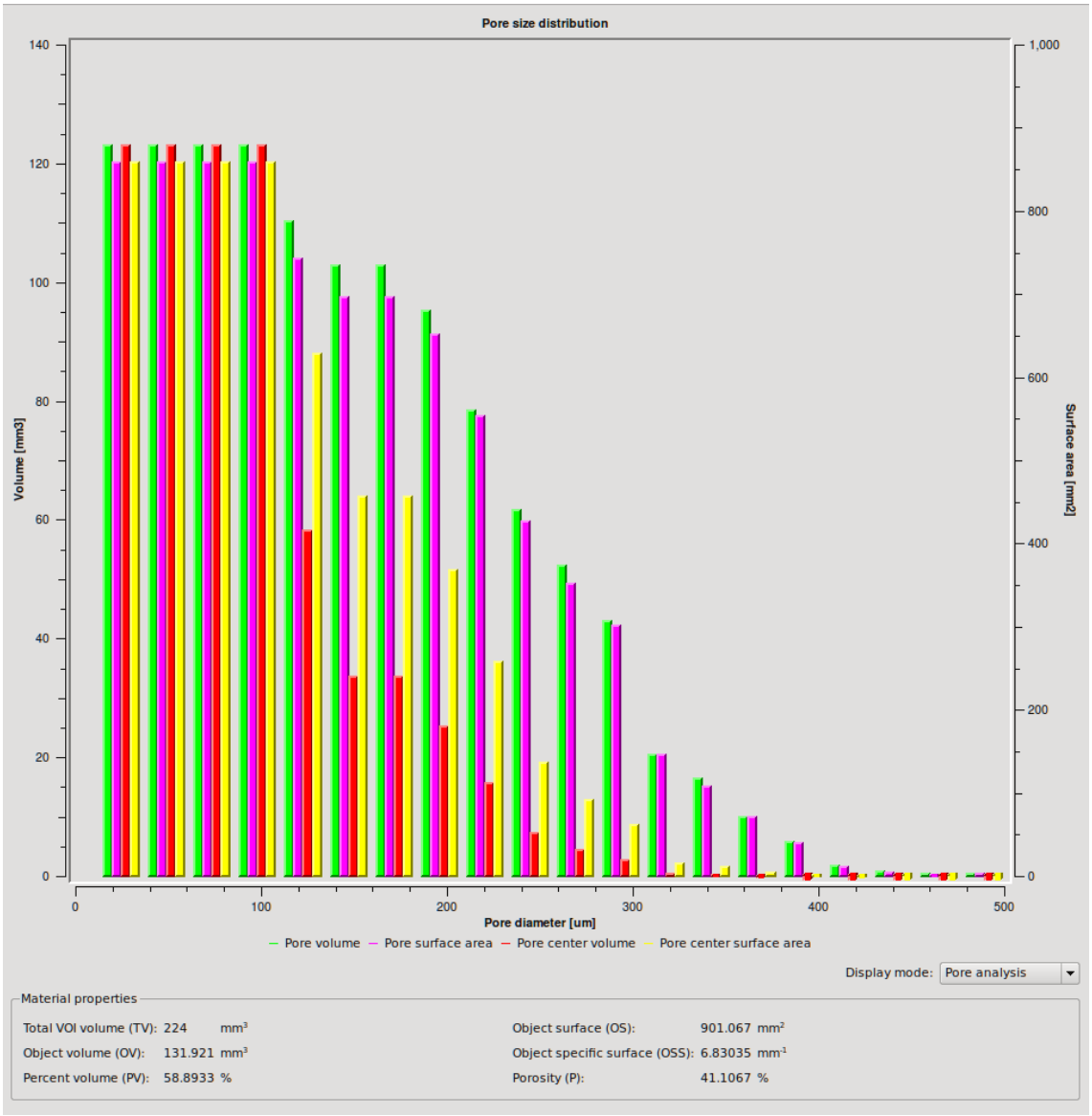

APPENDIX 4: A 3D RECONSTRUCTED MODEL OF PCG TYPE SCAFFOLD CORE VOLUME